

Luminosity measurement at CMS

Von der Fakultät für MINT – Mathematik, Informatik, Physik,
Elektro- und Informationstechnik
der Brandenburgischen Technischen Universität Cottbus-Senftenberg

zur Erlangung des akademischen Grades eines
Doktors der Naturwissenschaften
(Dr. rer. nat.)

genehmigte Dissertation
vorgelegt von

M. Sc.
Olena Karacheban
geboren am 19.02.1990 in Izmail

Gutachter: Prof. Dr. Wolfgang Lohmann

Gutachter: Prof. Dr. Karl Jansen

Gutachter: Prof. Dr. Ben Kilminster

Gutachter: Prof. Dr. Götz Seibold

Tag der mündlichen Prüfung: 5. Januar 2017

Erklärung über frühere Promotionsanträge

Hiermit versichere ich, dass ich bisher noch kein Antrag für ein Promotionsverfahren eingereicht habe.

Cottbus, den 28.10.2016

Olena Karacheban

Selbständigkeitserklärung

Hiermit versichere ich, dass ich die vorliegende Arbeit selbständig und nur unter Verwendung der angegebenen Quellen und Hilfsmittel angefertigt habe.

Cottbus, den 28.10.2016

Olena Karacheban

Erklärung von Schutzrechten

Hiermit versichere ich, dass die Veröffentlichung der Dissertation keine bestehenden Schutzrechte verletzt.

Cottbus, den 28.10.2016

Olena Karacheban

Abstract

Luminosity is a key quantity of any collider, since it allows for the determination of the absolute cross sections from the observed rates in a detector. Since the Higgs boson discovery in 2012, the highest priority at the Large Hadron Collider (LHC) has been given to an accurate understanding of the electroweak scale and a search for new physics. Precise luminosity measurements in such conditions are of crucial importance, as they determine the precision of any physics cross section measurement.

To increase the production of particles of interest, usually of low cross section, the LHC is running at the highest possible luminosity. After the first Long Shutdown (LS1) the original performance goal for the luminosity of $1 \times 10^{34} \text{ cm}^{-2} \text{ s}^{-1}$ was reached with 10^{11} protons per bunch and a bunch spacing of 25 ns. In such conditions radiation hard detectors with extremely fast response time are required, especially for instrumentation near the beam.

The Compact Muon Solenoid experiment is equipped with three online luminometers, which fulfill the listed requirements: the Fast Beam Conditions Monitor (BCM1F), the Pixel Luminosity Telescope (PLT) and the Forward Hadron calorimeter (HF).

The BCM1F was upgraded during LS1 from 8 to 24 diamond sensors and is read out by a dedicated fast ASIC. The back-end comprises a deadtime-less histogramming unit, with 6.25 ns bin width and analog-to-digital converters with 2 ns sampling time in the VME standard. A microTCA system with better time resolution is in development.

Particles originating from collisions and machine induced background arrive with 12 ns time difference. Because of its excellent time resolution BCM1F measures separately both luminosity and machine induced background particles. The performance of the detector in the first running period and radiation damage monitoring of the sensors and electronics chain form the first part of this thesis.

Calibration of the luminometers at the LHC is done using van der Meer (VdM) scans. The proton beams are scanned against each other separately in the x and y directions. The effective width of the beams is measured and the visible cross section, the key quantity for the luminosity measurement, is determined. The im-

pact of detector instability, beam-beam effects, correlations of the particle density distributions in the x and y planes, and satellite and ghost bunches are studied in detail and systematic uncertainties are derived. The systematic error on the visible cross section was estimated to be 3.1% in the 50 ns operation period. A comparison of the VdM scans of 2015 and 2016 completes the second part of the thesis, as well as a comparison of the results delivered by other luminometers.

As a contribution to the upgrade of the beam instrumentation for the high luminosity LHC, a novel single crystal sapphire detector was designed, built and studied in a test-beam. The detector comprises a stack of sapphire plates. The response depends on the direction of the incident particles. The performance of the detector is described in the third part of the thesis. It is demonstrated that this sapphire detector can be used for the detection of single relativistic particles. The results point to the dominant contribution of the electrons to the signal generation in sapphire.

Kurzfassung

Die Luminosität ist eine Schlüsselgrösse eines jeden Beschleunigers und Speicherrings (Collider). Die Ereignisrate eines speziellen Wechselwirkungsprozesses ist das Produkt aus Luminosität und Wirkungsquerschnitt. Daher ist eine hohe Luminosität wünschenswert, um interessante physikalische Prozesse mit kleinem Wirkungsquerschnitt zu untersuchen. Die Messung der Luminosität ist zur Berechnung von Wirkungsquerschnitten aus beobachteten Ereignisraten notwendig. Seit der Entdeckung eines Higgs-Bosons im Jahr 2012 wird am Large Hadron Collider (LHC) mit höchster Priorität am Verständnis der elektroschwachen Skala und der Suche nach neuer Physik gearbeitet. Präzise Luminositätsmessungen sind dabei von entscheidender Bedeutung, um Messungen von Wirkungsquerschnitten mit den Vorhersagen der Theorie zu vergleichen.

Nach der ersten langen Betriebspause des LHC (Long Shutdown 1, LS1) wurde die geplante Luminosität von $1 \times 10^{34} \text{ cm}^{-2} \text{ s}^{-1}$ mit maximal 3564 Teilchenpaketen im Zeitabstand von 25 ns mit 10^{11} Protonen pro Paket erreicht. Während der Datennahme wird die Luminosität mit speziellen Detektoren, den Luminometern, gemessen. Diese Online-Luminometer liefern sofort die aktuellen Werte der Luminosität für jede Wechselwirkung von Teilchenpaketen im Experiment an die Kontrollräume vom Compact Muon Solenoid Experiment und dem LHC und tragen so zur Optimierung des Arbeitregimes bei. Eine hohe Zeitauflösung und, da sie in der Nähe des Strahlrohrs installiert sind, eine hohe Strahlenhärte sind für Luminometer erforderlich.

Das CMS Experiment ist mit drei Online-Luminometern ausgestattet: der Fast Beam Conditions Monitor (BCM1F), das Pixel Luminosity Telescope (PLT) und das Forward Hadron calorimeter (HF).

Das BCM1F-System wurde während des LS1 erweitert. Die Zahl der Diamantsensoren wurde von 8 auf 24 erhöht, um ein hohes Maß an Redundanz zu erhalten. Wegen der höheren Folgefrequenz der Teilchenpakete wurde die Front-End-Elektronik durch einen speziell entwickelten ASIC ersetzt. Die Auswerteelektronik umfasst eine eigens für diesen Zweck entwickelte totzeitlose Histogrammier-Einheit mit 6.25 ns Zeitauflösung und einen Analog-Digital-Wandler mit 2 ns Sampling-Zeit im VME-Standard. Ein MicroTCA-ADC System mit noch besserer Zeitauflösung

ist in Entwicklung.

Die Teilchen von Reaktionsprodukten der Kollisionen und vom maschineninduzierten Hintergrund treffen mit 12 *ns* Zeitdifferenz auf die Sensoren. Aufgrund seiner ausgezeichneten Zeitauflösung wird BCM1F sowohl für Luminositäts- als auch für Hintergrundmessungen verwendet. Die Bestimmung der wesentlichen Kenngrößen des Detektors in der ersten Laufzeit und die Abschätzung von Strahlungsschäden der Sensoren und der Elektronik bilden den ersten Teil dieser Dissertation.

Die Kalibrierung der Luminometer erfolgt am LHC mit van der Meer (VdM) Scans. Die Protonenstrahlen werden dabei in definierten Schritten in x - und y -Richtungen bewegt, um die effektive Breite der Strahlen und den sogenannten sichtbaren Wirkungsquerschnitt zu messen. Der sichtbare Wirkungsquerschnitt ist unabhängig von den Strahlparametern im LHC. Zur Abschätzung des systematischen Fehlers wurde der Einfluss von Instabilitäten des Detektors, Strahl-Strahl-Wechselwirkungen, Korrelationen zwischen den Teilchendichten in x und y , Satellite- und sogenannter Geisterpakete auf die Messung des sichtbaren Wirkungsquerschnitts bestimmt. Im Ergebnis wurde der systematische Fehler zu 3.1% bestimmt. Ein Vergleich der VdM-Scans von 2015 und 2016 sowie ein Vergleich mit den Ergebnissen anderer Luminometer schließt den zweiten Teil der Arbeit ab.

Als Beitrag zur Weiterentwicklung der Strahlinstrumentierung für die spätere Phase hoher Luminosität am LHC wurde ein Einkristall-Saphir-Detektor entworfen, gebaut und im Teststrahl vermessen. Der Detektor besteht aus aufeinanderliegenden Saphirplatten, die einzeln ausgelesen werden. Die Signalgröße hängt von der Weglänge der Teilchen im Sensormaterial ab, so dass mit einem Schnitt auf die Signalgröße Teilchen in einem kleinen Winkel zur Sensorebene selektiert werden können. Die Kenngrößen des Detektors sind im dritten Teil der Dissertation beschrieben. Die vorliegende Studie zeigt, dass Saphirdetektoren zum Einzelteilchennachweis eingesetzt werden können. Die Hinweise auf den dominierenden Beitrag der Elektronen zum Signal werden bestätigt.

Acknowledgements

Modern accelerator physics community reminds me more of a big family, where intelligent and motivated people are working together for the same goal. Of course there are smaller working groups and competing spirit between experiments, but at the same time everyone is working on the complementary study, a part of a strong wish to understand how our Universe was built and which forces are keeping it in the state we observe it.

With currently available amounts of processed data, many analysis tools and expert knowledge is needed, and one person can not do everything. Also to complete the studies presented in this thesis a lot of people from different working groups contributed and I would like to say great thanks to all of them.

First of all, thanks to Prof. Wolfgang Lohmann for his patience, support and advices, and for supervising all this work. Thanks to Dr. Sergej Schuwalow, who made valuable contribution to complete the sapphire sensors test beam analysis, for his creativity and brilliant ideas, for perseverance, and for countless number of interesting and useful discussions. Thanks to Prof. Vladimir Aushev and Prof. Viatcheslav Sharyy, my first professors, for showing me the way.

I have to give an absolutely special thanks to my parents, Lidiya Karacheban and Vitalii Karacheban, grandmother Valentina Karpenko and friends Tatiana Olar, Alla Voitshenko and Hannes Jähnert for believing in me sometimes more than I did myself.

Thanks to the DESY-Zeuthen group: Wolfgang Lange, Hans Henschel, Maria Hempel, Martin Stegler, Olga Novgorodova and Lucia Bortko for all the nice days we have spent together and for all problems we managed to solve.

Thanks to the CMS BRIL project at CERN coordinators Anne Dabrowski and David Stickland and the whole group for all I learned from them and for all support they gave. Thanks to Monika Grothe for the analyses framework, Keith Rose, Jakob Salfeld and Chris Palmer for collaborative work on the VdM scans, Arkady Likhovitskiy for his great help to solve stability problem of the ADCs daisy chain and to set readout, Jessica Leonard for work she carried out with ADC and RHU modules, Jonas Daugalas, Zhen Xie for creating monitoring tools and saving the data, Moritz Guthoff for his advices and for organization of the CERN test beam

important for the BCM1F upgrade.

Thanks to the test beam facility at DESY Hamburg, a member of the Helmholtz Association (HGF) and DESY Hamburg colleagues, who helped to complete successfully our beam test and to set the EUDET Telescope analysis: Igor Rubinskiy, Vladyslav Libov, Simon Spannagel, Hanno Perrey.

The crew and the management of the S-DALINAC accelerator at the Technical University of Darmstadt for provided great support during the measurements at the electron beams. The Target Lab of the GSI Helmholtzzentrum für Schwerionenforschung for provided the metallization of the sensors.

Thanks to Taras Shevchenko National University of Kyiv and Brandenburg Technical University Cottbus-Senftenberg for making my study possible.

It is important to mention, that this work was supported by the Commission of the European Communities under the 7th Framework Program AIDA, contract no. 261015; the Tel Aviv University and the Brandenburg Technical University Cottbus-Senftenberg are supported by the German-Israel Foundation (GIF).

Thank you!

Contents

1	Introduction to collider physics	3
1.1	Large Hadron Collider	3
1.2	Experiments at the LHC	4
1.3	Physics goals at LHC	6
1.4	The CMS Experiment	6
2	Measurement of the luminosity at colliders	10
2.1	Absolute luminosity from machine parameters	12
2.2	Calibration of luminometers	12
2.3	Luminosity calculation using physics cross section	15
2.4	Beam Radiation, Instrumentation and Luminosity project	16
2.4.1	New pixel luminosity telescope	18
2.4.2	The Fast Beam Condition Monitor	19
2.4.3	The Beam Halo Monitor	22
2.5	Other luminometers of the CMS	23
2.5.1	The Hadron Forward calorimeter	23
2.5.2	Silicon pixel detector	24
2.6	Radiation simulations	25
3	BCM1F detector as luminometer	26
3.1	The BCM1F	26
3.2	Diamond as a solid state detector	27
3.3	Sensor characterization	29
3.4	Front-end electronics	29
3.5	Signal transmission and back-end electronics	30
3.5.1	Analogue signal processing using VME ADC	31
3.5.2	Processing of the data using the Real-time Histogramming Unit	32
3.5.3	The MicroTCA based back-end electronics	34
3.6	Beam splashes and BCM1F timing adjustment	34
3.6.1	ADC data analysis from splashes	35

Contents

3.7	The BCM1F response studies using the VME ADC	37
3.7.1	Baseline position	38
3.7.2	Detector response for particle hits and test pulses	38
3.7.3	Signal amplitude and signal length spectra	40
3.8	Detector stability and radiation damage monitoring	42
3.8.1	BCM1F stability within long LHC fills and in the 50 ns operation period	43
3.8.2	BCM1F performance as a function of the luminosity	47
3.8.3	Observations during measurements	55
3.8.4	Web monitoring tool	58
4	Measurements of the luminosity using BCM1F	60
4.1	BCM1F rate measurements using the Real-time Histogramming Unit	60
4.1.1	Online Luminosity calculation	61
4.1.2	Aggregated channel rate histograms	62
4.2	VdM scan in August 2015	63
4.2.1	Van der Meer scan analysis framework	65
4.2.2	Fits of the rate as a function of the relative displacement of the beams	66
4.2.3	Influence of the beam current measurement on σ_{vis}	68
4.2.4	Contribution of satellite bunches and ghosts to the beam current measurement	71
4.2.5	Contributions from MIB and albedo to the rates measured in the VdM scan	72
4.2.6	Length scale scan	74
4.2.7	Orbit drift	80
4.2.8	Correlations between the particle densities in the x and y planes	81
4.2.9	Beam-beam effects	82
4.3	Stability of BCM1F over the 50 ns running period and systematic uncertainties	84
4.3.1	Relative channel-to-channel stability	84
4.3.2	Systematic uncertainties of the luminosity measurements	85
4.4	Luminosity measurements using a single channel	85
4.4.1	Validation of the aggregated histogram	86
4.4.2	Visible cross section for single channel	88
4.5	Comparison of VdM scans in 2015 and 2016	90
4.6	Comparison of the luminometers	93

5	Upgrade of the luminometers for high luminosity LHC	96
5.1	Artificial Sapphire	96
5.1.1	Historical excurs	97
5.1.2	Basic features of artificial sapphire and industrial applications	100
5.1.3	Sapphire as a solid state detector	100
5.2	Sensor characterization and tests	102
5.2.1	Electrodes	103
5.2.2	Sensor characterization in the laboratory	103
5.2.3	The response of sapphire sensor as a function of the dose . . .	103
5.3	Detector stack design	105
5.4	Test beam setup	107
5.5	Data synchronization and analysis	108
5.5.1	Track reconstruction	109
5.5.2	Selection of data samples	110
5.5.3	Sapphire sensor response	112
5.5.4	Common mode noise	112
5.5.5	Signal spectrum	115
5.5.6	Systematic errors	116
5.6	Charge collection efficiency	118
5.7	Study of the sensor response as a function of the x coordinate	120
5.8	CCE as a function of time	122
5.9	A model to describe the CCE of sapphire sensors	123
5.9.1	Dependence of electric field on sensor depth	123
5.9.2	Signal size estimate	124
5.9.3	CCE as a function of local y	126
A	Adjustment of the BCM1F signal delay with respect to BPTX	132
A.1	BPTX signal delay	132
A.2	BCM1F signal delay and coincidence with BPTX	132
A.3	Coincidence of BPTX and BCM1F signals from both ends	133
A.4	Relative delay measurements using beam splash events	134
B	Linear coordinate transformation for the sapphire stack	136
B.1	Detector alignment	136
B.2	Linear coordinate transformation	138

Key abbreviations

ADC – Analog to Digital Converter
ASIC – Application-Specific Integration Circuit
ATLAS – A Toroidal LHC ApparatuS
BCID – Bunch Crossing IDentification number
BCM1F – Fast Beam Conditions Monitor
BCML – Beam Conditions Monitor Leakage
BHM – Beam Halo Monitor
BPM – Beam Position Monitor
BPTX – Beam Pick-up Timing for experiment
BQM – Beam Quality Monitor
BX – Bunch crossing
CCE – Charge Collection Efficiency
CMN – Common Mode Noise
CMS – Compact Muon Solenoid
CVD – Chemical Vapor Deposition
DCCT – Direct Current Current Transformers
FBCT – Fast Beam Current Transformers
FPGA – Field-Programmable Gate Array
HF – Forward Hadronic calorimeter
IP – Interaction Point
LDM – Longitudinal Density Monitors
LHC – Large Hadron Collider
LHCb – Large Hadron Collider beauty
LUT – Look-Up Table
MIB – Machine Induced Background
MicroTCA – Micro Telecommunications Computing Architecture
MIP – Minimum Ionizing Particle
PCB – Printed Circuit Board
RHU – Real-time Histogramming Unit
TLU – Trigger Logic Unit
VME – VERSA Module Eurocard bus standard

Introduction

The era of colliders in particle physics started in the 1950s and has developed from MeV to TeV energies up to now. There are two families of colliders: linear colliders, where particles are accelerated in opposite directions and brought to collision, and circular colliders, where two particle beams are accelerated in opposite directions in a ring accelerator, stored and collided in particular interaction points. In the past the largest circular colliders were the Large Electron Positron collider (LEP, 1989 - 2000) at CERN, Geneva area, the Hadron Electron Ring facility (HERA, 1992-2007) for proton-electron collisions at DESY, Hamburg and the proton-antiproton collider Tevatron (1983 - 2011) at Fermilab, Batavia, Illinois. Future linear colliders for electrons and positrons are in the planning phase.

Discoveries made at collider experiments confirmed the existence of the W and Z bosons predicted by theory and discovered new generations of matter particles. The Standard Model (SM) of particle physics was validated brilliantly on the level of quantum corrections. However, the Higgs boson had not yet been discovered and the Higgs mechanism, presumed to be responsible for electroweak symmetry breaking, had not been proven. The mass of the Higgs boson is not predicted by the SM. All searches in the experiments at the aforementioned colliders were not successful, but a lower mass limit of about 114 GeV was obtained. This was the motivation for investigations at higher energies. Also the open questions about matter-antimatter asymmetry in the Universe, the unknown nature of the so-called dark matter and dark energy provoke alternative to SM theories with new symmetries or new forces involved. These open questions motivated the development and construction of the Large Hadron Collider (LHC).

The LHC project was approved by CERN in 1994 to be built using the already-existing tunnel of LEP. The LHC started physics operation in 2010, equipped with two general purpose experiments, ATLAS and CMS, and two smaller experiments, ALICE, for heavy ions, and LHCb, specialized in B-physics. In July 2012 the discovery of the Higgs boson was announced by both experiments ATLAS and CMS, using data samples corresponding to integrated luminosities of up to 5.1 fb^{-1} at 7 TeV and 5.3 fb^{-1} at 8 TeV .

The LHC layout and a short description of the experiments are given in Chap-

Contents

ter 1.

The luminosity as an LHC machine parameter is of crucial importance for any physics cross section measurement, as the precision of the luminosity measurement directly translates to the precision of the cross section measurement and often is the dominant uncertainty. The definition of the luminosity and its measurement at the CMS experiment are described in Chapter 2.

After the first scheduled long LHC maintenance period, the Long Shutdown 1 (LS1), the LHC came back to operation at 6.5 TeV energy per beam with bunch spacing reduced from 50 ns to 25 ns . To deal with these conditions, several of the CMS subsystems were upgraded. One of them is the diamond-based Fast Beam Conditions Monitor (BCM1F). It is designed for both luminosity and Machine Induced Background (MIB) measurements. The front-end and back-end of BCM1F are described in Chapter 3. BCM1F is installed in the tracker detector volume, next to the interaction point, therefore radiation damage is expected. Radiation creates new traps for charge carriers, reducing the charge collection efficiency and leading to a drop in the signal size. Detector characterization and monitoring of the detector performance during data-taking are presented.

A nominal luminosity of $10^{34} \text{ cm}^{-2} \text{ s}^{-1}$ is expected in the LHC Run II. The availability of more than one luminometer is beneficial for the experiment not only to guarantee smooth and uninterrupted luminosity measurement, but also for cross checks of the measurement methods. CMS is equipped in Run II with three on-line luminometers. The calibration of the luminometers is done using van der Meer (VdM) scans. There is a list of corrections that have to be taken into account. For example, beam-beam deflections, orbit drift and length scale corrections, which affect beam separation measurements, and unbunched beam correction, which affect the normalization of the measured count rates. The calibration of the BCM1F luminometer, the above mentioned corrections and the comparison to other luminometers are shown in Chapter 4.

For future upgrades, new detector materials and technologies are required. For instrumentation next to the beam pipe, radiation hardness, low leakage current and fast response are the critical requirements. A study of a novel, direction-sensitive sapphire-based detector, tested in a 5 GeV electron beam at DESY-II, is presented in Chapter 5.

Chapter 1

Introduction to collider physics

1.1 Large Hadron Collider

The LHC [1], is a 27 *km* long circular particle accelerator and collider, installed in the tunnel previously occupied by LEP [2] at CERN [3], Geneva, Switzerland. It is the largest accelerator system in the world, designed for proton-proton collisions with a maximum of 7 *TeV* energy per beam.

Protons at the LHC are accelerated in a 400 *MHz* Radio Frequency (RF) system in opposite directions in two separate rings and brought into collisions at four Interaction Points (IPs), equipped with detectors.

The beams have a bunch structure. Bunches containing about 1.15×10^{11} protons are circulating in the LHC in groups, called bunch trains. The maximum number of bunches in the LHC accelerator ring is defined by the settings of the RF system and correspond to 3564. Bunch spacing in the LHC Run II starting from 2015 was reduced from 50 *ns* to 25 *ns*.

The LHC tunnel is built of eight arcs and eight straight sections. The arcs are used to keep beams in a bended orbit and are equipped with superconducting dipole magnets with the highest operational magnetic field of 8.4 *T* at a current of 11.7 *kA*. Each magnet is placed in a cryostat and cooled with super fluid helium to 1.9 *K* [4]. To focus the beam, quadrupole magnets are employed. All magnets used in the LHC are listed in Ref. [5]. The straight sections of the tunnel are used for experiments or machine equipment.

The LHC is the last piece of a complicated multistage accelerator complex, where the performance of each step is extremely important to provide clean particle beams and to guarantee the required operation performance. The schematic of the CERN accelerator complex is shown in Figure 1.1. Protons are sourced from hydrogen at LINAC2, accelerated to an energy of 50 *MeV* and injected into the 157 *m* long Proton Synchrotron Booster, where they are accelerated to 1.4 *GeV*. At the next

step protons are injected into the Proton Synchrotron (PS) and accelerated up to 26 GeV and then in the Super Proton Synchrotron (SPS), where they are reaching the LHC injection energy of 450 GeV . For heavy ion collisions particles are sourced at LINAC3 and first accelerated in the other synchrotron, LEIR, then the same accelerator chain is used. The accelerator complex is also shared with other collaborations and experiments as the Isotope Separator On Line DEvice (ISOLDE), the radioactive ion beam facility [6], the neutron time-of-flight (n-ToF) experiment [7], the Advanced Proton Driven Plasma Wakefield Acceleration Experiment (AWAKE) [8] and the Extra Low ENergy Antiproton (ELENA) experiment [9].

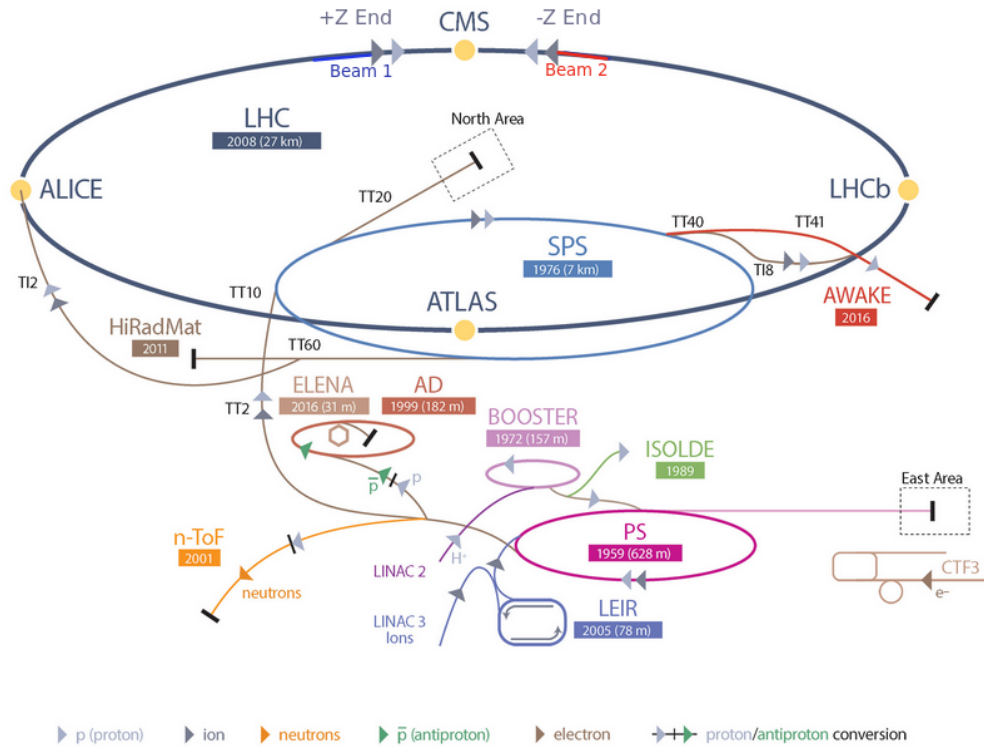


Figure 1.1: The schematic of the CERN accelerator complex.

1.2 Experiments at the LHC

The circulating beams are colliding at four IPs, where the main LHC experiments have been constructed. These are ATLAS, CMS, ALICE, LHCb, as is shown in Figure 1.2. There are also two smaller experiments (LHCf and TOTEM), situated close to IP next to the main experiments.

ATLAS (A Toroidal LHC ApparatuS) [10, 11] and **CMS** (Compact Muon Solenoid) [12, 13] are large multipurpose experiments. Both experiments have a cylindrical structure with end-caps on both ends and consist with growing radius of a tracker, calorimeter and muon systems. ATLAS is instrumented with an inner solenoid and eight toroidal magnets to create an outer magnetic field, whereas CMS is build with a single solenoid magnet. The CMS detector will be described in detail in subsection 1.4.

ALICE (A Large Ion Collider Experiment) [14] is dedicated to the study of heavy ion collisions with the focus on the quark-gluon plasma, a state of matter believed to be present shortly after the big bang. For these studies LHC provides heavy ion beams (Pb-Pb collisions).

LHCb (Large Hadron Collider beauty) [15] is an asymmetrically built with respect to the IP detector. It is specialized in B-physics. It carries out the investigation of phenomena possibly creating the imbalance of matter and anti-matter in an early state of the Universe.

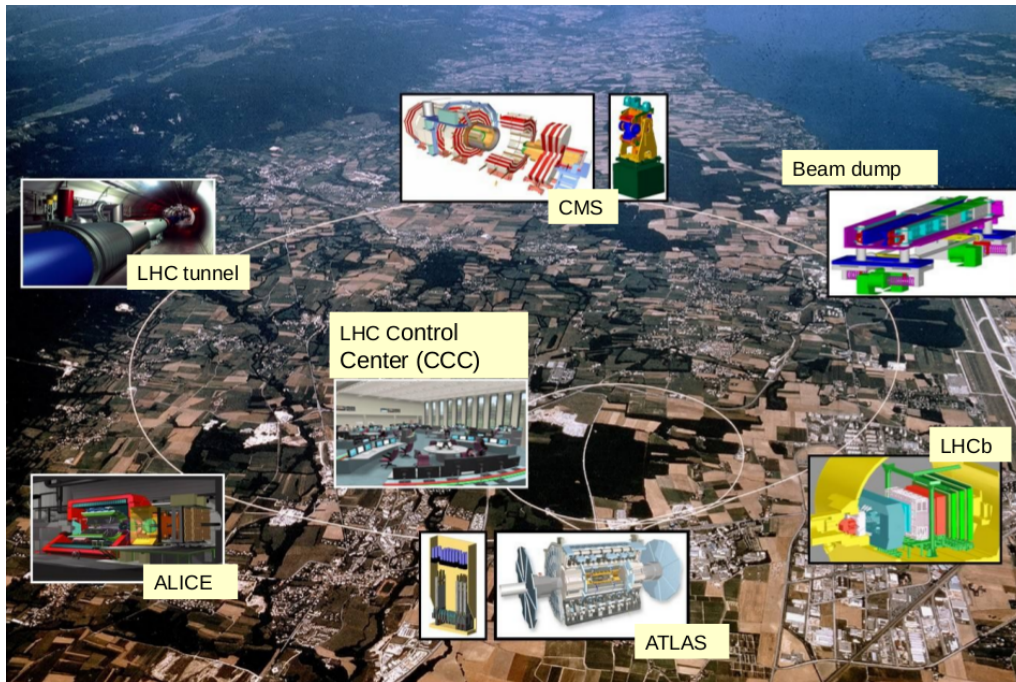


Figure 1.2: The approximate position of the LHC ring shown on the surface map with diagrams pointing to positions of the main experiments, the beam dump and the LHC control room.

LHCf (Large Hadron Collider forward) [16] is a smaller experiment, made up of two detectors which sit along the LHC beamline, at 140 m at either side of the

ATLAS experiment. It uses particles emitted by the collisions in the very forward direction or at nearly zero degrees to the proton beam direction. This study is needed for the understanding of cosmic rays cascades and helps to calibrate large-scale cosmic-ray experiments.

TOTEM (TOTal cross section, Elastic scattering and diffraction dissociation Measurement at the LHC) [17] is installed close to the CMS experiment. It is designed for proton-proton elastic cross section measurements at small polar angles. These measurements are complementary to the physics programs of the LHC general-purpose experiments.

Beam conditions are continuously monitored in the LHC control room and in case of high beam losses a beam dump is performed. There is a $3 \mu s$ gap in the filling scheme of the LHC, so-called abort gap, needed to ramp up the magnet for the beam dump. Locations of the LHC control room and beam dump are also shown in Figure 1.2.

1.3 Physics goals at LHC

One of the primary physics goal at the LHC is to prove electroweak symmetry breaking, which in the Standard Model is performed by the Higgs mechanism. In the interaction with a scalar field the fundamental particles acquire mass. An excitation of the scalar field, the Higgs boson, was predicted, but stayed the last undiscovered boson in the SM until 2012.

Its discovery was declared on the 4th of July in 2012. The mass of the Higgs boson, confirmed by both ATLAS and CMS, is about 125 GeV [18, 19].

After the discovery of the Higgs boson in Run 1, the analyses will be focused in Run 2 to fully explore the electroweak symmetry breaking. Quantum numbers, such as spin, parity, and CP and the couplings to bosons, fermions, and its self-coupling must be measured more precisely in order to determine whether there are any new physics contributions.

Of particular interest are also searches for extra dimensions, dark matter candidates, SUpEr SYmmetry (SUSY) and unexpected phenomena. All of this together with the Higgs measurements and precise measurements of the SM parameters motivates the large physics program for the general purpose experiments.

1.4 The CMS Experiment

CMS is designed according to the specifications summarized in Ref. [13]. The most important ones are: a good muon identification and momentum resolution, 1% di-muon, di-photon and di-electron mass resolution at 100 GeV , high momentum

resolution and reconstruction efficiency in the inner tracker, good electromagnetic energy resolution in the electromagnetic calorimeter and good missing-transverse-energy resolution in the hadronic calorimeter.

To match the LHC physics program requirement, the CMS was designed not only to reach the required resolutions, but also to deal with high particle rates and radiation damage. At the luminosity of $10^{34} \text{ cm}^{-2} \text{ s}^{-1}$ about 20 inelastic collisions are expected in one bunch crossing. This implies that around 1000 charged particles will emerge from the interaction region every 25 ns. To prevent pile-up effects fine granularity of the detectors and precise synchronization of subsystems are required.

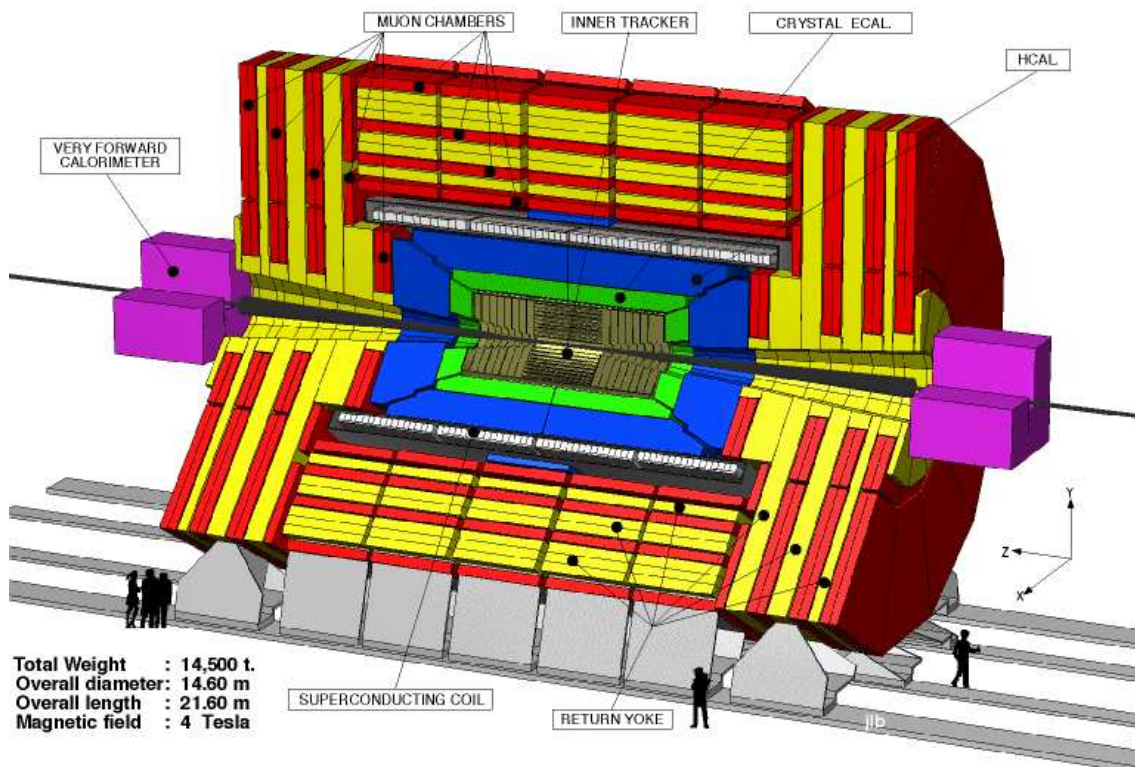


Figure 1.3: The schematic of the CMS detector.

The schematic layout of the CMS detector is shown in Figure 1.3. To be able to distinguish between different types of charged particles and to reconstruct tracks a set of subsystems is used. They are built in cylindrical layers on top of each other around the beam pipe. Cylinders are closed with the end caps to detect particles scattered at smaller polar angle. Tracking detectors are positioned around the beam pipe, surrounded by calorimeters, a superconducting magnet and a muon detection

system as the most outer part.

The CMS coordinate system is oriented such that the x -axis points south to the center of the LHC ring, the y -axis points vertically upward and the z -axis is in the direction of the beam to the west, as shown in Figure 1.3. The azimuthal angle ϕ is measured from the x -axis in the xy plane and the radial coordinate in this plane is denoted by r . The polar angle θ is defined in the rz plane.

The Superconducting Magnet is one of the main distinguishing features of CMS. It is 13 m long, 7 m in diameter and operated at 3.8 T to guarantee large bending power, needed for precise measure of the momentum of high-energy charged particles. The tracker and calorimeters are installed inside the coil.

The Tracking System is comprised of a silicon pixel and a silicon micro-strip detector. The trajectories of particles bended in the 3.8 T magnetic field are reconstructed to the IP. The most outer part of the tracker is 5.8 m long and 2.6 m in diameter. The resolution of the impact point of a particle in x is better than 13 μm and in z better than 33 μm . The resolution for the transverse momentum at $p_T = 1 \text{ GeV}$ is about 0.7% [20].

The silicon pixel detector is the closest to the IP. Three-layers of silicon pixel sensors are surrounding the beam pipe. Its construction is described in more detail in subsection 2.5.2. The strip tracker at larger radii is comprised of four parts. The inner-most contains four concentric barrel layers, called the Tracker Inner Barrel (TIB). It is covered with six more barrel detector layers forming the Tracker Outer Barrel (TOB). The TIB is closed with Inner Discs (TID) and the TOB with tracker end-cups (TEC).

To describe the angle θ between the particle traveling with momentum p and the beam axis, covered by the detector, a quantity called pseudorapidity is used. It is defined as:

$$\eta = -\ln[\tan(\theta/2)], \quad (1.1)$$

The tracker covers the pseudorapidity region up to $|\eta|=2.4$.

The CMS tracker plays a very important role in **the High Level Triggers** used for reduction of the data rate, while keeping the interesting events. First a threefold coincidences in the silicon pixel layers are searched for, then the track finding algorithm tries to reconstruct the track in the strip tracker, associates it with the vertex and defines the initial trajectory. After the trajectory is estimated, compatible hits are searched for in the calorimeter and muon system.

The Electromagnetic Calorimeter (ECAL) consists of a barrel part and end-caps made of about 68 000 lead tungstate $PbWO_4$ scintillating crystals. It is shown in dark green in Figure 1.3. For the readout silicon Avalanche Photodiode (APD) detectors are used. The end-caps include a Si-Pb pre-shower detector to separate single photons from π^0 decays into two photons. In the ECAL the two photons are

reconstructed as one shower, however in the pre-shower two showers are visible. The ECAL ages due to radiation and gains need to be adjusted over time, as well as with temperature changes. With end-cap calorimeters ECAL reaches the pseudorapidity up to $|\eta|=3.0$. One of the most challenging aspects of the ECAL is achieving the required 0.5% constant term of the energy resolution for unconverted photons, which is very important for Higgs boson analyses in related decay channels [21, 22].

The Hadronic Calorimeter (HCAL) is a sampling calorimeter built from alternating layers of plastic scintillator and absorber. It is designed for the energy measurement of hadronic jets and neutral hadrons. HCAL consists of a barrel (HB), an outer part (HO), an end-caps (HE) and an additionally installed forward calorimeter (HF). The end-cap calorimeters reach the pseudorapidity up to $|\eta|=3.0$, HF extends it up to $|\eta|=5.0$. It is shown in blue in Figure 1.3. The HF is also used for luminosity measurements and is described in subsection 2.5.1. The performance of the HCAL is important for Higgs and SUSY analyses. Based on these analysis the motivation and the concept of the HCAL upgrade is described in Ref. [23].

The Muon System is the most outer part of the CMS, designed for identification and momentum measurement of muons. Only muons are able to penetrate the calorimeters and reach the outer part. The muon system is of crucial importance for the ZZ decay channel in the Higgs analysis, with ZZ further decay to four muons. This is a signature with almost no background.

The Muon System is placed outside of the magnet coil. To return the magnetic field, the iron yoke outside of the magnet is employed, including 3 end-cap disks per end and 5 barrel wheels. The iron yoke is shown in green in Figure 1.3. It allows the magnetic field inside the iron to reach about 2 T. Three subsystems are used for muon detection: four layers of the Drift Tubes (DT), shown in Figure 1.3 in orange are installed alternating with yoke in the barrel part, the Cathode Strip Chambers (CSC) in the end-caps and Resistive Plate Chambers (RPC) in the barrel and end-caps. CSCs and RPCs are installed in addition to DTs because of their fast response required for first level trigger. DT covers the pseudorapidity range up to $|\eta|=1.2$ and reaches a spatial resolution of $100 \mu m$. The CSC covers $0.9 < |\eta| < 2.4$, and the spatial resolution is less than $150 \mu m$. The RPC covers $|\eta| > 1.6$ and a spatial resolution of 1 cm is reached [24].

Chapter 2

Measurement of the luminosity at colliders

The luminosity is a key parameter of each collider experiment for determining its physics potential in terms of normalizing its event statistics. The precise measurement of the luminosity is of crucial importance, since the uncertainty of the luminosity translates directly to the uncertainty of cross section measurement. A high luminosity is needed to measure low cross sections, as in Higgs measurements or SUSY searches [25–34]. For processes of high cross section, as W and Z boson production [35], the luminosity uncertainty is often the dominant uncertainty. It is illustrated in Figure 2.1, showing the ratios of the experimental to theoretical cross sections and ratios of cross sections for W and Z bosons. The shaded box indicates the uncertainty in the luminosity measurement. The inner error bars represent the experimental uncertainties, the outer error bars also include the uncertainties in the theoretical predictions.

In addition, the bunch-by-bunch luminosity measurement is important for accelerator diagnostics and optimization. To provide an uninterrupted luminosity measurement and to allow a permanent cross check to trace back in real time possible detector malfunction, more than one luminometer is beneficial for the experiment.

Operation at the highest possible luminosity is required for exploring the lower cross section processes. After the first scheduled long LHC maintenance period LS1 the LHC was expected to operate at bunch spacing of 25 ns and an energy of 6.5 TeV per beam. To operate at the nominal luminosity of $10^{34} \text{ cm}^{-1}\text{s}^{-1}$ with bunches of intensity of $O(10^{11})$ protons [36], the luminometers of CMS were upgraded or redesigned, as it will be described further in this Chapter. To keep linear response of the luminometers in the new operating conditions of the LHC, the granularity of the detectors and readout electronics had to be improved.

After LS1 the CMS experiment was running with three independent online luminometers: the Hadron Forward calorimeter, the Pixel Luminosity Telescope (PLT)

and the Fast Beam Conditions Monitor.

Along with the luminosity, it is important to measure MIB [37]. MIB is generated by interactions of beam particles with residual gas molecules in the vacuum chamber. This MIB component is known as “beam gas”. Another source of MIB is the interactions of off-momentum beam particles with collimators, known as “beam halo”.

MIB particles move almost parallel to the incoming beam. An increase of the MIB background is an indication of bad beam quality or bad vacuum in the beam pipe that may affect the data taking performance. The systems used for online machine induced background measurements are the BCM1F, the Beam Condition Monitor “Leakage” (BCML) and the Beam Halo Monitor (BHM), described in subsection 2.4.

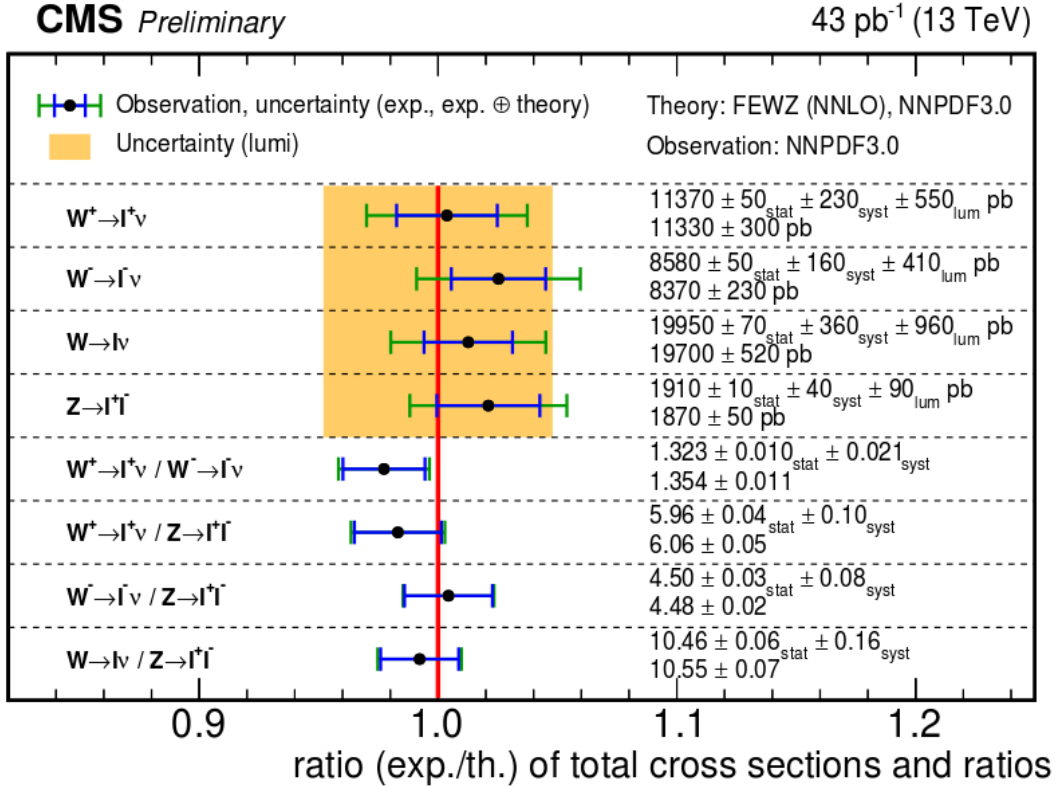


Figure 2.1: Summary of total inclusive W^+ , W^- , W and Z production cross sections times branching fractions, W to Z and W^+ to W^- ratios, and their theoretical predictions [35].

2.1 Absolute luminosity from machine parameters

The absolute luminosity at the LHC is determined from machine parameters, which do not require the knowledge of particle cross sections.

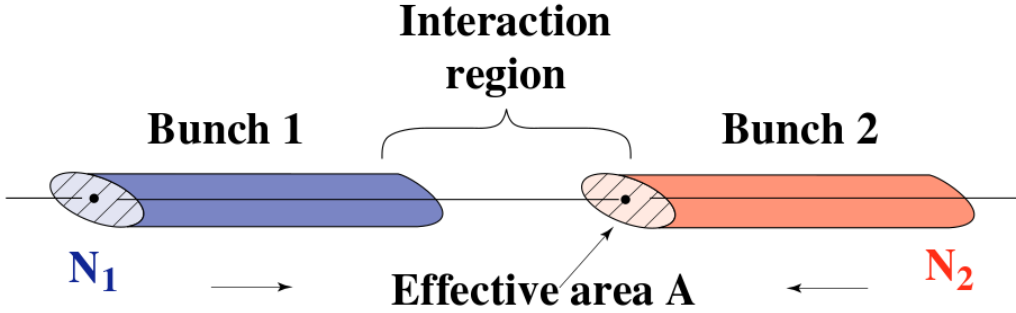


Figure 2.2: Illustration of a bunch crossing with the relative parameters [38].

For colliding bunches with N_1 and N_2 numbers of particles, as shown in Figure 2.2, the luminosity is defined as:

$$L = \frac{N_1 \cdot N_2 \cdot f \cdot n_b}{A_{eff}}, \quad (2.1)$$

where n_b is the number of colliding bunches, f is the revolution frequency in the collider and A_{eff} is the area of the luminous region. The quantities N_1 , N_2 , f and n_b are obtained from measurements of the LHC machine. The luminous region, assuming Gaussian particle density distributions in the colliding bunches [38], is given as:

$$A_{eff} = 4\pi \cdot \sigma_x \cdot \sigma_y, \quad (2.2)$$

where σ_x and σ_y are the Gaussian widths of the lateral particle density distributions in the bunches. To achieve a high luminosity, the beams must be focused at the interaction point into as small as possible of an effective area.

The width of the luminous region is needed for the luminometers calibration and obtained from the VdM scans, as described in section 2.2.

2.2 Calibration of luminometers

Any detector which can measure particle hit rates and provide a linear dependency of the signal as a function of the luminosity can be used as a luminometer. For

calibration of the luminometers special experimental conditions are created – van der Meer scans – a method originally proposed by Simon van der Meer and first exploited at the CERN ISR [39]. Here the general idea of the method will be discussed and in particular the BCM1F detector calibration will be described in Chapter 4.

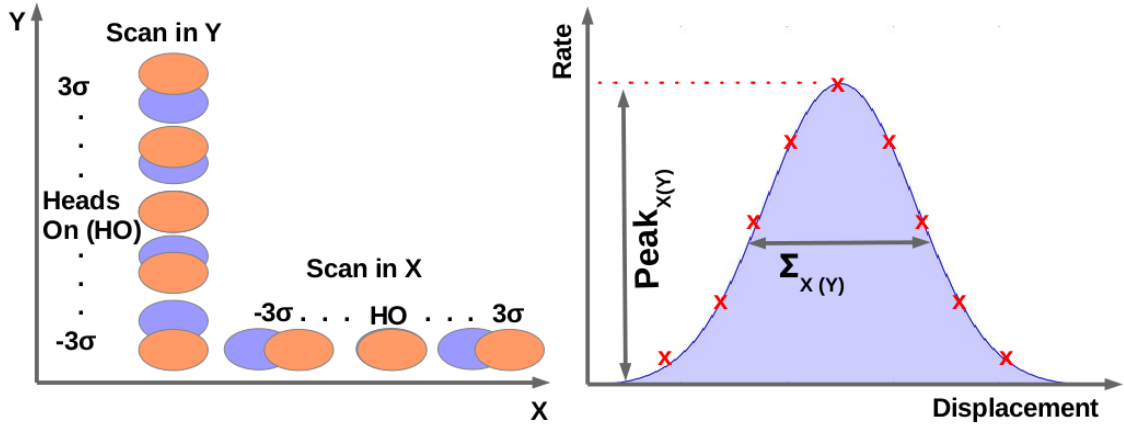


Figure 2.3: Left: Illustrative sketch of the VdM scans in x and y planes. Right: Sketch of the luminometer rates as a function of displacement obtained from the VdM scan.

The VdM method consists of scanning colliding bunches against each other in the plane transverse to the beam axis in order to determine their overlap region. The two beams are moved with respect to each other in steps in the x and then in the y plane, and the rate R is measured by the luminometers. The procedure of the VdM scan is illustrated in Figure 2.3 on the left side for a maximum beam separation of 3σ . The position of the beams with no separation is called head-on. It corresponds to full overlap of the bunches and is shown on the sketch with an orange ellipse. The maximum measured rate is achieved at full overlap.

The measured rates for different displacements are shown with red crosses in Figure 2.3 on the right. The distribution of the rates as a function of the displacements for two Gaussian beams is also a Gaussian. From the distributions of rates as a function of the beam displacements in the x and in the y planes the widths in x and y , denoted hereafter as Σ_x and Σ_y , were obtained by a fit. Denoting the average maximum rate in x and y as R_{peak} , and using the values measured for Σ_x and Σ_y , the visible cross section of the luminometer reads:

$$\sigma_{vis} = \frac{2\pi\Sigma_x\Sigma_y}{N_1 \cdot N_2 \cdot f \cdot n_b} \cdot R_{peak}. \quad (2.3)$$

Thus, determining the visible cross section once, the measured count rate is used to measure the luminosity as:

$$L = R/\sigma_{vis}. \quad (2.4)$$

For better understanding of the assumptions used in the VdM method, we will define the visible cross section using particle density functions ρ_1 and ρ_2 per-bunch in beam 1 and beam 2. The per bunch crossing luminosity [40] reads using particle density functions as:

$$L(\Delta_x, \Delta_y) = N_1 N_2 \int \rho_1(x, y, z + ct) \rho_2(x - \Delta_x, y - \Delta_y, z - ct) dx dy dz dt, \quad (2.5)$$

where Δ_x and Δ_y are the relative beam displacements in the plane transverse to the beam axis, c is the speed of light, $N_{1,2}$ are the numbers of particles in the bunches of beam 1 and beam 2, respectively. The particle density functions in the laboratory frame are normalized to:

$$\int \rho_{1,2}(x, y, z) dx dy dz = 1. \quad (2.6)$$

The key idea of the VdM scan is to assume that the three-dimensional particle density functions $\rho_{1,2}(x, y, z)$ can be factorized as products of three independent one-dimensional functions:

$$\rho(x, y, z) = \rho_x(x) \rho_y(y) \rho_z(z), \quad (2.7)$$

normalized to:

$$\int \rho_x(x) dx = \int \rho_y(y) dy = \int \rho_z(z) dz = 1. \quad (2.8)$$

The dependence on the longitudinal coordinate z drops out due to integration over time. Eq. 2.5 reduces to the product of two one-dimensional integrals:

$$\begin{aligned} L(\Delta_x, \Delta_y) &= \nu N_1 N_2 \left[\int \rho_{x1}(x) \rho_{x2}(x - \Delta_x) dx \right] \times \left[\int \rho_{y1}(y) \rho_{y2}(y - \Delta_y) dy \right] \equiv \\ &\equiv \sigma_{vis} R(\Delta_x, \Delta_y), \end{aligned} \quad (2.9)$$

where ν is the beam revolution frequency ($\nu = 11245.6 \text{ Hz}$ for the LHC), $R(\Delta_x, \Delta_y)$ is the rate of the luminometer as a function of the beam displacements Δ_x and Δ_y , and σ_{vis} is the visible cross section.

It is important to point out that σ_{vis} is used as a calibration constant, and is independent of the beam displacements Δ_x and Δ_y . Therefore integration over Δ_x of both sides of Eq. 2.9 and using normalization Eq. 2.8 results in:

$$\nu N_1 N_2 \left[\int \rho_{y1}(y) \rho_{y2}(y - \Delta_y) dy \right] = \sigma_{vis} \int R(\Delta_x, \Delta_y) d\Delta_x, \quad (2.10)$$

and integrating over Δ_y , similarly,

$$\nu N_1 N_2 \left[\int \rho_{x1}(x) \rho_{x2}(x - \Delta_x) dx \right] = \sigma_{vis} \int R(\Delta_x, \Delta_y) d\Delta_y. \quad (2.11)$$

Substituting Eqs. (2.10) and (2.11) into (2.9) and expressing the luminosity $L \equiv L(0, 0)$ in terms of the interaction rate $R(\Delta_x, \Delta_y)$ and the bunch multiplicities N_1 and N_2 , one obtains the following expression for the visible cross section:

$$\sigma_{vis} = \frac{\nu N_1 N_2 R(0, 0)}{[\int R(\Delta_x, 0) d\Delta_x] \times [\int R(0, \Delta_y) d\Delta_y]}. \quad (2.12)$$

Eq. 2.3 and 2.12 determine visible cross sections in alternative ways. In Ref. [40] the visible cross section calculation is done using areas under the $R(\Delta_x, 0)$ and $R(0, \Delta_y)$ distributions as well as the zero-separation values $R(0, 0)$. They are defined either by fitting the distributions by appropriate functions and evaluating the area and the zero-separation value from the fit parameters or by using a ‘‘bin counting’’ method. For our study Eq. 2.3 was used and beam width as well as R_{peak} value were extracted from the fit.

2.3 Luminosity calculation using physics cross section

The collision rate N_{col} for a process of known cross section σ_{crop} produced by a machine running with luminosity L is:

$$N_{col} = L \sigma_{proc}. \quad (2.13)$$

If the cross section for a process is known, the luminosity can be measured from this relation from the observed event rate. In e^+e^- colliders, the theoretically well known $e^+e^- \rightarrow e^+e^-$ scattering or Bhabha process was often used for this purpose [38, 41]. For pp collisions at the LHC at 14 TeV c.m.s energy, the rate of W and Z production is high [35] and it is believed to be suitable for luminosity calculation in the future, if precision of the calculation of the cross section for W and Z production would be improved.

When considering bunched beams, the per-bunch instantaneous luminosity L is proportional to the number of collisions per bunch crossing μ . The number of interactions based on the pp minimum bias cross section σ_0 is known to be related with luminosity as:

$$L = \frac{f}{\sigma_0} \mu, \quad (2.14)$$

where f is the LHC orbit frequency.

Such a luminosity calculation is limited by the precision of the predicted cross section σ_0 , therefore the measurement of luminosity only using machine parameters is used at LHC.

2.4 Beam Radiation, Instrumentation and Luminosity project

Several groups of beam monitoring systems, online luminometers and MIB monitors are organized under the CMS Beam Radiation, Instrumentation and Luminosity (BRIL) project. The higher luminosity, beam energy and denser bunch spacing after LS1 required an upgrade of the Run I systems. In addition, as a new luminometer the PLT and as a background monitor the BHM were designed, built, commissioned and installed [42]. After 2014 CMS was equipped with three independent online per-bunch luminometers: the upgraded HF, the newly installed PLT and the upgraded BCM1F. The last one is also used for MIB measurements, as well as BHM, composing together two independent measurements of MIB at different radii.

The systems are positioned to provide complementary measurements and maximize exposure to signal, as illustrated in Figure 2.4. Each of them will be described in more detail in the following sections.

The BRIL subsystems are synchronized using common timing signals distributed by the CMS Trigger, Control and Distribution System (TCDS). A common architecture for the data acquisition and analysis from all subsystems was developed based on the CMS XDAQ online software framework to provide fast feedback to the LHC and CMS control rooms.

The Beam Condition Monitor “Leakage”

To guarantee safe operation of the tracker, the BCML system is used [43]. The upgraded beam condition monitor 1 (BCML1) is based on 8 polycrystalline CVD (pCVD) diamond sensors of 1 cm^2 area, 4 sensors per side, 1.8 m from the interaction point. BCML1 is positioned in the tracker volume at the outer radius of the BCM1F PCB, about 4.5 cm around the beam pipe. The position of the subsystem is shown in Figure 2.4. The diamond sensors are used as current monitors, as the current through the sensors is proportional to the particle flux. If the current through the sensor reaches a predefined threshold, the system sends a signal to the LHC control room to dump the beam.

The upgraded beam condition monitor 2 (BCML2) uses 24 pCVD diamond sensors, 12 diamonds per side, around 12.4 m away from the IP. Four diamond sensors are mounted at a radius 5 cm and 8 at a radius of 28 cm around the beam pipe.

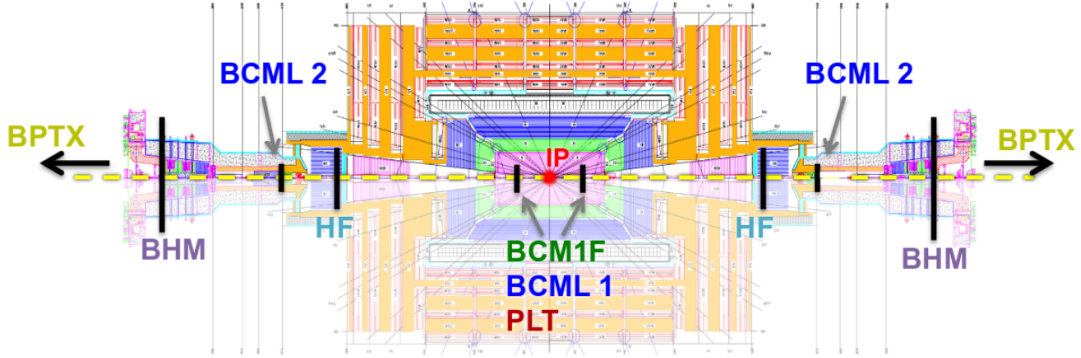


Figure 2.4: Schematic view of the CMS detector with arrows pointing to the BRIL subsystems location.

Also BCML2 sensors are used as current monitors and provide a beam abort signal. In addition, sapphire sensors are installed at the BCML2 location for commissioning and study of the signal in comparison to diamond sensors. Sapphire sensors are not included in the beam abort.

Since BCML is included in the beam dump, exceptional reliability is required. As a safety system it is also included in the CMS Beam Interlock Controller.

The Beam Pick-up Timing for experiment

The Beam Pick-up Timing for experiment (BPTX) is used for bunch arrival time, intensity and bunch length measurements [44, 45]. Each BPTX station uses standard LHC beam position monitors (BPM) comprised of four electrostatic button electrodes positioned symmetrically around the beam-pipe 175 *m* from the IP. The signals from BPTX detectors arrive in the counting room and are connected to a 5 Giga-samples oscilloscopes. For timing one oscilloscope per side is used, performing a full waveform readout (contains information about the whole orbit) and analysis. The analysis takes about 15 *s*. For bunch intensity and length measurements another oscilloscope is used, the analysis of full waveform takes about 30 *s*.

Typical signals measured by the oscilloscope are bipolar, as it is shown in Figure 2.5. The point, where BPTX bipolar signal crosses the baseline is used for timing, Figure 2.5 a). The measured bunch timing is phased with respect to the LHC clock. The phase is defined as the difference between the measured bunch arrival time and the LHC clock signal edge. The intensity of the bunch is calculated as the integral of the positive part of the signal (Figure 2.5 b)) and the Full Width

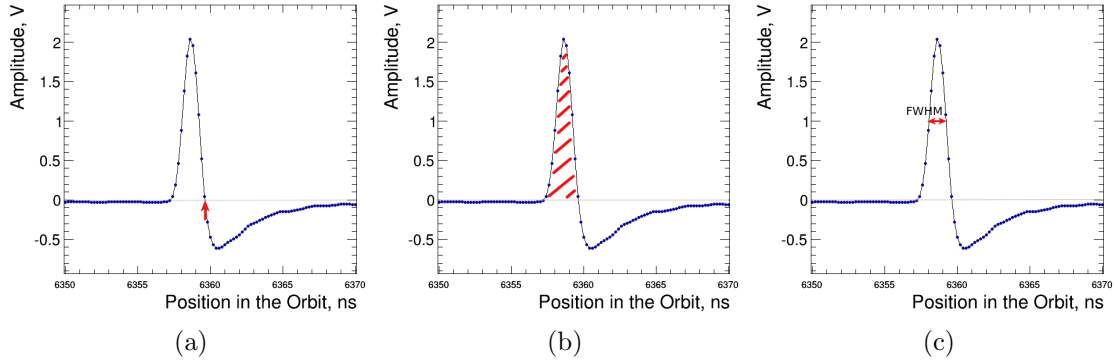


Figure 2.5: An example of the BPTX detector response to one proton bunch. a) The point, where BPTX bipolar signal crosses the baseline is used for arrival time with respect to the LHC clock measurement. b) The integral of the positive part of BPTX signal is proportional to the total charge of the given bunch and used for bunch intensity measurement. c) The FWHM of the positive part of BPTX signal is taken as a measurement of the bunch length.

at the Half Maximum (FWHM) of the same part of the signal is taken as the bunch length (Figure 2.5 c)).

BPTX is needed for checks of the number of bunches filled in the LHC, the time difference between two colliding bunches, and used to predict the z position of the collisions before stable beams are declared. The BPTX signals are also used to provide gating for the background and luminosity measurements performed by the the BCM1F detectors.

2.4.1 New pixel luminosity telescope

The PLT is a new CMS luminometer based on silicon pixel sensors [46], bump bonded to the PSI46v2 CMS pixel readout chip (ROC) [47], the same as used in the CMS barrel pixel detector. A ROC with a mounted sensor is called a PLT Hybrid board and is shown in Figure 2.6 on the left. Sensors are located radially 5 cm away from the beam line, around 1.75 m distance from the CMS IP. Four Hybrid boards are mounted onto one plane of the cassette, which provides also cooling. It is produced from a titanium alloy using the selective laser melting (SLM) technique. Three equally spaced hybrids board form a telescope of about 7.5 cm length, as shown in Figure 2.6 on the right.

Three hybrid board planes of one telescope are connected by “pigtailed” to the High Density Interconnect (HDI), a four-layer flex circuit. The HDI houses a CMS

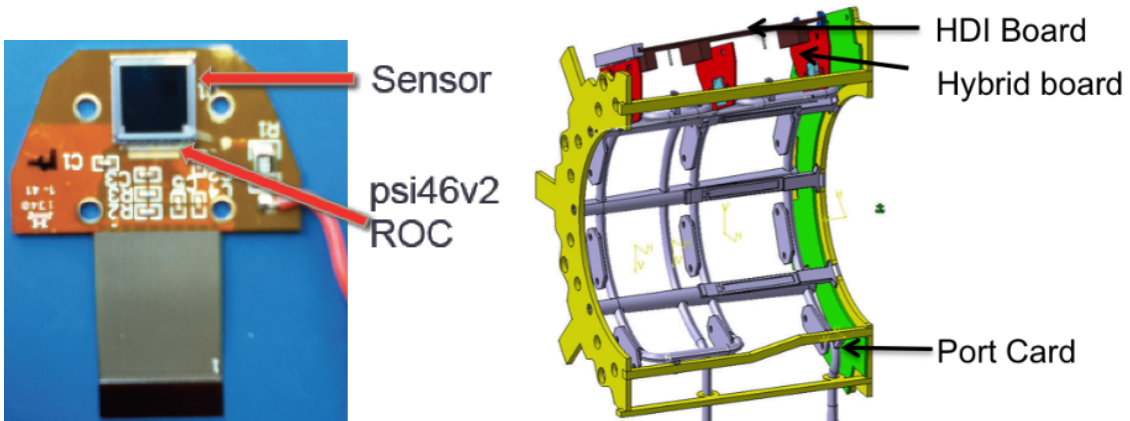


Figure 2.6: Left: The silicon PLT hybrid board. Right: PLT cassette providing the frame for electronics, alignment components and cooling distribution [42].

pixel Token Bit Manager (TBM) chip that communicates with the three readout chips in the telescope and coordinates the readout of the full sensor information. The HDI circuits connect to a semi-circular port card board, one port card for each half carriage and then to an opto board. From the opto board analog signal fibers connect to a Front End Driver (FED), where the histogramming of the 40 MHz, fast-or signals is done.

The primary luminosity measurement of the PLT is based on counting the number of the threefold coincidences of the fast-or output as a function of the bunch crossing (BX). The fast-or signal, clocked at the bunch crossing frequency of 40 MHz, indicates the number of double columns with pixels over threshold in each bunch crossing. In addition, the full hit information consisting of the row and column addresses and the pulse heights of all signals over threshold is readout at a lower configurable frequency of a few kHz. This full pixel readout provides tracking information and is a powerful tool for determining systematic corrections, calibrating pixel efficiencies and measuring the collision point centroid as a function of time [42].

2.4.2 The Fast Beam Condition Monitor

The BCM1F is diamond-based detector with about 1 ns arrival time resolution. It has been in operation in CMS since 2008 [48–50]. During LS1 it was upgraded to match Run II LHC requirements: a new PCB was developed, the number of channels increased from 8 to 48 and a new fast front-end ASIC was designed. The front-end and back-end of the BCM1F will be described in detail in Chapter 3. The

upgraded BCM1F is installed at a radius of 6.94 cm from the beam axis, 1.8 m away from the CMS IP. Due to its excellent time resolution and specially selected location BCM1F is used for both, luminosity and MIB measurements. Incoming machine induced background particles and outgoing collision products are separated in time by 12.5 ns . It is important to mention that the BCM1F C-shaped PCB is assembled in the one carbon fiber support carriage with PLT and also BCML1 detectors mounted on it, as seen in Figure 2.7. As a whole system is installed in the most inner part of the CMS, it had to fit in a very limited space and to fulfill efficiency and radiation hardness requirements. It is a masterpiece of beam-instrumentation engineering. A more detailed drawing of the carriage is shown in Figure 2.8.

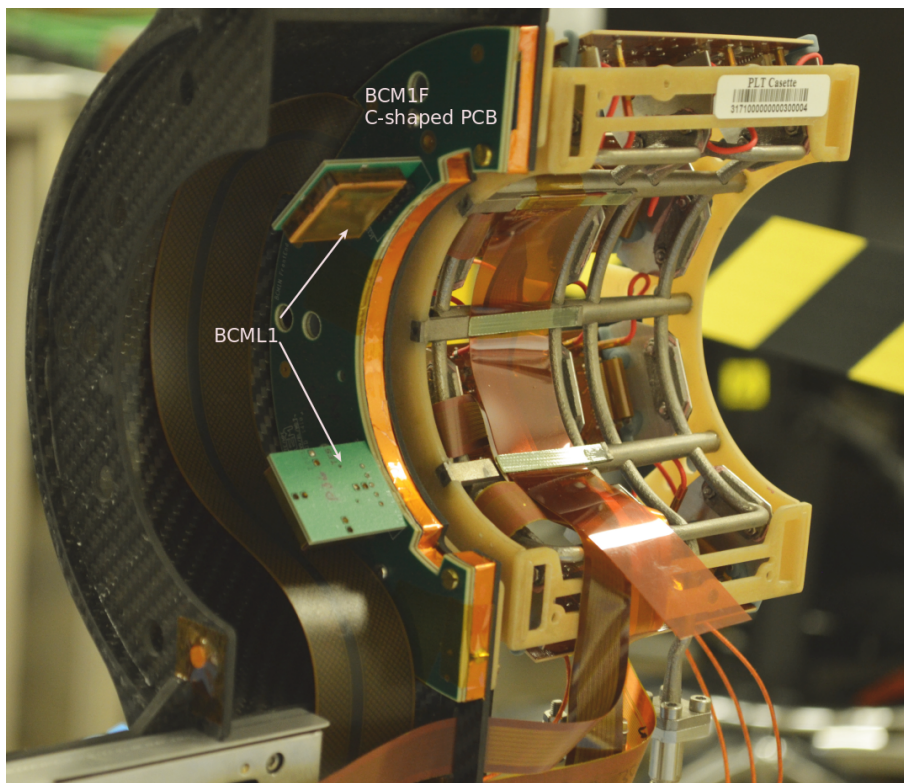


Figure 2.7: Photo of the quarter of the PLT detector assembled with BCM1F C-shaped PCB and mounted BCML1 detectors in the carbon fiber support carriage ready for installation.

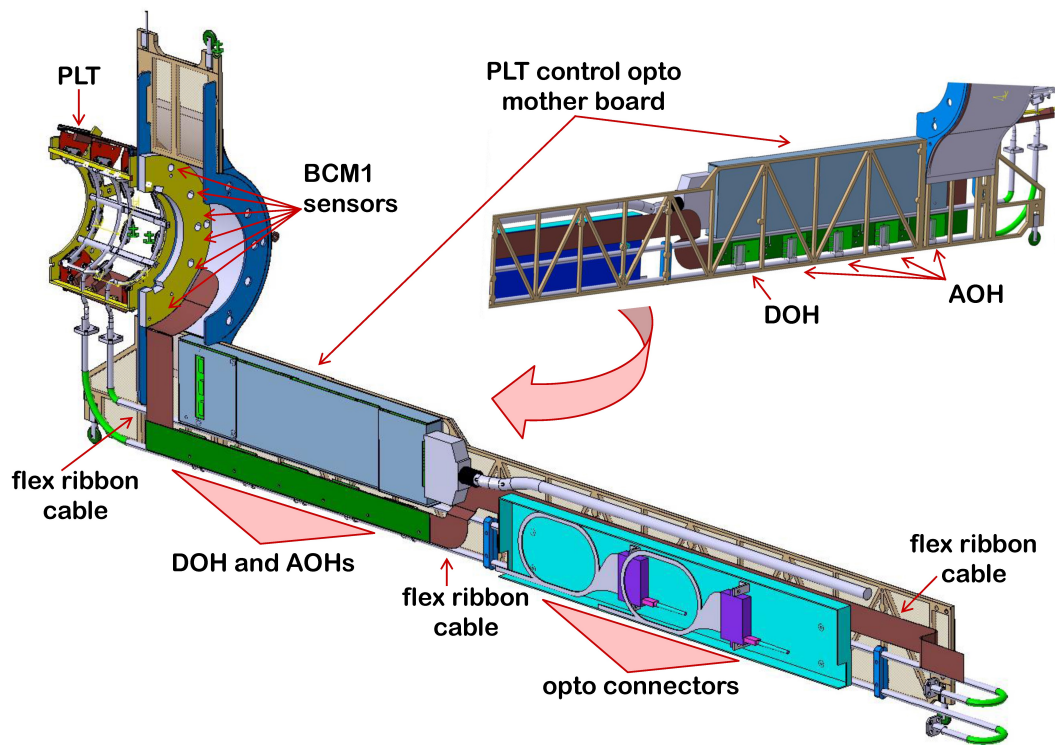


Figure 2.8: Detailed drawing of the PLT/BCM1F/BCML1 carbon fiber support carriage.

Zero counting algorithm

During the operation of BCM1F, hit rates are measured in each channel. Each channel can be handled as an independent luminometer. Taking into account that the number of hits per bunch crossing follows a Poisson distribution, the probability of a certain number of hits, n reads:

$$p(n) = \frac{\mu^n e^{-\mu}}{n!}. \quad (2.15)$$

The probability that there is no hit, $p(0)$, is used to measure the mean value μ ,

$$\mu = -\ln[p(0)] = -\ln[1 - p(\neq 0)]. \quad (2.16)$$

Since the occupancy per channel is low this method is used to determine the mean value μ for the luminosity calculation.

2.4.3 The Beam Halo Monitor

The BHM is a new system designed, built and installed in the CMS during LS1, as part of the upgrade of the CMS background monitoring instrumentation [55]. The BHM modules are positioned azimuthally outside the rotating shielding of the CMS about 20.6 m away from the CMS IP at a radius of 1.8 m from the beam axis. It is used for the measurement of the MIB arriving at high radius from the LHC tunnel. Twenty detectors per end are placed pointing towards the LHC tunnel. Mainly muons, originating from the interactions of the beam halo of the LHC beams with the collimators and traveling almost parallel with the incoming beam, are measured. The time resolution of 0.6 ns allows a bunch-by-bunch measurement of the MIB and in addition allows separation of MIB hits from collision products. It is independent and complementary to the BCM1F MIB measurement.

The BHM is sensitive only to relativistic charged particles. It is a Cherenkov quartz radiator of 10 cm length and 5.1 cm diameter read out by a UV sensitive photo-multiplier tube. Directional nature of the Cherenkov light is employed to obtain directional sensitivity of the BHM. The front side of the quartz radiator is covered with a light-absorbing black paint and the photo-multiplier is connected to the back side. Difference in the BHM response to the forward and backward-moving particles is shown in Figure 2.9. The integrated signal charge is more than one order of magnitude higher for forward moving particles.

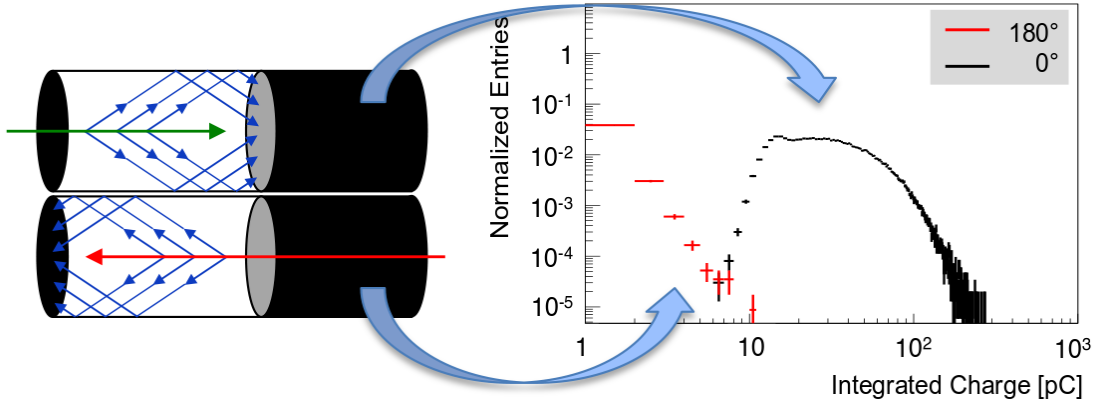


Figure 2.9: Illustration of the difference of the BHM detector response to the forward and backward particles [56].

2.5 Other luminometers of the CMS

2.5.1 The Hadron Forward calorimeter

The HF is a quartz fiber calorimeter and extends the CMS Hadron calorimeter to small polar angles. It is located 11.2 m away from the IP on both sides, covering the pseudo-rapidity range $3 < |\eta| < 5$.

The HF tower occupancy method was the primary method used at CMS for real-time bunch-by-bunch luminosity measurements already in Run I. As the logarithm of the average fraction of empty towers is proportional to the average interaction rate, also the zero counting method was used, as described in section 2.4.2. To minimize the non-linear contribution, only the four azimuthal rings of HF in the range $3.5 < |\eta| < 4.2$ were used for luminosity measurements [40], resulting in 864 towers.

For detection of the signal from towers, Photo Multiplier Tubes (PMTs) were used. As a result of gain changes in the PMTs, the HF luminosity measurement was affected by time-dependent changes. In addition, the detector response has been proved to be non-linear with pileup in the luminosity range of the 2012 LHC run. Therefore during LS1, as a part of the HCAL Phase I upgrade program, an upgrade of the HF was performed [23]. The PMTs were replaced with new multi-anode PMTs and the back-end electronics have been switched to the MicroTCA standard. New readout boards provide bunch-by-bunch occupancy and transverse energy sums

(“ $E_T sum$ ”), giving a linear relationship between the average transverse energy per tower and the luminosity.

2.5.2 Silicon pixel detector

The silicon pixel detector is the innermost component of the CMS tracking system. The sensors of the pixel detector are segmented into a total of 66 million pixels, each with the size $100 \mu m \times 150 \mu m$ [57].

It is designed for determining the trajectories of charged particles to determine the interaction point and the secondary vertex of heavy-flavor hadron decays with high precision. The pixel detector consists of a Barrel Pixel detector (BPIX) and a Forward Pixel detector (FPIX), based in hybrid pixel technology. The BPIX consists of three cylindrical layers of pixel modules oriented coaxially with respect to the beamline at 4 cm , 7 cm and 11 cm and centered around the collision point. The FPIX is located orthogonally to the beamline on each side of BPIX, extending to 2.5 in pseudorapidity $|\eta|$.

At Run II nominal instantaneous luminosity of $10^{34} \text{ cm}^{-2} \text{ s}^{-1}$ the detector occupancy per pixel per BX will not reach 0.1%. Hence, reading out the number of pixels provides excellent linearity. As the silicon pixel detector can only operate at stable beam conditions, it is only suitable for offline luminosity measurements. But its stability and linearity at high luminosity makes it a powerful tool for cross-checking the online luminometers.

Pixel cluster counting

The offline luminosity calculation is based on the Pixel cluster counting (PCC) method [95]. A cluster is a group of pixels with signal higher than the threshold and associated with one particle hit. Taking the number of collisions per crossing μ , the mean number of pixel clusters per bunch crossing is:

$$\langle N_{cluster} \rangle = \langle N_{cluster/interaction} \rangle \mu. \quad (2.17)$$

The PCC visible cross section can be defined as:

$$\sigma_{vis}^{PCC} = \langle N_{cluster/interaction} \rangle \sigma_0, \quad (2.18)$$

where σ_0 is the pp minimum bias cross section. Using Eqs. (2.14) and (2.17), the relation between the instantaneous luminosity and visible cross section can be written as following:

$$L = \frac{\langle N_{cluster} \rangle f}{\sigma_{vis}^{PCC}}, \quad (2.19)$$

The visible cross section is determined similar to online luminometers, using the VdM scan method discussed in Chapters 2 and 4.

2.6 Radiation simulations

As in Run II the peak nominal instantaneous luminosity is expected to reach $2 \times 10^{34} \text{ cm}^{-2} \text{ s}^{-1}$, with around 50 interactions per bunch crossing, twice the instantaneous luminosity foreseen in the initial LHC technical design report, it becomes critical to monitor the radiation damage in different locations. The BRIL project group works also on simulations of the radiation field in the full CMS detector and cavern using FLUKA [58] and MARS [59]. It is needed as well for detector hit rate predictions, estimations of the radiation damage and activation of materials and the design, development and optimization of the hardware [60,61]. An example of the particle fluence in silicon in the tracker region for a total integrated luminosity of 300 fb^{-1} obtained from FLUKA simulation in 1 MeV neutron equivalent for 7 TeV energy per beam is shown in Figure 2.10.

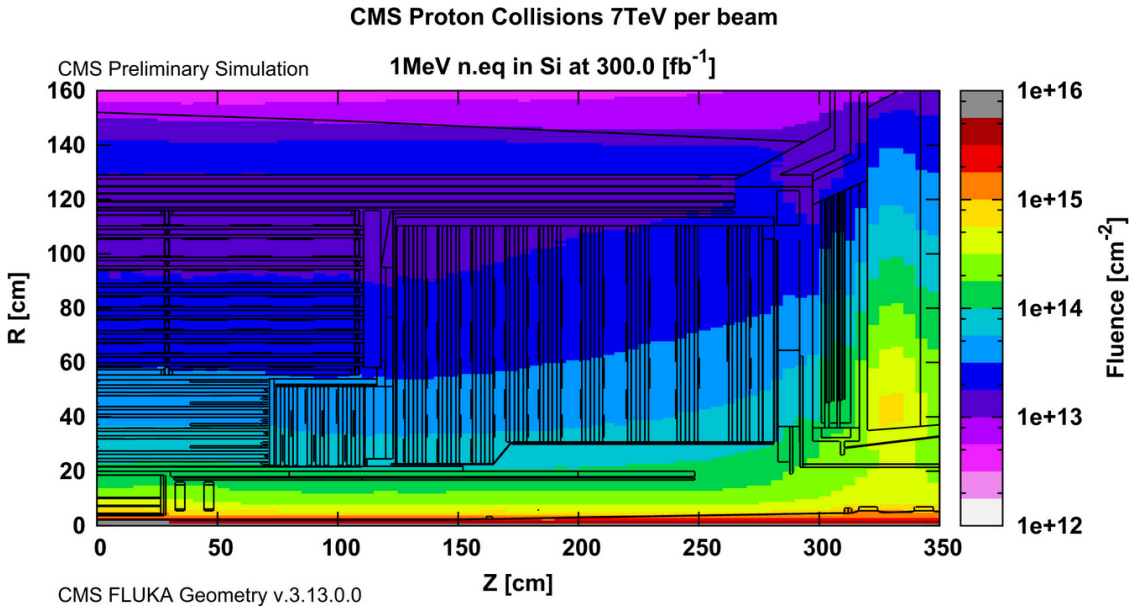


Figure 2.10: Estimation of the expected 1 MeV neutron equivalent fluence in silicon in the tracker region for a total integrated luminosity of 300 fb^{-1} ; collisions from 7 TeV proton beams were simulated [61].

Chapter 3

BCM1F detector as luminometer

3.1 The BCM1F

The BCM1F [49,50] is designed for bunch-by-bunch luminosity and machine induced background measurements. It is a part of the CMS BRIL Project. In 2014 it was upgraded and currently is based on 24 single crystal CVD (scCVD) diamond sensors. The sensors are placed on 4 half-ring PCBs (C-shapes) at a radius of 6.94 *cm* from the beam axis with almost equal spacing in the azimuthal angle, as is shown in Figure 3.1.

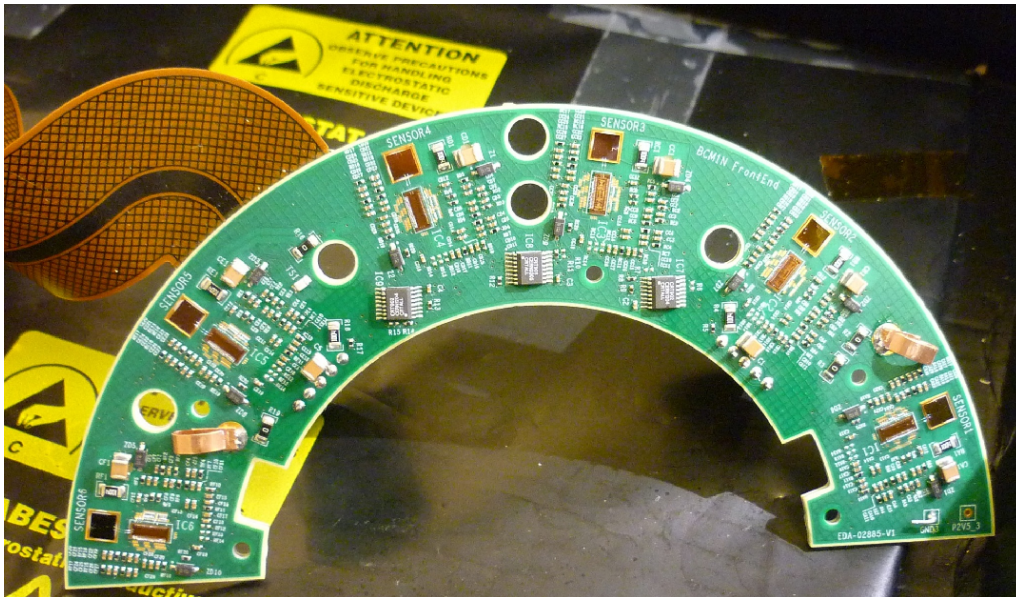


Figure 3.1: The C-shape assembled with 6 diamond sensors and front-end ASICs.

The half rings are combined into rings, positioned at a distance of 1.8 m in z on both ends of CMS around the interaction point (see Figure 1.1). C-shapes are named “+Z” or “-Z” with respect to the end from the interaction point and “NEAR” or “FAR” with respect to the center of the LHC ring. Resulting into names: +Z NEAR, +Z FAR, -Z NEAR and +Z FAR. The distance between the IP and C-shapes positions was chosen to benefit from the maximum time difference of 12.5 ns between incoming MIB particles and outgoing collision products as illustrated in Figure 3.2. Fast front-end electronics and excellent time resolution of the back-end electronics allows for the separation of hits originating from collisions and MIB, thus it is used for real time luminosity and MIB measurements.

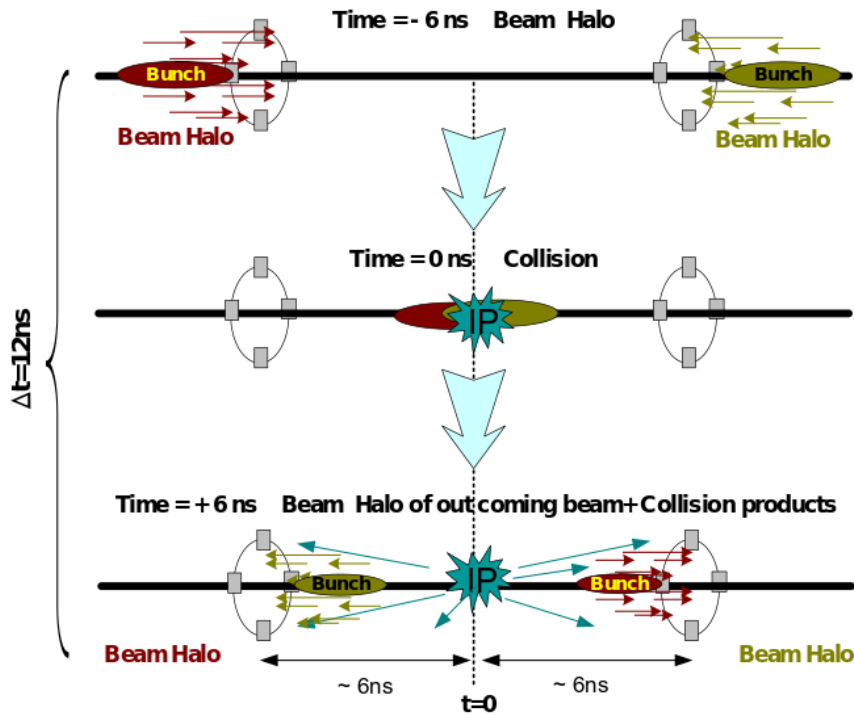


Figure 3.2: Schematic of arrival time for various beam products [50].

3.2 Diamond as a solid state detector

A charged particle traveling through diamond detector material interacts with atomic electrons and nuclei along its track, depositing energy in the detector material. Depending on the type of the collision, electrons can be moved to a higher atomic

bound state or kicked out of the atom, creating an electron-hole pair. The first process is called excitation, the second process is called ionization. In some cases the ionization can provide very high energy transfer to the electron which can continue to ionize other atoms. Such electrons are called δ -electrons.

The diamond sensors are metallized from both sides. Applying a bias voltage to the metallization, an electric field is created. Charge carriers produced by the ionizing particle drift towards the electrodes. The observed signal size depends on the deposited energy of the particle and the average energy needed to create an electron-hole pair. By repeating the measurement of the signal size a multiple number of times spectra are obtained. For a given setup, the signal size can be defined by the maximum of the signal or by the integral of the signal wave form over time.

The mean energy loss $\langle \frac{dE}{dx} \rangle$ due to ionization for relativistic charged heavy particle is described by the Bethe-Bloch formula [62]:

$$-\langle \frac{dE}{dx} \rangle = K z^2 \frac{Z}{A} \frac{1}{\beta^2} \left[\frac{1}{2} \ln \frac{2m_e c^2 \beta^2 \gamma^2 T_{max}}{I^2} - \beta^2 - \frac{\delta(\beta\gamma)}{2} \right], \quad (3.1)$$

where $K = 4\pi N_A r_e^2 m_e c^2$, N_A is Avogadro's number, r_e is the classical electron radius, $m_e c^2$ is the electron mass $\times c^2$, Z is the atomic number of absorber, A is the atomic mass of absorber, $\beta = v/c$ is the velocity of the particle, $\gamma = 1/\sqrt{1-\beta^2}$, T_{max} is the maximum kinetic energy that can be transferred to a free electron in a single collision, I is the mean excitation energy and $\delta(\beta\gamma)$ is the density effect correction to the ionization energy loss.

At low momenta, $0.1 < \beta\gamma < 3$, the energy loss decreases proportionally to $1/\beta^2$. At higher velocities ($\beta\gamma \gg 4$), the electric field surrounding the charged particle flattens and extends its influence at larger distances from the particle trajectory causing the logarithmic increase of the energy loss, called the relativistic rise. Between these two regimes a minimum of the energy loss is situated at $\beta\gamma$ around 3.5. Particles with $\beta\gamma=3.5$ or close to it are called Minimum Ionizing Particles (MIPs). Above $\beta\gamma=100$ deceleration due to interactions with the atomic nucleus, called bremsstrahlung, and direct pair production become dominant. The intensity of bremsstrahlung is inverse proportional to the squared mass of the particle, therefore it is stronger for lighter particles, such as electrons.

The ionization energy loss of MIPs is statistically distributed around its mean value, but due to δ -electrons it becomes asymmetric with a tail extended towards larger energy losses. The Landau distribution [63] or a convolution [64] of a Landau and a Gaussian distributions are used as the simplest approach to describe amplitude spectra obtained from measurements.

The energy needed to create an electron-hole pair in diamond is about 13 eV. The number of electron-hole pairs created per μm of material is obtained from

simulation and is about $36 \text{ eh}/\mu\text{m}$ for MIPs. A comparison of the relevant material properties for diamond and sapphire sensors is shown in Table 5.1.

3.3 Sensor characterization

Single crystal CVD diamond sensors were chosen for the BCM1F detector, as they match the requirements for a harsh radiation environment as close to the beam pipe:

- small size, which is important due to the limited space near the beam pipe;
- fast response, allowing for sub-nanosecond time resolution;
- radiation hardness;
- require no cooling for operation.

Sixty-eight diamond sensors of $5 \times 5 \text{ mm}^2$ area and 0.5 mm thickness were tested in DESY-Zeuthen's laboratory to choose 24 for the final installation. Sensor surfaces were metallized with two pads of half the area. The metal layer was made of a titanium-tungsten alloy or subsequent titanium and chromium layers. Before metallization, inspection with an optical microscope was done to exclude the presence of possible defects and to do a precise thickness measurement. After metallization a second inspection to check the metallization quality and to measure the pad size and the gap between pads was done.

Three criteria were used for the selection of sensors for installation: the sensor leakage current was required to be in the pA range up to 1 kV , the Charge Collection Efficiency (CCE) had to be close to 100% at about 100 V and the signal current, induced by a 37 MBq activity ^{90}Sr source, had to be stable over time.

The CCE is defined as the ratio of the collected and induced charge. It is a value between zero and one, and can be expressed as a percentage with maximum CCE corresponding to 100%. Examples of the characterization plots are shown and measurement setups are described in Ref. [65, 66].

3.4 Front-end electronics

A dedicated front-end ASIC has been developed in a 130 nm CMOS technology [67], expected to be intrinsically radiation hard. The design goals were linearity up to 10 fC input signal, a gain of 50 mV/fC , an equivalent noise of less than 1000 electrons at 10 pF input capacitance, a quasi-Gaussian pulse shape with a full-width at half maximum of less than 10 ns and a short recovery time for input signals above the linear range. The required parameters were verified in measurements in a test beam [68] and confirmed during LHC operation with circulating beams [69].

3.5 Signal transmission and back-end electronics

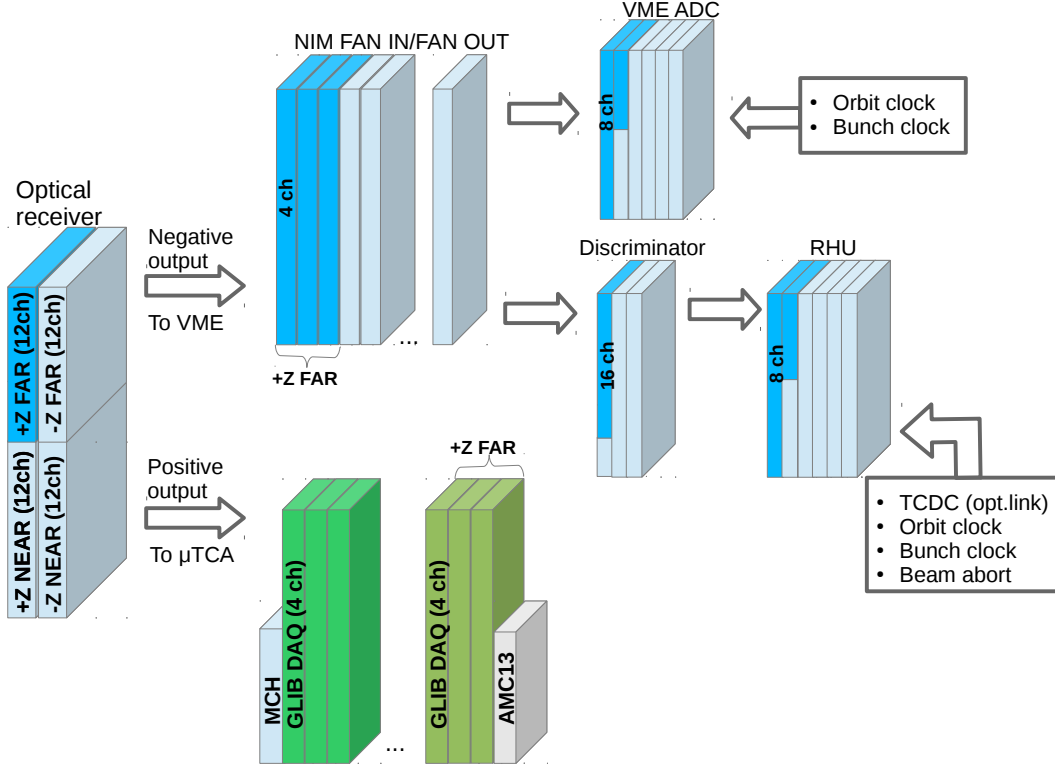


Figure 3.3: Schematic view of the BCM1F back-end. For illustration the readout chain of the +Z FAR C-shape is shown in a different color.

Signals from the ASICs from 12 BCM1F channels of one C-shape are distributed using a flexible PCB to four analog-opto-hybrids (AOH) with 3-channels each. A digital-opto-hybrid (DOH) is used to control the AOHs [70]. It is mounted on the solid part of the PCB. Each AOH channel is equipped with a laser diode with both adjustable bias current and gain. The maximum laser gain was used for operation. To find the setting of the bias current a scan was performed for each channel. The bias current was set to zero and then increased in small steps, thus showing the turn-on point of the laser. The operational bias current was chosen just above the turn-on point to ensure the full dynamic range. The flexible PCB is also seen on the top left in Figure 3.1. A Slow Hub Controller, implemented in the MicroTCA back-end electronics [71], produces the configuration commands. The DOH converts the steering signals to electrical ones, decodes them and provides the setting information to each laser driver of all AOHs.

Optical signals are transmitted via a 12-channel ribbon fiber cable to the counting room and fed into optical receivers (CMS Opto Bahn receivers of 100 MHz bandwidth). Four optical receiver boards with 12 channels each are needed to convert optical signals from all BCM1F channels into electrical ones, one optical receiver per C-shape. A schematic view of the BCM1F back-end electronics is shown in Figure 3.3. The +Z FAR C-shape modules are highlighted to track the whole electronics chain. The signal from each channel is duplicated in the optical receiver. The negative copy is used to provide signals to the VME based back-end electronics and the positive copy is fed into MicroTCA based ADCs.

One part of the VME back-end consists of fixed-threshold fast discriminators and deadtime-free Real-time Histogramming Units (RHUs). The raw RHU rates are processed to determine the online luminosity and MIB measurements for CMS and the LHC. The second part of the VME back-end consists of daisy-chained analog-to-digital converters (ADCs) which are read out. The ADC data is used to monitor the performance of the system. Since with the currently-used VME system data for only a limited amount of orbits can be recorded, a MicroTCA back-end is in development and will replace the VME back-end ADCs in the future.

3.5.1 Analogue signal processing using VME ADC

To serve 48 channels of the BCM1F detector, 6 CAEN digitizers V1721 with 8 channels per board are used [72]. The 8 bit ADCs are operated at a 500 MS/s sampling rate, reaching 2 ns sampling time. The modules are equipped with a front panel clock input and a phase-locked loop (PLL) for clock synthesis from internal/external references. For our purpose synchronization with the LHC clock was required. The ADCs were customized by CAEN to be able to lock on the 40.08 MHz LHC clock. The LHC clock was provided by the general LHC timing system and converted into ECL format.

All boards were updated to firmware revision v 4.3 (10. Sep. 2014) in the test facility before they were installed in the electronics cavern.

The ADCs are read out via optical links. The schematic of the daisy chain and a picture of the boards connected are shown in Figure 3.4. The successful connection of the boards in the daisy chain is identified by the LED next to the optical transceiver. Readout of the modules was triggered with the orbit clock signal. Six copies of the trigger signal are obtained from a Test Pulse Generator based on CAEN V1495 module [73] and provided to the ADCs.

The ADC data acquisition (DAQ) used in DESY-Zeuthen's laboratory [65] was upgraded to save data from daisy-chained ADCs. A set of resets was added at the beginning of the data acquisition to ensure smooth start of data saving. Also a block of the acquisition interruption was implemented to stop the DAQ code correctly if the stop signal arrived during the readout.

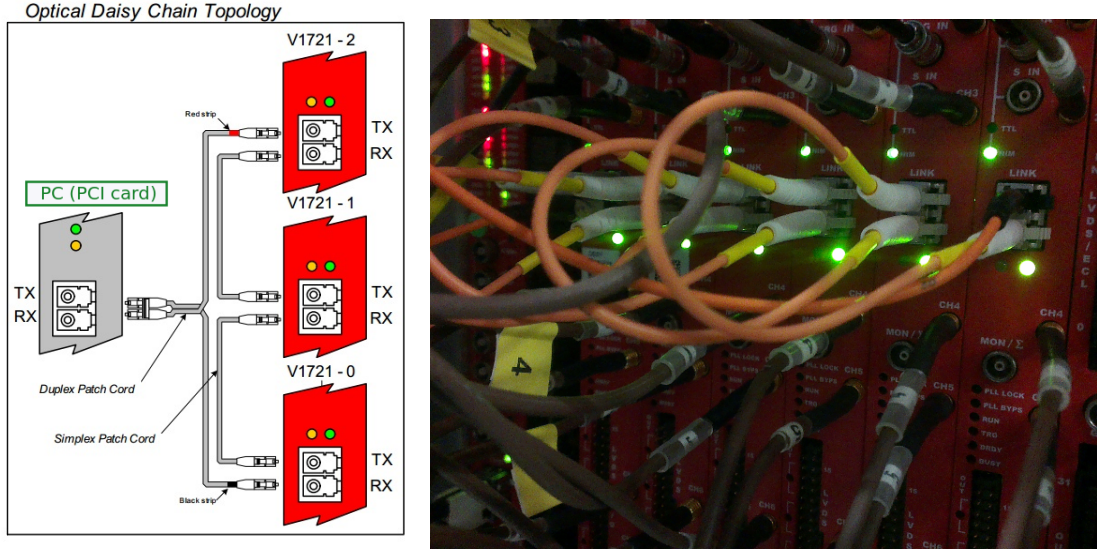


Figure 3.4: Schematic of the daisy-chained readout of the V1721 CAEN digitizers (left) and picture of the setup assembled in the VME crate in the CMS counting room (right).

Several settings have to be defined by the user. The length of the event to be readout from the ADCs buffer is defined by the variable `CUSTOM SIZE`. It was chosen to be 5563 units, because multiplied by 8 *bits* and 2 *ns* sampling time, it corresponds to one LHC orbit length of 89 μ s. Each time after a trigger is received and the board is ready for acquisition, one orbit is saved. As soon as the communication with the computer is established, the orbit is read out. Raw data is stored in ROOT format. The file size limit is set to 2 GB, reached by the DAQ after 5 *min* of data taking. About 4200 orbits per channel are saved in one raw ROOT file. With these constraints only one out of the 1000 LHC orbits is saved.

The ADC data is needed to study signals from individual particles, to monitor the detector response versus time, study the baseline stability and the effect of radiation damage. The recorded fraction of the orbits is sufficient for those studies.

3.5.2 Processing of the data using the Real-time Histogramming Unit

For online rates monitoring all signals have to be registered. For this purpose, deadtime-free RHUs are used [74]. An RHU is a VME board for sampling and processing discriminated signals from detectors in real time and sending data via the network. The RHU incorporates a FPGA with 5 *MBit* internal memory, 16 *MBit*

external memory and a Single Board Computer (SBC).

The signals from the 48 channels of BCM1F are fed into fixed threshold discriminators with 5 ns double pulse resolution. The discriminator threshold was determined from a threshold scan. For each channel, the threshold was set to a value just above the noise. This value is generally well below the minimum signal size of a charged particle. The output pulses are sent to 6 RHU modules with 8 channels per module. The RHU maps the hits synchronous to the LHC bunch clock in histograms with a bin width of 6.25 ns in a time window corresponding to an LHC orbit of 89 μ s. The histograms obtained for 4096 orbits are read out via the Linux-based SBC and transferred via the network to the Luminosity DAQ. This data forms a luminosity nibble. The sum of the histograms from four nibbles (~ 1.46 s) is used for luminosity and MIB measurements.

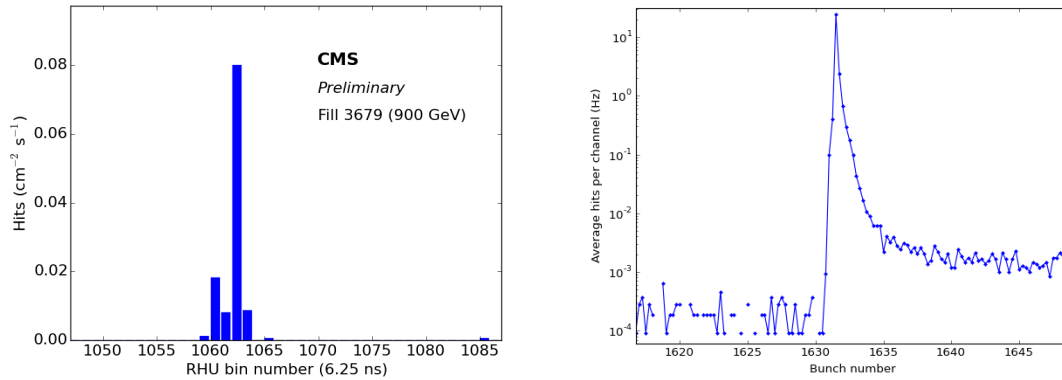


Figure 3.5: Count rates in 4 bins around a bunch crossing as recorded by the RHU [75]. Left: Data from Fill 3679 at $\sqrt{s} = 900$ GeV, at the beginning of the LHC Run II. Right: Data from the VdM scan Fill 4266, at $\sqrt{s} = 13$ TeV.

For the LHC bunch spacing of 25 ns 4 bins in the RHU histogram are available per bunch crossing. Because of the distance along the z -axis between the sensors and the interaction point, MIB particles being in time with the incoming bunch (Figure 3.2) are counted in the first bin. Outgoing MIB particles and particles originating from collisions populate the third bin, as can be seen in the Figure 3.5. The left figure is obtained from data at $\sqrt{s} = 900$ GeV, Fill 3679, at the beginning of the LHC Run II. Histograms from a data taking time of about 2.5 minutes were added. In the right figure, data is used from the VdM scan Fill 4266 at $\sqrt{s} = 13$ TeV of the first bunch of the third bunch train, integrated over 2 hours. The first bin with a counting rate of about 10^{-1} Hz corresponds to incoming MIB, the third bin with a counting rate of about 20 Hz corresponds to collision products plus outgoing

MIB. In addition, the “albedo” tail is visible after the collision, originating from hits of delayed particles.

3.5.3 The MicroTCA based back-end electronics

The MicroTCA technology allows advanced signal processing that is implemented in a FPGA. It is chosen for the phase one upgrade, currently still in development. The deadtime-free operation makes it convenient for high luminosity operation and allows the resolution of even double hits within a few ns .

The system control and communication is being operated by the specialized CMS MicroTCA Hub module AMC13 and the NAT MicroTCA Hub module (MCH) [71]. Four-channel GLIB DAQ modules are used for data processing, 3 modules per C-shape as shown for +Z FAR in Figure 3.3. The modules are synchronized using the LHC clock. The functionality of the MicroTCA ADC will combine functionality of the VME ADC and the RHU. During the commissioning period the MicroTCA ADC will be complementary to RHU. Counting rates, the time distribution of the hits in the LHC orbit and amplitude histograms will be provided. The produced histograms will be stored in the internal memory and transmitted to the MCH through the back-plane and subsequently to the BRIL DAQ for online luminosity measurements and system performance monitoring.

3.6 Beam splashes and BCM1F timing adjustment

A splash event is generated by a single bunch at an injection energy of 450 GeV which is dumped in a collimator just upstream of the ATLAS or CMS experiment. Splashes are performed by the LHC in series for each experiment using both beams.

Splash events were important to test the functionality of all detectors before the LHC starts operation. Especially in April 2015 splashes played an important role, as it was a first chance after the installation for the BRIL team to check the responses of all channels. The arrival time information was very useful to correct time settings in the counting room. The correction of the arrival time difference between the BCM1F signals from +Z and -Z ends and BTPX is described in Appendix A.

Splashes in April 2016 were used mostly to compare the response of the channels to the one of the previous year. Also it was important to confirm the functionality of the channels used for luminosity and MIB measurements in 2016 after the technical stop.

3.6.1 ADC data analysis from splashes

All beam splash events were recorded with the VME ADCs. The BPTX “beam 1 OR beam 2 signal” was used to trigger the ADC readout. As a splash event generates large signals in the sensors a saturation of the optical readout chain was observed as shown in Figure 3.6. For illustration of the good agreement between different channels 12 channels from C-shape +Z FAR are shown on the left and 12 channels from C-shape -Z NEAR are shown on the right. A detailed amplitude analysis of the recorded signals was not possible because of the saturation, but the functionality of the channels was confirmed and the detector response seen for an amount of crossing particles several orders of magnitude higher than the system was designed for.

As the standard detector response to one MIP, a pulse with an amplitude of about 40 mV and a time over threshold about 20 ns was taken at the outputs of the optical receivers. Assuming that also for saturated signals both the amplitude and the time over the threshold is a measure of the original amplitude, the splash signal was converted into a MIP equivalent.

The duration of the saturation pulses shown in Figure 3.6 points to less intense splash events from beam 1 (left), then from beam 2 (right). The saturation pulses from beam 1 splashes have an amplitude of about 360 mV and a time over threshold of about 40 ns . It corresponds to a minimum of about 18 $MIPs$ crossing the diamond pad simultaneously, taking the integral over time as a measurement for the number of particles. As the diamond pad metallization area is $[0.24 \times 0.48] \text{ cm}^2$ the estimated number of MIPs per cm^2 is about 180 MIP/cm^2 . The saturation pulses from beam 2 splashes have an amplitude of about 360 mV and time over threshold of about 80 ns . The integral over time corresponds to a minimum 360 MIP/cm^2 .

In Figure 3.6 (left) it is also possible to see a delayed hit with arrival time at 1190 ns , gray curve. This signal is most likely originating from material activation or from a cosmic particle. There were much more examples of such delayed events with different delay times and amplitudes after the splash event.

In April 2016 the LHC machine delivered for CMS 7 splashes with one collimator closed as well as 10 splashes with two collimators closed from beam 1 and 15 splashes with two collimators closed from beam 2. As the response of the BCM1F active channels to splash events with both collimators closed for beam 1 and beam 2 were similar, we will discuss only splashes from beam 1.

The RHU counting rates, displayed on one of the online monitors in the CMS control room are shown in Figure 3.7. Splash events with one collimator closed are much more intense, compared with events with both collimators closed. Two of the most intense splash events triggered the BCML2 beam abort signal.

The ADC data shown in Figure 3.8 (left) in pink and light blue (channels 40-41), show an amplitude of about 400 mV and time over threshold of about 80 ns and correspond to more than 400 MIP/cm^2 . The green and dark blue curves (channels

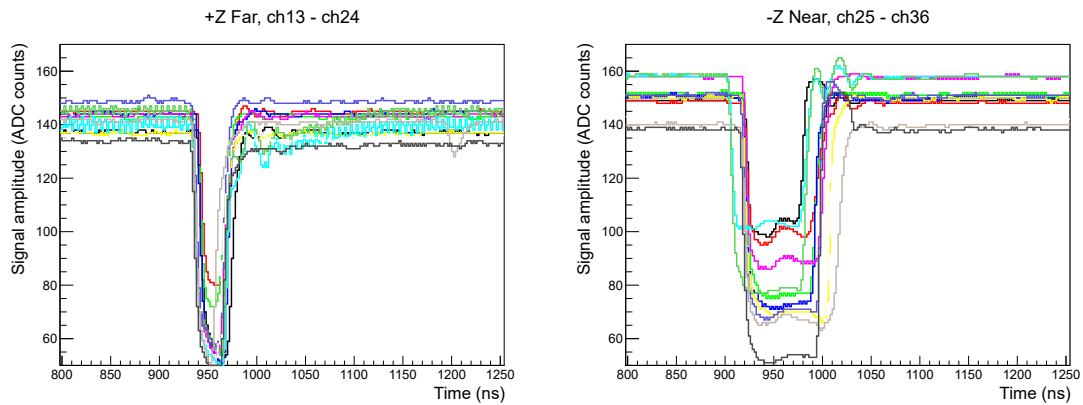


Figure 3.6: Response of several channels of the BCM1F detector to beam 1 (left) and beam 2 (right) splash events recorded by the VME ADCs in April 2015. The signal amplitude is shown as a function of time. One ADC count corresponds to 4 mV .

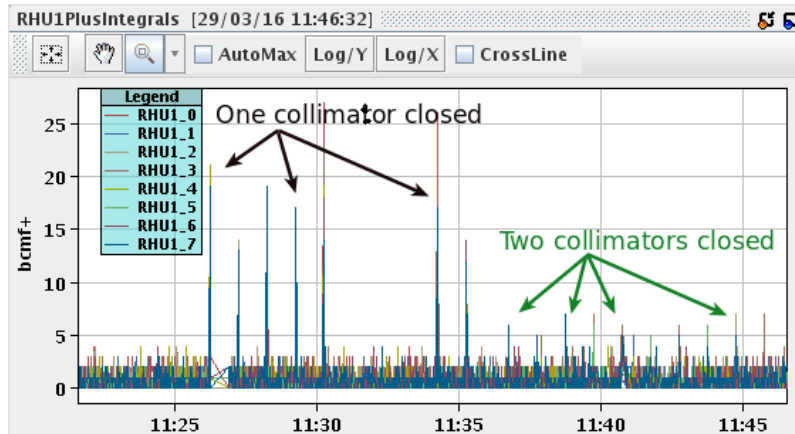


Figure 3.7: Screen-shot of the RHU counting rates displayed in the CMS control room. 7 intense splash events from beam 1 with one collimators closed are shown on the left. Much smaller intensity splash events with two collimators closed are shown on the right.

44-45) had a signal high enough for ASIC saturation. The duration of the saturation pulse is more than 500 ns.

The saturation pulses of beam 1 with both collimators closed are shown in Figure 3.8 (right). Its amplitude is about 400 mV and the time over threshold about 75 ns. The pulse integral corresponds to a minimum of 375 MIP/cm².

Secondary peaks after the saturation pulse correspond to delayed particles from activated material. They are observed with a delay of up to a few μ s and have different amplitudes. The more intense the pulse from the splash event was, the more activation products are observed.

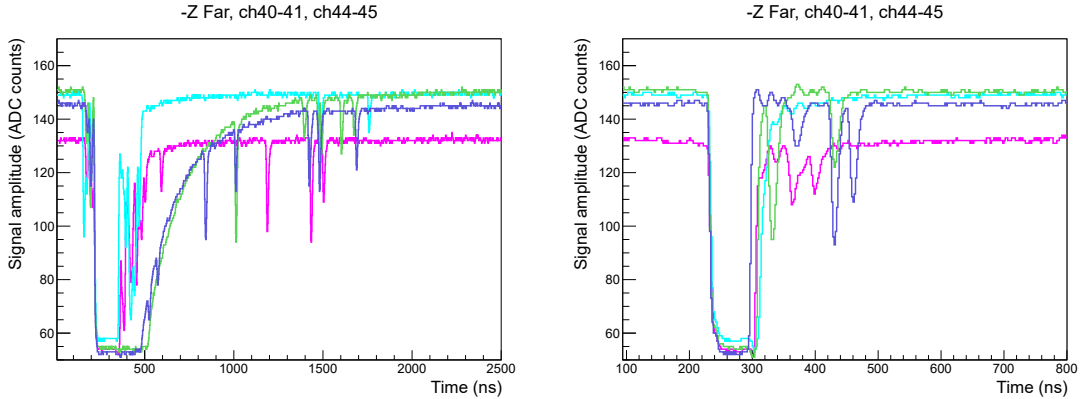


Figure 3.8: Response of 4 reference channels of the BCM1F detector to 2016 splash events: ch 40 in pink, ch 41 in light blue, ch 44 in green, ch 45 in dark blue. Beam 1 splashes with one collimator closed (left) and with two collimators closed (right).

3.7 The BCM1F response studies using the VME ADC

The response of the detector and electronics is changing during the operation because of radiation damage and possibly because of CMS changes to the magnetic field or temperature. The ADC data analysis is focused on detector stability and response monitoring. Individual signals from particle hits are processed to obtain amplitude spectra and to study the development of these spectra as a function of time. The stability of the electronics and response changes of the sensors are monitored separately, since a test pulse (TP) of a constant amplitude and fixed arrival time is fed into a special input of the ASIC.

An example of one recorded orbit during the LHC Fill 4364 with 877 colliding bunches grouped in bunch trains is shown in Figure 3.9 a). The filling scheme

contained one “pilot” bunch – separated from the rest of the bunches, one short bunch train containing 12 bunches and 12 longer bunch trains containing about 70 bunches. The longer bunch trains were in groups of two with 9 unfilled bunch positions in between.

Applying a 3 ADC counts threshold to each recorded orbit of ADC values, the distribution of the hits arrival time was obtained, as it is shown in Figure 3.9 b). The first ADC sample value under the thresholds is taken as the arrival time and saved as one histogram entry. The observed pattern reproduces the filling scheme of the LHC: a pilot bunch, a short bunch train, longer bunch trains in groups of two with a short gap in between.

3.7.1 Baseline position

The baseline of the ADC is determined from data samples in the abort gap, where no signals are expected. Data taken during 40 ns in the abort gap is averaged defining the baseline for each channel. The baseline position monitoring is important to characterise the stability of the readout chain. A typical baseline position histogram is shown in Figure 3.10 (left). The standard deviation of the baseline distribution is defined as:

$$BL_{sigma} = \sum_{n=1}^N \sqrt{(BL_{aver.} - BL_n)^2/N}, \quad (3.2)$$

where $BL_{aver.}$ is the averaged baseline value, BL_n the baseline value of one data sample and N a number of samples in the average. The obtained distribution is shown in Figure 3.10 (right).

3.7.2 Detector response for particle hits and test pulses

An example of one LHC orbit recorded by the VME ADC is shown in Figure 3.9 a). Zooming into the range of the first long bunch train with arrival time around 12600 ns, an example of the response of the BCM1F detector for a single particle hit is shown in Figure 3.11 on the left. The first hit corresponds to an amplitude of 24 mV and the second hit to an amplitude of about 220 mV. The rise-time of both signals is about 10 ns.

To find such signals in the ADC data, a threshold was set. It will be described in more detail in the following section. Thresholds of 1 and 3 ADC counts are shown in Figure 3.11 as the horizontal red dashed and solid lines, respectively.

Because of the irradiation a reduced performance of the detector is expected over time. The performance of the readout electronics chain is monitored using the test pulse. An example of a test pulse is shown in Figure 3.11 on the right. It is set to

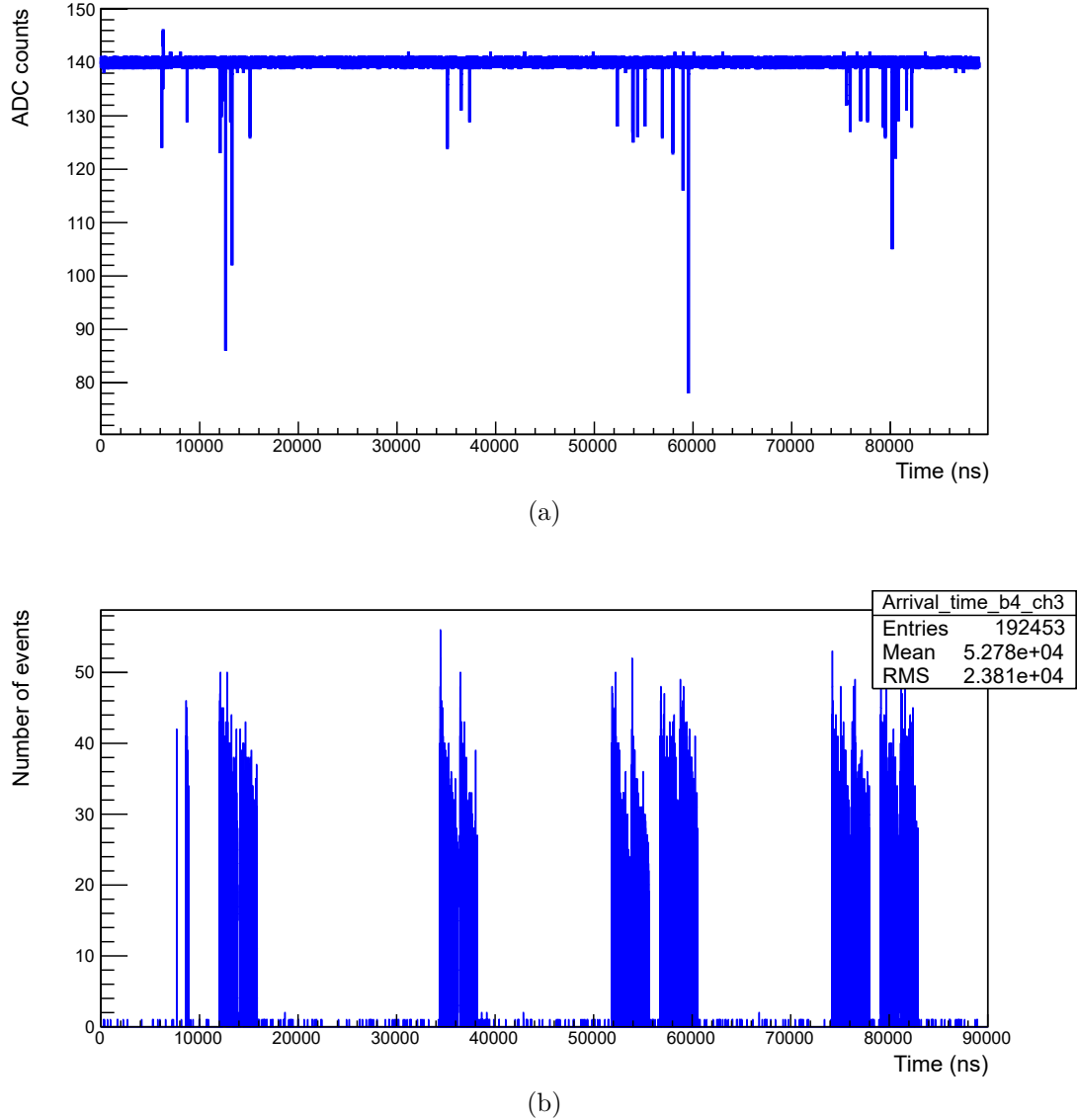


Figure 3.9: The VME ADC data recorded with 877 colliding bunches in the LHC, Fill 4364. a) Example of signals of one LHC orbit. b) Particles arrival time distribution. About 4200 orbits as shown in a) were processed applying a threshold of 3 ADC counts. The pattern reproduces the filling scheme of the LHC.

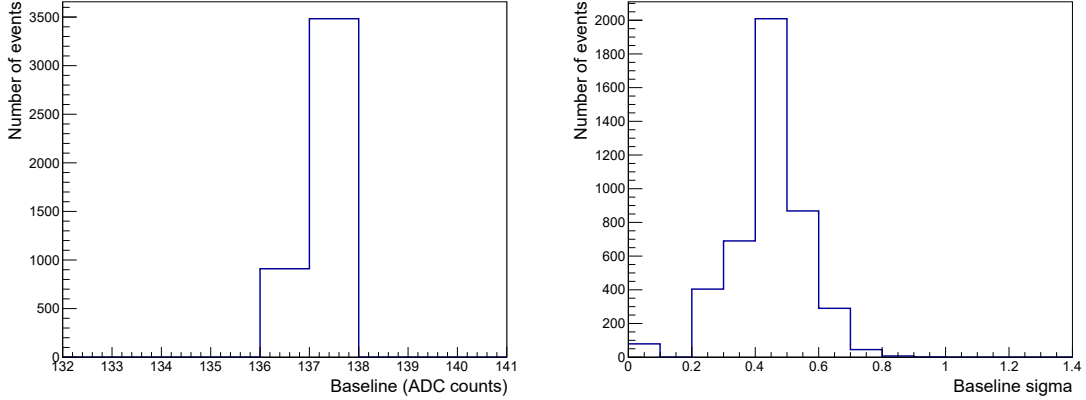


Figure 3.10: VME ADC data of channel 12 in Fill 3695. Left: Baseline position defined in the abort gap. Right: The distribution of the standard deviation of the baseline as defined in Eq. 3.2.

arrive with a fixed delay after the start of an orbit. The analysis is done applying the same thresholds as for hits, but only in the narrow time-window, surrounded by vertical dashed red lines in Figure 3.11, right. Part of the orbit corresponding to the arrival time of the test pulse is excluded from the particles amplitude spectra analysis.

3.7.3 Signal amplitude and signal length spectra

After the baseline for the particular orbit is defined, signals are found applying a certain threshold. A threshold of one ADC count is the minimum possible threshold based on the baseline standard deviation, as shown in the subsection 3.7.1. If the signal stays more than 6 ns below the threshold it is considered as a signal candidate and processed again from the first till the last bin under the thresholds to define the time over threshold and the amplitude. The amplitude is defined as the minimum value under the threshold.

Using data from a large amount of orbits histograms of the signal amplitude and length were obtained. An example of an amplitude spectrum histogram for channel 12 with 4 mV threshold, corresponding to one ADC count, is shown in Figure 3.12 on the left. The first peak in the spectrum corresponds to noise, also called “pedestal” peak. The second peak at about 55 mV corresponds to relativistic particle hits hereafter referred to as MIP peak.

The pedestal and MIP peak have to be well separated. This is reached by applying a bias voltage high enough to the diamond sensors to keep the CCE at

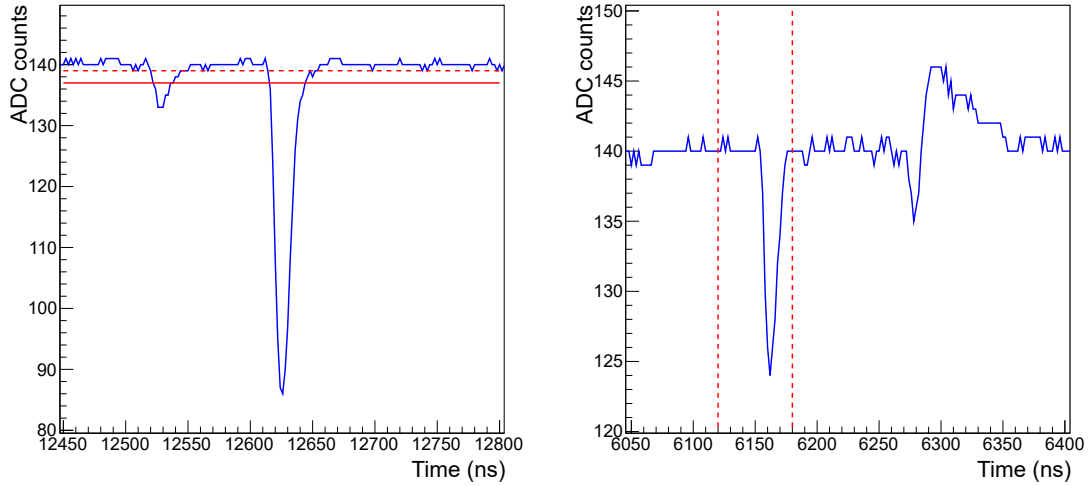


Figure 3.11: The VME ADC data. Left: An example of the detector response to a particle hit (blue) with a threshold applied in the analysis (dashed and solid red lines). Right: Test pulse signal (blue). The region selected for the later analysis is indicated by the red dashed lines. One ADC count corresponds to 4 mV .

100%. At the beginning of operation for most of the installed diamond sensors 100% CCE was already reached at 40-100 V .

Due to irradiation uniformly distributed traps are developing in the diamond material. These traps are filled by charge carriers traveling to the electrodes. As bias voltage of the fixed polarity is applied to the electrodes, and electrons are always moving to the positive electrode and holes to the negative electrode, traps are filled non-uniformly. More electrons are trapped next to the positive electrode, more holes next to the negative electrode, creating non-uniform space charge of opposite polarity. It is called polarization and described in more detail in Ref. [76, 77].

To reduce the polarization effect and to keep the CCE constant the bias voltage was set at the beginning of operation to above 200 V .

The deep minimum between the pedestal and the MIP peak is used to define the minimum threshold needed to cut noise. For all BCM1F channels a threshold of 12–16 mV is already enough to cut the noise. These thresholds defined from the spectra analysis are in a good agreement with the values defined from the discriminator thresholds scan. They were set individually for all channels.

For further studies a threshold of 12 mV , corresponding to 3 ADC counts, was used. An example of the amplitude spectrum is shown for channel 12 in Figure 3.12 on the right. The maximum of the distribution around 55 mV corresponds to the

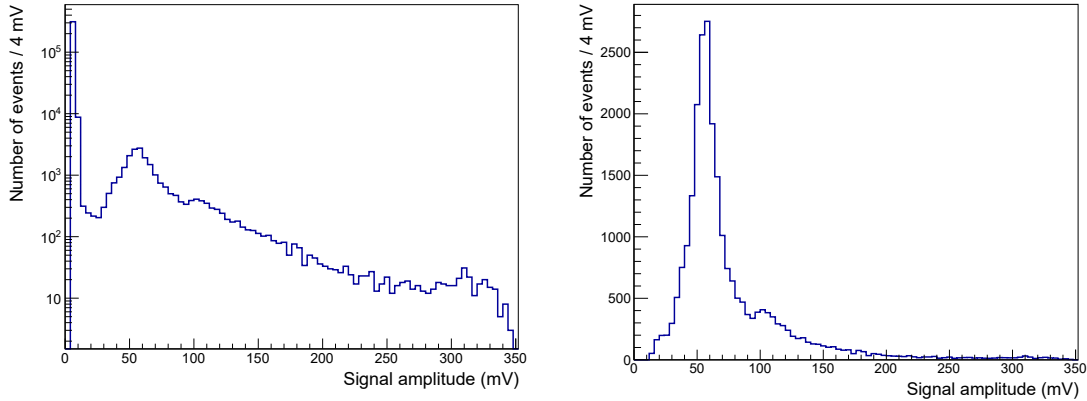


Figure 3.12: VME ADC data from channel 12, Fill 3965. Left: The signal amplitude spectrum built using a 4 mV threshold. The signal amplitude in mV with 4 mV binning is plotted on the x -axis, the number of particles of a given amplitude is on the y -axis. The peak around 55 mV is the 1 MIP and around 110 mV is the 2 MIP peak. Right: An example of a signal amplitude spectrum built using a 12 mV threshold.

detector response to one MIP. A second peak around 110 mV originates from two particles crossing simultaneously.

The time over threshold distribution is shown in Figure 3.13 on the left. The maximum of the distribution corresponds to about 24 ns , matching the requirement for the 25 ns bunch spacing operation mode of the LHC.

An example of an amplitude spectrum and signal length distribution obtained for test pulses are shown in Figure 3.13 in the middle and right plots. As expected, the distributions for test pulses are narrower than for particle hits, as they are always generated with the same test charge and only the superposition of electronics noise broadens the spectra. The average test pulse amplitude is about 70 mV and the time over the threshold is less than 20 ns .

3.8 Detector stability and radiation damage monitoring

For each data taking period the LHC ring is filled with proton bunches with the desired filling scheme [78]. One data taking period starts with the beam injection and ends with the beam dump, the whole referred to as a Fill. Fills are numerated with consecutive numbers.

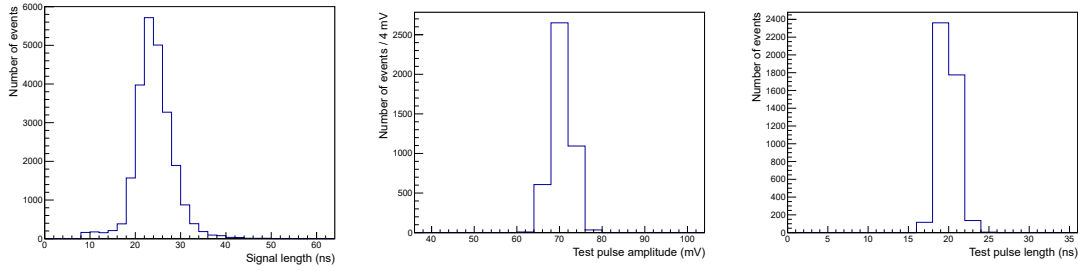


Figure 3.13: VME ADC data from channel 12, Fill 3965. Left: A time over the threshold distribution. Middle: An example of the test pulse amplitude spectra, a 12 mV threshold applied. Right: Time over the threshold distribution for the test pulse signals.

After LS1 the LHC started in March 2015 the commissioning period first without beam in the LHC ring, then with non-colliding single bunches and later operating with 50 ns bunch spacing, hereafter referred to as the 50 ns operation period. When the commissioning period was completed, the operation with 25 ns bunch spacing began, hereafter referred to as the 25 ns operation period.

During the LHC operation the RHU data is used for online monitoring of the rates. Stability of the rates within one LHC Fill is a rough indication for stable operation of the detector. However, to monitor the stability of the detector quantitatively over a longer period of time, the amplitude spectra obtained from VME ADC data is used.

3.8.1 BCM1F stability within long LHC fills and in the 50 ns operation period

The duration of LHC physics fills varies between a couple of hours and more than 24 hours. Fill 5045 in June 2016 was one of the longest in the LHC history. Its duration reached 37 hours.

To study the stability of the MIP peak position within the fill, an average fill of about 12 hours duration was chosen, Fill 4246. The beam intensity as a function of time measured by LHC is shown in Figure 3.14. There were 328 colliding bunches in the machine, the CMS magnet was at a field strength of 3.8 T and the energy per beam 6.5 TeV . Three ADC data sets marked with the arrows in Figure 3.14 were chosen for comparison of the MIP peak position: at the beginning of the fill (around 00:00), in the middle (around 03:00) and at the end of the fill (around 08:00).

Data files were analyzed applying a 12 mV threshold to build the amplitude spectra similar to the one shown in Figure 3.12 on the right. Most of the particles

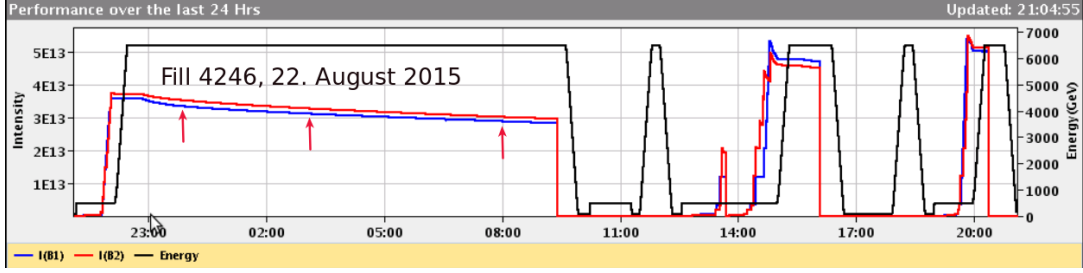


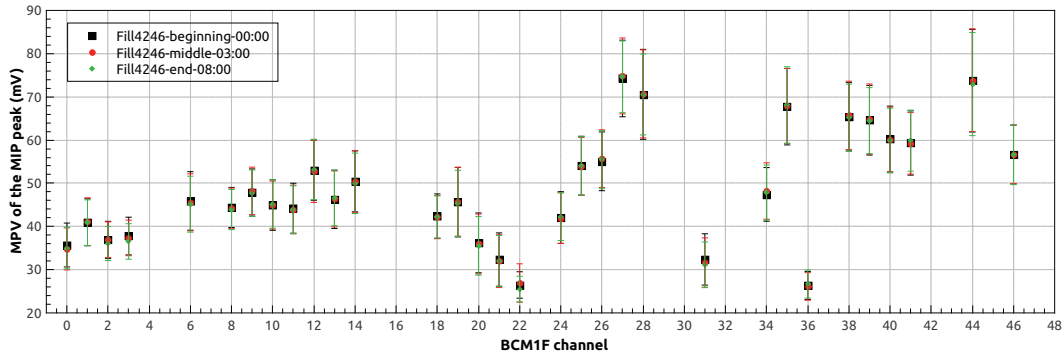
Figure 3.14: Online LHC measurement of the beam intensities versus time during last 24 hours starting from about 22:00 on August 21st 2015. Blue is the intensity of beam 1, red the intensity of beam 2 and in black the energy per beam.

crossing the sensors are relativistic, hence their energy deposition follows a distribution close to a Landau distribution, as it was described in subsection 3.2. Therefore the Landau distribution was used to fit the MIP peak range of the amplitude spectra and define the most probable value (MPV). The MPV values obtained from the fit were used to monitor the stability of the MIP peak position within the fill.

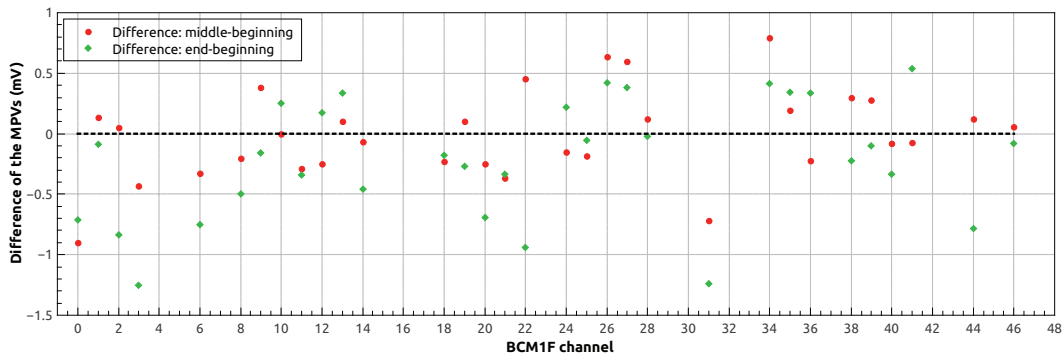
The extracted MPV values for each of three data sets are shown in Figure 3.15 a). It is seen that the obtained values are almost the same. The error bars correspond to the FWHM of the Landau distribution. For better illustration the difference of the MPV in the middle and at the beginning of the fill as well as the difference at the end and at the beginning of the fill are shown in red and green colors, respectively, in Figure 3.15 b). Some channels are not shown, as there was no data available. Those channels were used for other measurements or high voltage setting were too low to see the MIP peak. The maximum difference is for most of the channels less than or equal to 1 mV . Also the test pulse position was found to be stable within the fill. Hence we conclude stability of the MPV position within a data taking fill.

In the following the MPV position is considered over a longer period, the whole 50 ns operation period, when radiation damage may cause a decrease of the CCE. For several data sets recorded between July 6 and August 22 the MPV of the fit with a Landau distribution was determined. The value obtained from the data taken at July 6 is used as a reference. The values of the MPV for all channels at the beginning and at the end of the 50 ns operation period are shown in Figure 3.16 a). In Figure 3.16 b) the relative change of the MPV for the same data sets is shown, where 1 corresponds to 100%.

The channels used in the luminosity measurement are indicated by blue dots. Channels shown as red dots were not used because of erratic signals or changed high voltages due to trips. For six channels only the July measurement is shown, as later data is not available.



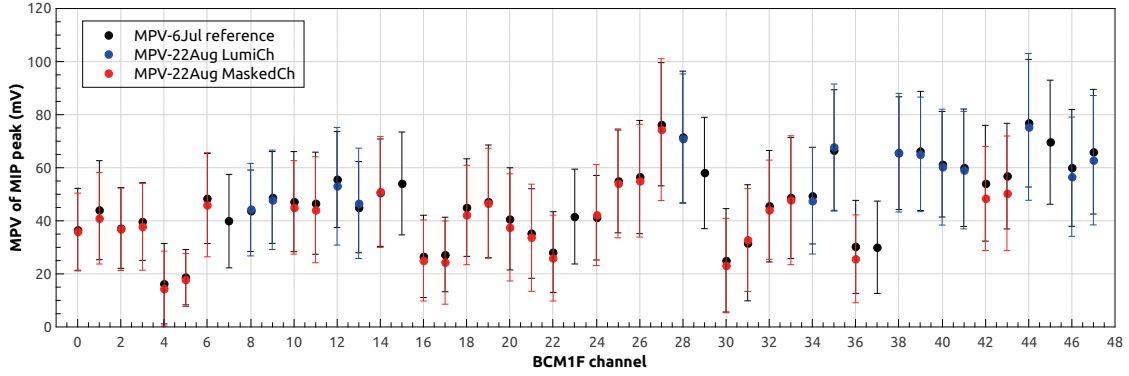
(a)



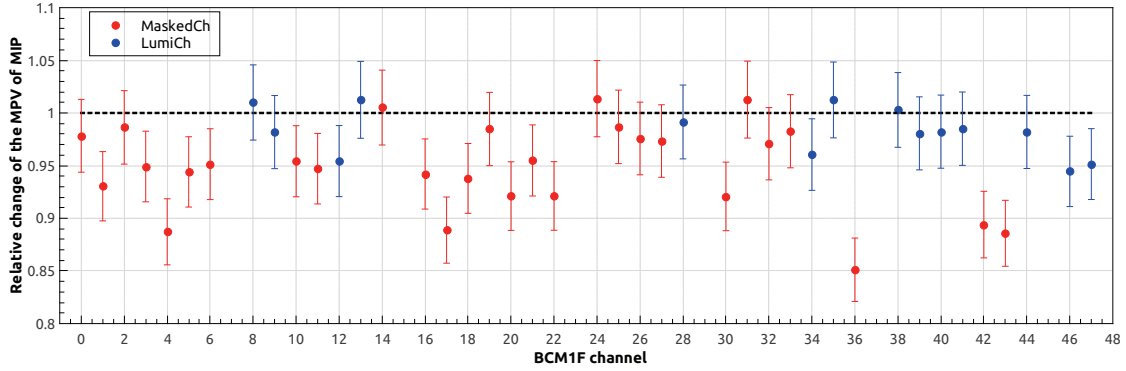
(b)

Figure 3.15: Comparison of the MPV position within the long LHC Fill 4246. a) Position of the MPV in mV at the beginning, middle and end of the Fill 4246. b) Difference of the MPV in the middle and at the beginning of the fill (red); at the end and at the beginning of the fill (green).

Chapter 3. BCM1F detector as luminometer



(a)



(b)

Figure 3.16: a) The MPV for all channels at July 6, corresponding to an integrated luminosity of 12 pb^{-1} (in black) and at August 22, corresponding to an integrated luminosity of 191 pb^{-1} (masked channels in red and channels used for the luminosity measurement in blue). b) The relative change of the MPV between July 6 and August 22 (masked channels in red and channels used for the luminosity measurement in blue).

The position of the MPV for channels used in the luminosity measurement varies between 40 mV and 80 mV, mainly due to the variations of the overall gain in the optical signal transfer units. In Figure 3.16 b) a slight decrease of the MPV value on the 22nd of August is observed. Figure 3.16 b) illustrates the relative change of the MPV position. For channels included in the luminosity measurement the relative drop reached up to 6% in a few channels. This drop is attributed to radiation damage.

To separate radiation damage of the sensors from the radiation damage of the electronics test pulse spectra were used. The test pulse distribution is narrow and Gaussian-like, as shown in Figure 3.13. Any movement of the peak in the test pulse amplitude distribution with time reflects changes in the electronics chain and is taken into account when determining efficiency loss of the sensors. The mean values of the test pulse spectra are shown in Figure 3.17 a) for the same data sets and keeping the color code as for the MPV plots. The variations between the channels correspond, as expected, to the variations for the MPV values in Figure 3.16 a). From the relative changes of the TP amplitude, shown in Figure 3.17 b) the maximum drop of the TP amplitude for channels used in the luminosity measurement reached about 4 %.

An important conclusion of this study is that the shift of the MPV towards lower values during 50 ns operation did not affect the luminosity measurements. The MPV in all luminosity channels was well above the threshold.

3.8.2 BCM1F performance as a function of the luminosity

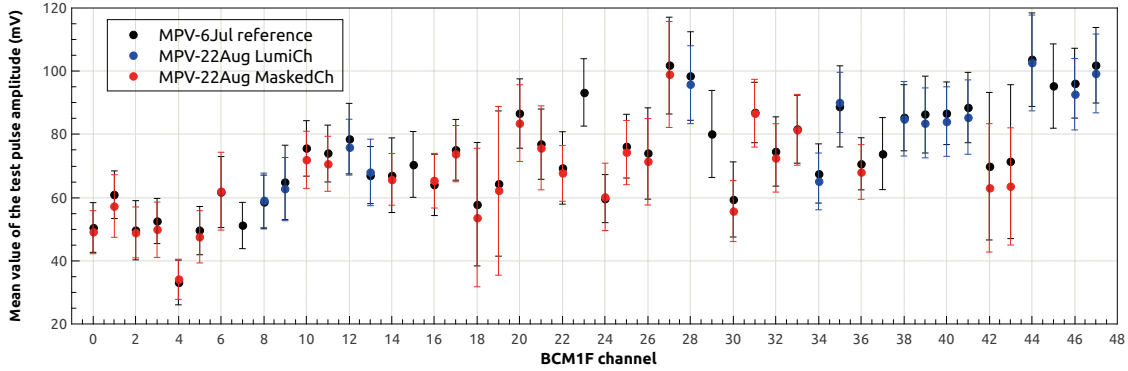
As a reference for the amplitude spectrum, Fill 3965 from the beginning of the operation in July 2015 is taken. An example is shown in Figure 3.18 for channel 12 in red. The integrated luminosity at this time was 12 pb^{-1} with a particle flux of about $4 \cdot 10^6 \text{ MIP/cm}^2\text{s}$. After three months of operation the sensors show a 13% shift of the MPV to lower values. A comparison of the reference spectrum from the July data to spectra from September (Fill 4437, blue dashed line) and October data (Fill 4467, black line) is shown in Figure 3.18.

As the LHC was in the commissioning period, later fills had more colliding bunches and accumulated luminosity. After Fill 4437, where the integrated luminosity was 1257 pb^{-1} and the particle flux was about $23 \cdot 10^6 \text{ MIP/cm}^2\text{s}$ the MIP peak became wider but the MPV stayed at the same position. After the Fill 4467 integrated luminosity was almost doubled and reached 2107 pb^{-1} . The particle flux reached about $27 \cdot 10^6 \text{ MIP/cm}^2\text{s}$ in Fill 4467. The left side of the spectra, which corresponds to smaller amplitudes, appears and forms a shoulder. This is caused by an increased amount of traps in the sensor due to irradiation and also by a lower electric field on the sensor edges and in the metallization gap, as it will be shown later.

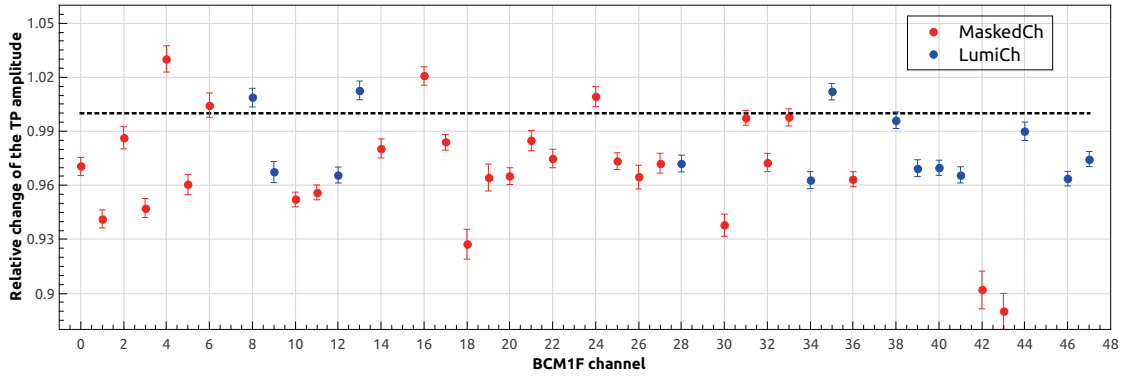
Starting from the 25 ns operation period and dense filling of the LHC, the luminosity and, together with it, hit rates, and hence, radiation damage of the sensors significantly increased. It caused more problems with erratic behavior of the sensors and the bias voltage had to be lowered in more channels. As the bias voltage was lowered, the calibration of the sensors was no longer valid and they could not be used for luminosity measurements.

Four channels, which showed stable and reliable behavior were kept up to November at the initial voltage settings of 225 V. They were used for online luminosity

Chapter 3. BCM1F detector as luminometer



(a)



(b)

Figure 3.17: a) The mean value of the Gaussian fit to the TP amplitude distribution at July 6 (in black) and at August 22 (masked channels in red and channels used for the luminosity measurement in blue). b) The relative change of the mean value of the TP in percent between July 6 (in black) and at August 22 (masked channels in red and channels used for the luminosity measurement in blue).

and machine induced background measurements. The relative change of the MPV from the beginning of operation up to November 2015 is shown in Figure 3.19 as a function of the integrated luminosity. Channels 40-41 are shown in red color and channels 44-45 in pink. Some data points are missing for channel 45, as it was used for other measurements and amplitude spectra could not be built. Even though all luminosity channels are located at the same C-shape it is seen that in channel 44-45 the shift of the MPV is much larger and reaches about 16%, whereas for channel 40-41 it is less than 8%. This points to a strong performance difference from sensor

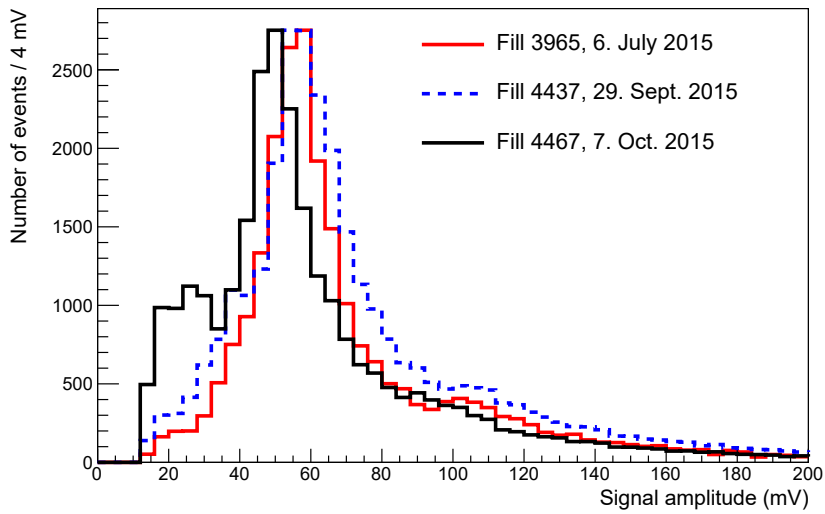


Figure 3.18: The amplitude spectra for channel 12 at a bias voltage of 200 V at the beginning and after several months of operation in a high radiation field. The red line from reference Fill 3965, beginning of the operation, after an integrated luminosity 12 pb^{-1} ; blue dashed line from Fill 4437, after an integrated luminosity 1257 pb^{-1} ; black line from Fill 4467, after an integrated luminosity 2107 pb^{-1} . Histograms are normalized using the peak values.

to sensor.

To estimate the influence of the electronics chain on the observed MPV drop, test pulse amplitude spectra were analyzed for the same data sets. The relative change of the test pulse position is shown as well in Figure 3.19 in blue for channels 40-41 and in turquoise for channels 44-45. The relative drop of the test pulse amplitude is almost equal for all channels and reached not more than 6% in November 2015.

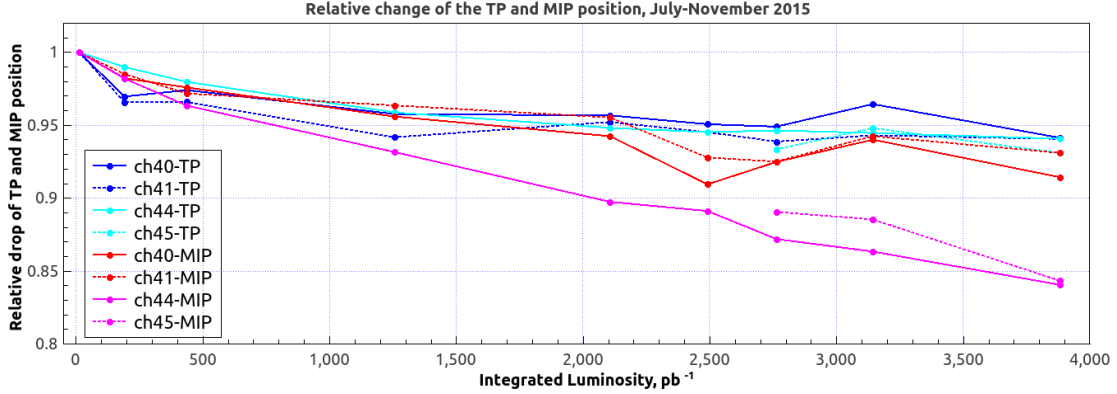


Figure 3.19: The relative drop of the MPV and TP position for luminosity channels 40-41 and 44-45.

Later in the year 2015 the channels 44-45 also showed instabilities and the voltage was lowered first by 25 V and then by 50 V and 100 V. Figure 3.20 shows the amplitude spectra for channel 40 and channel 44 in July 2015 as reference in red in both plots and at different voltages and times in 2015 - 2016. The partner channels 41 and 45 showed a similar behavior, thus we will concentrate only on channels 40 and 44.

The amplitude spectra of channel 40 shown on the left side in Figure 3.20 illustrate the stability of the MIP peak position. As it was mentioned before, the drop of the MPV was about 8% in November 2015 and did not reach more than 10% in May 2016. Concerning channel 44, the HV supply tripped a few times and was finally operated at 150 V in May 2016. The difference of the amplitude spectra is shown on the right side in Figure 3.20. With respect to the reference position, the MPV drop reached about 18% in April 2016 when it was at 225 V (blue curve) and already 35% in May when the bias voltage was lowered to 150 V (black curve).

For a van der Meer scan in 2016 the voltage settings were lowered to 175 V for channels 40-41 and to 125 V for channels 44-45 to ensure stable performance. The separation of the MIP peak from the pedestal was still kept.

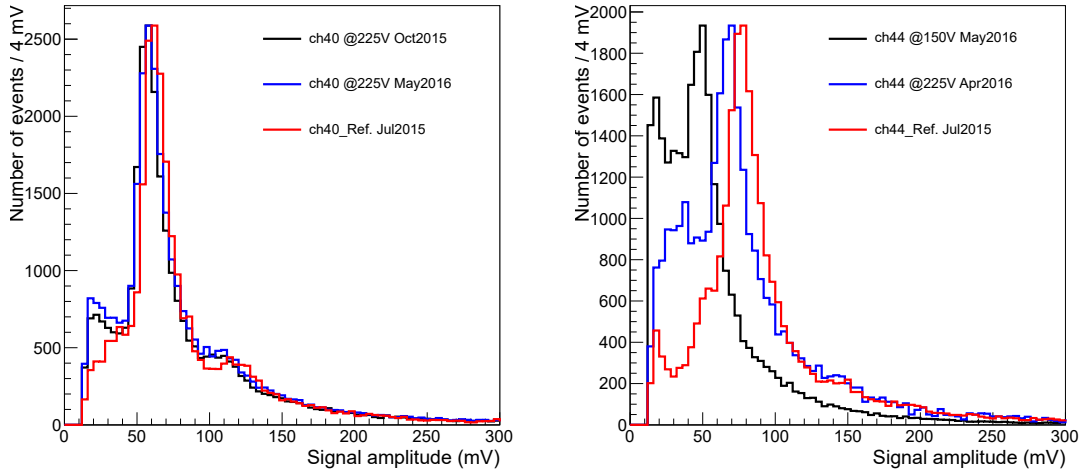


Figure 3.20: Left: amplitude spectra for channel 40 in 2015-2016. The reference spectrum at the beginning of the operation in July 2015 is shown in red, the intermediate spectrum for October 2015 data is in black and the latest spectrum for May 2016 data in blue. Right: amplitude spectra for channel 44. The reference spectrum is shown in red, the spectrum at the same bias voltage in April 2016 is shown in blue and the latest spectrum for May 2016 data at a bias voltage lowered to 150 V is in black.

Impact of radiation damage on signal length

Three data sets were used to study the signal length as a function of the integrated luminosity. The comparison is shown in Figure 3.21 left. The red line corresponds to the reference Fill 3965, the blue dashed line to Fill 4437 and the black line to Fill 4437. Histograms are normalized by the peak values.

The filling scheme of the LHC was different. The number of colliding bunches was 111, 1291 and 1596 in Fills 3965, 4437 and 4467, corresponding to flux of about $4 \cdot 10^6 \text{ MIP/cm}^2\text{s}$, $23 \cdot 10^6 \text{ MIP/cm}^2\text{s}$ and $27 \cdot 10^6 \text{ MIP/cm}^2\text{s}$, respectively. The probability that the hits from consecutive bunches pile up depends on the number of bunches, therefore peaks corresponding to two and three particles are visible in distributions from Fill 4437 and Fill 4467.

An example of a double hit is shown in Figure 3.21 on the right. It is obtained from Fill 4467. The measured time over threshold for the double hit is about 50 ns. Also a couple of single hits are seen beforehand.

From the evolution of the time over threshold distribution it is seen that it becomes broader and the amount of longer signals increases with increasing luminosity.

Also the peak corresponding to one particle hit is moving towards longer signals. This may be caused by the slower charge collection in the sensor due to polarization and longer signals because of the pile up of signals.

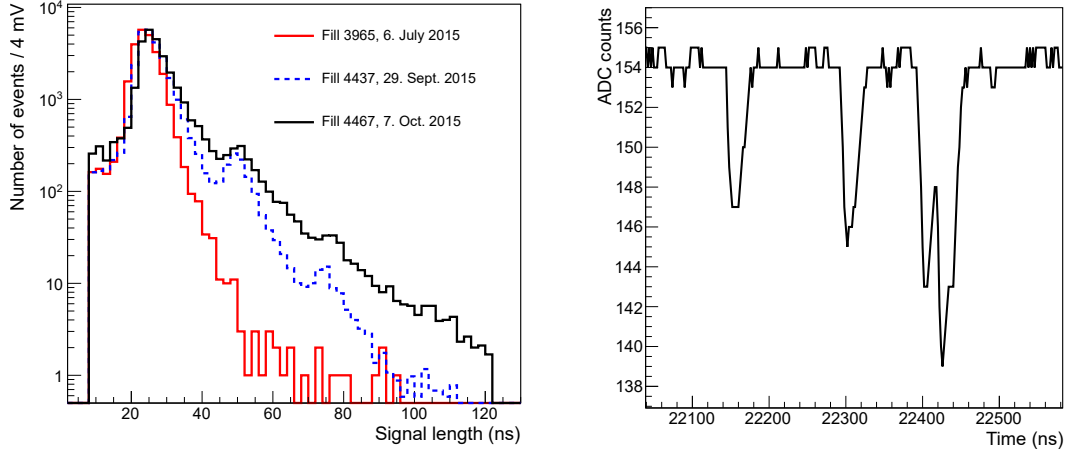


Figure 3.21: Left: Evolution observed in the signal length distribution with growing luminosity. Red line: reference Fill 3965, flux about $4 \cdot 10^6 \text{ MIP}/\text{cm}^2\text{s}$, integrated luminosity 12 pb^{-1} ; blue dashed line: Fill 4437, flux about $23 \cdot 10^6 \text{ MIP}/\text{cm}^2\text{s}$, integrated luminosity 1257 pb^{-1} ; black line: Fill 4467, flux about $28 \cdot 10^6 \text{ MIP}/\text{cm}^2\text{s}$, integrated luminosity 2107 pb^{-1} .

Right: An example of the ADC signal corresponding to the pile up of signals of two particles together with a couple of single hits.

The time over threshold distribution for Fill 4467, shown in Figure 3.21 left in a logarithmic scale is also shown in Figure 3.22 left in the linear scale. It is subdivided into three zones: signals shorter than 20 ns to the left of the pink line, signals between 20 ns and 40 ns between pink and green lines and longer than 40 ns signals to the right of the green line. For each zone the corresponding signal amplitude spectrum is shown in Figure 3.22 on the right. The pink spectrum corresponds to the short signals, the green to the long signals and the blue to the middle part of the time over threshold distribution. The histograms are not normalized. Short signals are mostly contributing to the left shoulder of the amplitude spectrum, but the signals longer than 40 ns are distributed along the whole time range. The resulting amplitude spectrum is the sum of three amplitude spectra obtained for different time over threshold zones and it is shown in black in Figure 3.18.

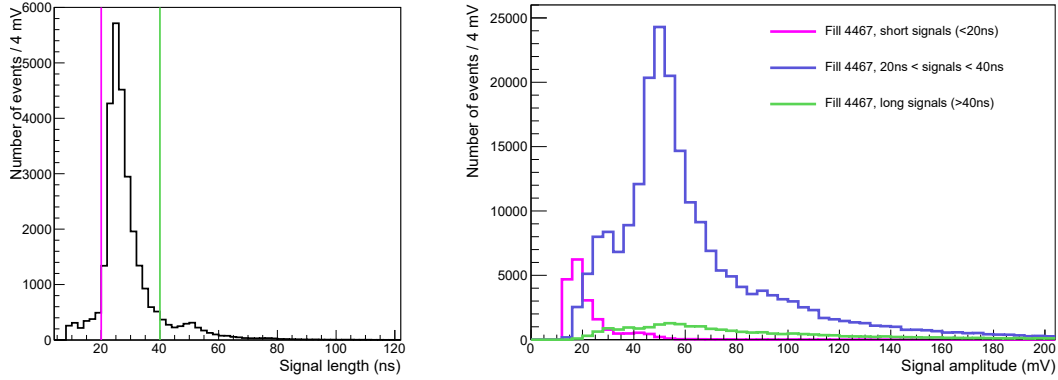


Figure 3.22: Left: Fill 4437 signal length distribution in linear scale divided into three zones. Right: Amplitude spectra obtained for the three different signal length zones: signals shorter than 20 ns (pink), signals between 20 ns and 40 ns (blue) and longer than 40 ns signals (green).

Difference of the sensor response on the particle hit position

The main contribution to the lower amplitudes in the spectrum is caused by the non metallized edges of the sensor and metallization gap. This is supported from the test beam data. A prototype of the BCM1F detector with a two-pad sensor was studied in the 5 GeV electron beam at DESY-II [79]. Using a beam telescope based on 6 pixel detectors it was possible to reconstruct the impact point of the beam particle on the sensor. The sensor response in different regions was studied. A similar technique was used for sapphire sensors study and will be described in detail in subsection 5.5.1.

Regions near the metallization edges and near the gap between the pads are investigated. Five narrow bands of 0.1 mm width were selected parallel to the metallization gap, as is shown in the diamond sketch inserted on the left side in Figure 3.23. In red color the reference band is shown. Using only tracks pointing in this particular band of the sensor, the reference amplitude spectrum, the red curve on both plots in Figure 3.23, was obtained.

In blue color two sensor bands near the metallization edge are marked on the sketch of the diamond sensor: the dashed line is for the not-metallized sensor edge and the solid line is for the edge of the metallization. Keeping the same color code the amplitude spectra obtained for the selected bands are shown in Figure 3.23 on the left. The MIP peak obtained for the band at the metallization edge has about a 20% lower value than the reference peak and is pushed in the direction of even lower amplitude values for the not metallized band. In black two bands of the sensor

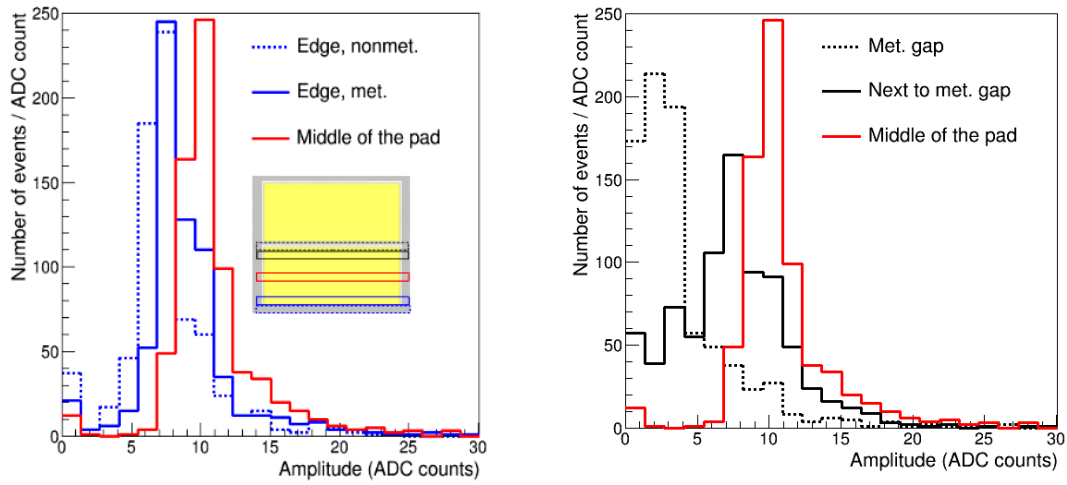


Figure 3.23: Amplitude spectra obtained for the BCM1F detector prototype in the DESY-II beam test. Only signals from beam electrons pointing in the narrow 0.1 mm wide sensor bands were selected. The sketch of the diamond sensor with selected narrow bands is inserted in the left plot. Amplitude spectra for selected bands of the sensor are shown. The color code of the marked bands correspond to the color code of the amplitude spectra.

next to the metallization gap are marked: the dashed line the band containing the metallization gap and the solid line the sensor band adjacent to the metallization gap, but not containing it. As it is seen on the corresponding amplitude spectra in Figure 3.23 on the right, the band containing the metallization gap shows an almost 80% drop of the MIP peak value. In the band adjacent to the metallization gap the amplitude spectra is much wider than the reference spectra and shows an about 20% lower MIP peak position. Such a strong effect on the signal amplitude is explained by a non-uniform field caused by the gap between two metallization pads, as it was shown in the simulation in Ref. [68].

The observed effects are not that pronounced in the amplitude spectra obtained for the whole pad, as they are scaled by a geometrical factor. The area of the inner metallization, where amplitude spectrum corresponds to reference spectrum is about 10 times bigger than the area around the metallization edges and the gap. One pad size is about $4 \times 2 \text{ mm}^2$, resulting in 8 mm^2 area. Taken on average, a 0.15 mm frame around the inner part of the metallization where the electric field is disturbed results in an area of about 0.9 mm^2 .

Coming back to amplitude spectrum obtained from the VME ADC data analysis, the black curve in Figure 3.18, we can summarize that the observed shoulder on the left side of the MIP peak is caused mostly by edge and metallization gap effects. The shoulder does not have the same size for different sensors and develops with irradiation. It is also pointing to individual dependence of the significance of the effect on the sensor material and metallization.

3.8.3 Observations during measurements

During the LHC commissioning there were occasions when the CMS magnet was off. We used this data to test the amplitude spectra with “magnet on” and “magnet off”. The data sets used should be close in time to exclude effects of radiation damage or operation conditions except the one under test. Fill 4540 with magnet off and Fill 4555 with magnet on were used. There were no fills in between, but the initial intensity and the filling schemes were different. 2232 bunches were colliding in the Fill 4540, corresponding to a particle flux of about $38 \text{ MIP}/\text{cm}^2\text{s}$ and resulting in an initial luminosity of $3677 \times 10^{30} \text{ cm}^{-2}\text{s}^{-1}$. In Fill 4555 there were 589 colliding bunches, corresponding to a particle flux of about $10 \text{ MIP}/\text{cm}^2\text{s}$ and an initial luminosity of $1361 \times 10^{30} \text{ cm}^{-2}\text{s}^{-1}$. Therefore this study is testing magnet on/off and different filling conditions.

Spectra were obtained applying a 12 mV threshold and MPVs were determined from the fit with a Landau distribution. Results are shown in Figure 3.24. Black dots correspond to the Fill 4555 with magnet on, blue and red dots correspond to Fill 4540 with magnet off. There is no systematic change of the MPV value found.

For illustration, the amplitude spectra with the fit with a Landau distribution

Chapter 3. BCM1F detector as luminometer

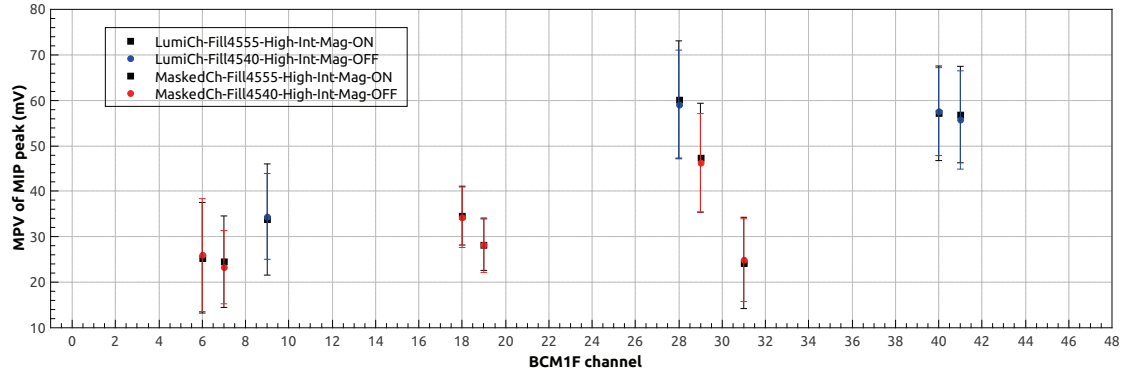


Figure 3.24: The comparison of the MPVs at October 30 (Fill 4555 in black, magnet on, low initial luminosity) and at October 27 (Fill 4540, magnet off, high initial luminosity, masked channels in red and channels used for the luminosity measurement in blue).

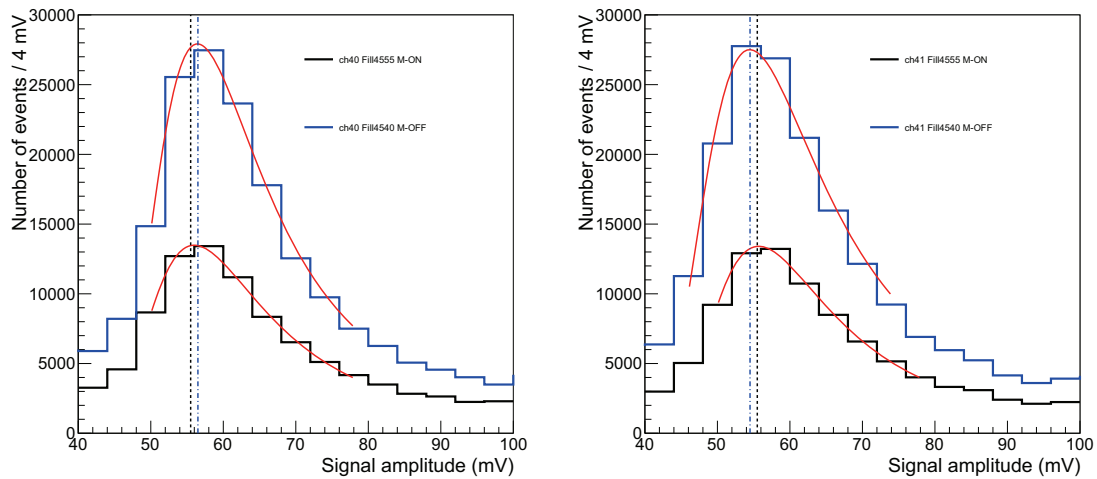


Figure 3.25: The comparison of the MPVs for channel 40 (left) and 41 (right) with magnet on/off and different beam intensities. Blue histogram: magnet off, high intensity, Fill 4540; black histogram: magnet on, low intensity, Fill 4555; the red line is the result of the fit with a Landau distribution, the black dashed and the blue dash-dotted line the MPV position in the corresponding histogram.

for two luminosity channels corresponding to one diamond sensor are shown in

Figure 3.25: on the left for channel 40, on the right for channel 41. In black color is shown the amplitude spectrum of the data set collected during the Fill 4555 with lower luminosity, in blue the spectrum of the data set collected during the Fill 4540 with higher luminosity. The red lines correspond to the fits. The black dashed line and the blue dash-dotted line were added to point to the MPV positions in the corresponding spectra. The difference of the MPV positions of both channels is less the 1 mV . Hence, the MPV values do not depend on magnet conditions or filling schemes.

Erratic signals

During the commissioning period of the BCM1F detector an unexpected erratic behavior of some channels appeared. In online measurements it was reflected in the fast rise of the RHU counting rates of one order or a couple of orders of magnitude. The observed erratic counting rates could disappear after a short time for some of the channels, but for other channels it caused high voltage supply trips. Taking into account the extremely low leakage current of diamond sensors in pA range and signal currents in the nA range as measured in the laboratory up to 1000 V with a 37 MBq ^{90}Sr source, the high voltage supply trip threshold was set to 3 μA . It is not known what caused such behavior of the sensors, but for operation it had to be prevented. For channels, which were showing erratic rates the bias voltage was lowered to stabilize the behavior. These sensors were not included in the luminosity or background measurements, but they were still useful for radiation damage studies.

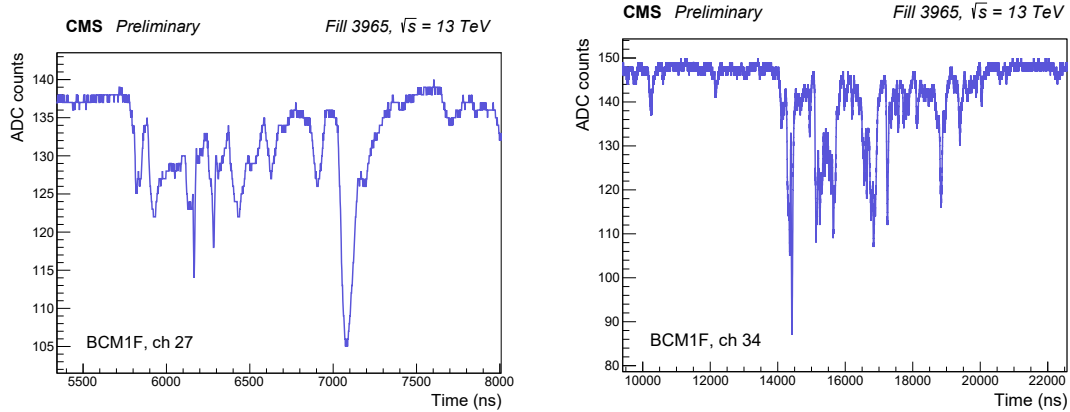


Figure 3.26: An example of the erratic behavior of channel 27 (left) and channel 34 (right). The analog signal is shown as a function of time.

Using ADC data it is possible to investigate the analog signal as a function of time for sensors becoming erratic. An example of the analog signal in some

channels recorded by the ADC is shown in Figure 3.26. Some signals reach a couple of hundred ns signal length. This data originates from the low luminosity Fill 3965, where no saturation of the electronics or simultaneous particle hits were seen. The orbits, containing erratic events were excluded from the further analysis using a signal length filter in the program. The fraction of such events was found in Fill 3965 to be $<1\%$.

3.8.4 Web monitoring tool

The ADC data acquisition was automated to start and stop using a computer program synchronizer called a cron job, which is running up to now. It is checking the LHC beam status and activating the data acquisition program every time when the beam status “Stable beams” is declared. For each fill about 10 minutes of data is saved and analyzed. For long fills every 3 hours an additional data file is saved for offline analysis. For the first data file of the fill the analysis is done directly after the file was saved. The logic of the ROOT-based analysis code was described in section 3.7. The amplitude spectra of particle hits, the test pulse spectra, the baseline position and baseline standard deviation histograms are produced and saved in .root and .png formats into a separate folder. Also the mean values of the test pulse position and the baseline position histograms are written in a text file for each channel. This way it is easy to check the performance of each channel in the particular LHC fill.

To make it possible to compare different channels or to track particular channel performances during long time period a monitoring web page was created. Plots and text files, produced for each fill are copied to another server and then published online under <http://srv-s2d16-22-01.cms/webmonitor/bcm1f-adc> [80]. Special proxy server settings are required to display the web page. The text files with baseline and test pulse position information from each fill are used to update plots as illustrated in Figure 3.27. On the left side the baseline position for the set of the BCM1F channels is shown as a function of the fill number. Pointing with the cursor on a certain line it is highlighted and a box with fill number, channel number and precise value of the baseline at the particular point is popping-up. On the bottom of the figure the active channels are shown in color and hidden channels are shown in gray. Channels can be set back to active by mouse click on the channel number. On the right a similar plot is shown for the test pulse position. On the top right corner a menu is seen, which allows to save the plot in different formats. It is also possible to zoom in and zoom out.

Any of the .png plots can be displayed by setting fill number, channel number or a time interval in the filters seen on the top of Figure 3.28. A set of the particular files or a set of channels for comparison can also be selected. On the bottom of Figure 3.28 the amplitude spectra of channel 44 for three selected fills are displayed. Fills well-

Chapter 3. BCM1F detector as luminometer

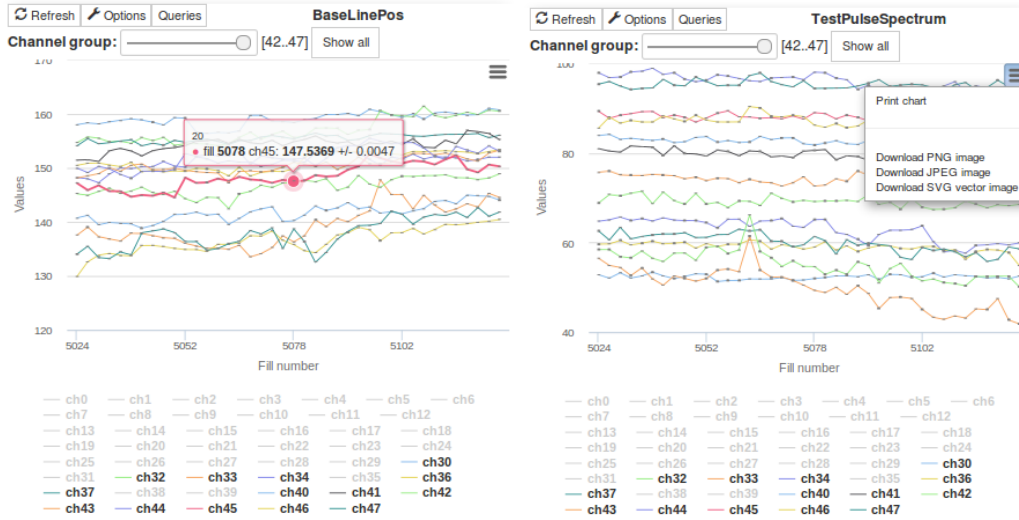


Figure 3.27: Left: The baseline positions for the set of channels as a function of the fill number. Right: The test pulse amplitude spectra mean value positions for the set of channels as a function of the fill number.

separated in time are selected, thus changes in the spectra are very pronounced.

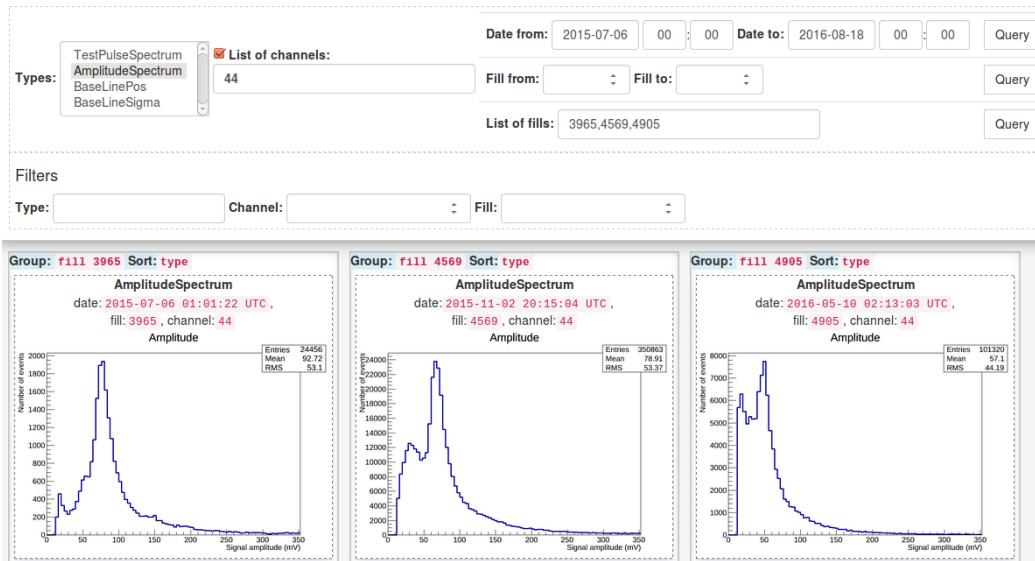


Figure 3.28: The screen shot of the ADC data monitoring web page. The amplitude spectra of channel 44 for three selected fills.

Chapter 4

Measurements of the luminosity using BCM1F

4.1 BCM1F rate measurements using the Real-time Histogramming Unit

RHU modules, described in subsection 3.5.2, are used for online BCM1F rate measurements. Although it is expected that each channel measures almost the same hit rate, in practice the rates differ significantly. This is due to conditions like larger noise in a few channels requiring a higher discriminator threshold, differences in the sensor efficiency due to progressive radiation damage or a reduced bias voltage. In the future these inefficiencies will be corrected for, but at the moment they are accounted for by normalizing the rates to an average of all channels.

Channels that have consistently low performance, e.g. low efficiency or erratic signals, are omitted from the luminosity measurement via a permanent channel mask. However, during Run II it was observed that a number of channels jumped occasionally to high count rates for a short time. To account for this, an automatic channel-masking algorithm was developed to mask these channels temporarily [75]. The rates in the central 50% of the channels are taken as a reference. The mean values and standard deviations of the normalized rates in these channels are calculated. Channels whose rate falls outside of 6 sigma from the mean are excluded from the luminosity calculation for the corresponding four lumi-nibbles. In addition, the list of permanently- and temporarily-masked channels is sent along with the luminosity values for offline storage.

The software used to read the data out of the RHU is implemented in the CMS online data-taking software framework XDAQ [81, 82]. The system is modular, so that the data is passed from element to element through an eventing bus. The module that interfaces with the RHU hardware is called the source. The source

collects the RHU histograms and passes them over the eventing bus to the processor, the module that uses the zero-counting algorithm to calculate the luminosity as well as background values, along with monitoring information and aggregated channel rate histograms for offline analysis, as is shown in Figure 4.1. It will be described in more detail in subsections 4.1.1 and 4.1.2. The calculated values are then passed from the processor over the eventing bus to the upstream data collector, which publishes the values online and stores them for offline use. RHU count rates during the van der Meer scan are used to calibrate BCM1F as a luminometer.

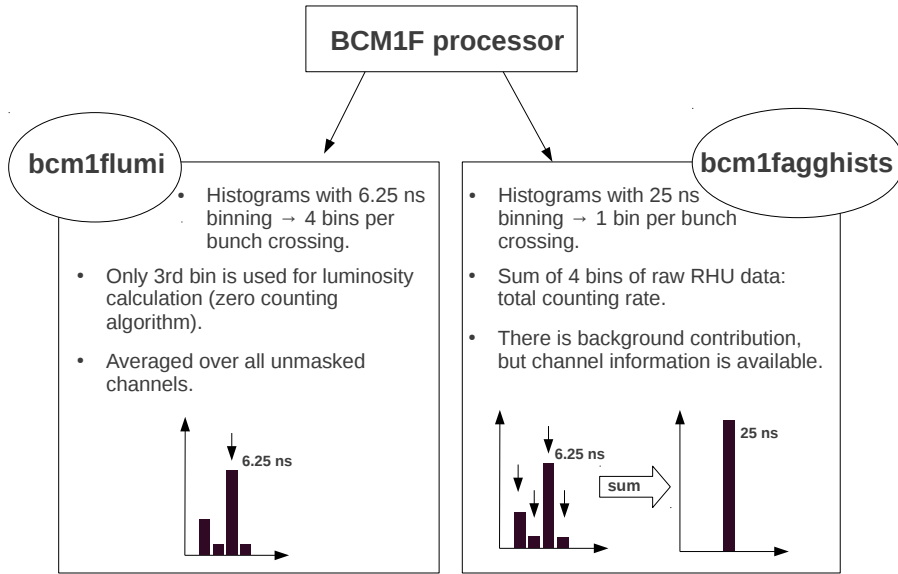


Figure 4.1: The BCM1F processor logic. Left: online luminosity, 6.25 ns bin width (third bin of RHU data). Right: aggregated channel rate histograms, 25 ns bin width (sum of 4 RHU bins).

4.1.1 Online Luminosity calculation

The RHU histograms accumulated over four luminosity nibbles contain 4 bins per bunch crossing. The content of the third bin is used for luminosity calculation. It is divided by the number of orbits, amounting to 16384, and then subtracted from 1, giving the fraction of zero counts $p(0)$. Eq. 2.16 is then used to determine the mean value of hits μ for each bunch crossing per orbit. The luminosity per bunch

crossing is obtained as

$$L(BCID) = \frac{\mu}{\sigma_{vis}} \cdot f, \quad (4.1)$$

where BCID is the Bunch Crossing IDentification number. For each four luminosity nibbles the average of $L(BCID)$ over all unmasked channels is calculated, stored, and sent as the online luminosity to CMS and LHC. The stored values are used in the van der Meer scan analysis below.

4.1.2 Aggregated channel rate histograms

From the raw RHU histograms aggregated histograms (agghists) are produced summing the 4 bins of raw data for each bunch crossing. The aggregated count rates of each bunch crossing are passed to the upstream data collector and published on the online monitors in the CMS control room to get a raw information on the total rate and its stability within a fill. An example of RHU rates seen on the online displays during the imaging beams scan of Fill 4937 from two RHU modules is shown in Figure 4.2. It is seen, that some channels have lower count rate, as lower bias voltage was applied to those channels.

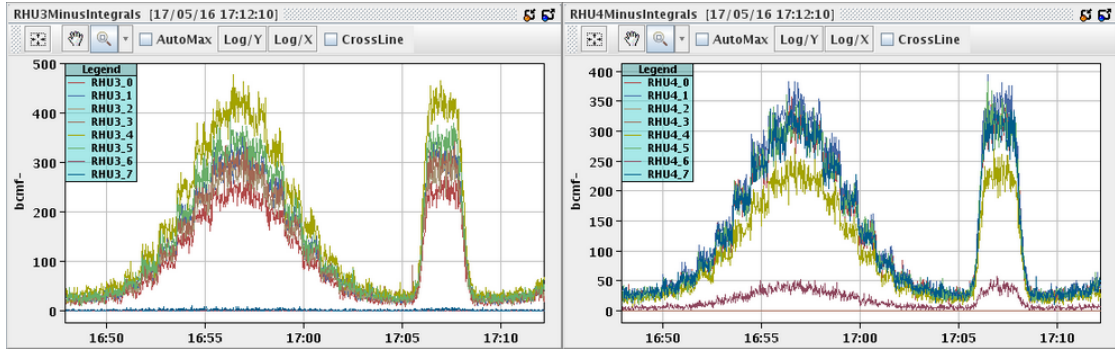


Figure 4.2: Fill 4937, imaging VdM scan: an example of RHU rates seen on the online displays in the CMS control room.

The aggregated histograms were also used for offline analysis, e.g. in the channel-by-channel van der Meer scan analysis in 2015. In the measurement of the quantities Σ_X and Σ_Y and the visible cross section the MIB background contribution, present in the aggregated histograms, was taken into account and corrected for. Later in 2016 for offline analysis the luminosity relevant third-bin-only information was stored per-channel.

4.2 VdM scan in August 2015

The van der Meer scan program on August 25th 2015 (Fill 4266) comprised several scans in the x and y planes and 3 Length Scale Scans (LSS). In each beam 30 colliding and 28 non-colliding bunches were stored, grouped in 4 bunch trains and one well separated single bunch, denoted as last BCID. The energy per beam was 6500 GeV, the magnetic field in CMS 3.8 T and the beam optics settings $\beta^* = 1917.0$ cm.

At the beginning, in session 1, CROSSING (x) and SEPARATION (y) scans, in which both beams were moved, were performed, hereinafter referred to as Scan pair 1. The beams were scanned up to $\pm 3 \sigma$ in steps of 0.25σ of the beam width ($6 \sigma = 612 \mu\text{m}$ in total). The position of the beams with zero separation, when maximum count rate is reached, is referred to hereinafter as head-on position. After each scan beams were brought to head-on position, then the next scan began. The scan pair after Scan pair 1, Scan pair 2, is of the same type, but the order of the scans was opposite: y scan was done first, x scan after it. After the length-scale calibration in the x - and y -directions, Scan pair 3 (x, y) and Scan pair 4 (x, y) were performed. These scans are imaging scans: one beam was kept fixed, and the other beam was moved across it to obtain an image of a beam. In Scan pair 3 beam 2 was kept fix and beam 1 was moved in steps of 0.5σ up to a separation of $\pm 4.5 \sigma$, resulting in 19 measurement points. In Scan pair 4 beam 1 was fixed, and beam 2 was moved across it in the same 19 steps. Between Scan pair 4 and Scan pair 5 a second LSS in the x plane was done. The LSS will be discussed in subsection 4.2.6. The last Scan pair 5 was done to test the reproducibility. It started from y in head-on position. In the first scan in x each beam was moved up to a separation of $\pm 3 \sigma$ in steps of 0.25σ , resulting in 25 points as in Scan pair 1.

For all described scans the count rate from the aggregated histograms as a function of time is shown in Figure 4.3. The shapes of the distributions obtained in the van der Meer scans are similar to a Gaussian.

The pattern of the filled bunches, in terms of BCID, was the following:

- The first train of colliding bunches, filled in both beams: 1, 51, 91, 131, 171, 211, 251, 291
- The first train of non-colliding bunches: 351, 391 (beam 1), 491, 531, 571 (beam 2), 591 (beam 1), 611 (beam 2), 631 (beam 1), 651, 691 (beam 2)
- The second train of colliding bunches, filled in both beams: 771, 811, 851, 891, 931, 971, 1011
- The second train of non-colliding bunches: 1242, 1282 (beam 2), 1385, 1425, 1465, 1505, 1545, 1585 (beam 1)

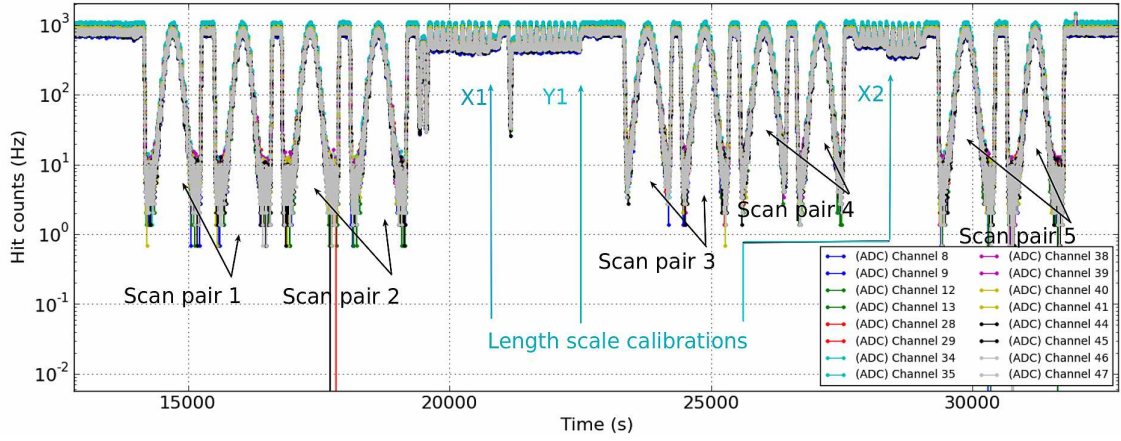


Figure 4.3: RHU rates for unmasked channels during VdM Fill 4266 as a function of time. The Gaussian-like shapes correspond to VdM scans. In between three length scale calibrations are seen. The scan pairs 1, 2 and 5 are standard VdM scans, and the scan pairs 3 and 4 are imaging VdM scans [75].

- The third train of colliding bunches, filled in both beams: 1631, 1671, 1711, 1751, 1791, 1831, 1871
- The third train of non-colliding bunches: 1921, 1961, 2001, 2041 (beam 1)
- The fourth train of colliding bunches, filled in both beams: 2211, 2251, 2291, 2331, 2371, 2411, 2451
- The isolated colliding bunch 2674
- The fourth train of non-colliding bunches: 2812, 2852, 2892, 2932, 3051, 3091 (beam 2)

This pattern is very well seen in Figure 4.4. For colliding bunches the count rates are two orders of magnitude higher than for non-colliding bunches.

It is important to notice that both colliding and non-colliding bunch trains in each beam were equidistant with 40 BCIDs spacing, except for the isolated colliding bunch with BCID 2674. Also the 1st and 2nd non-colliding bunch trains were filled alternating with bunches in beam 1 and beam 2. The 3rd non-colliding bunch train comprises 4 bunches only in beam 2 and the 4th non-colliding bunch train, 6 bunches only in beam 1. The rate values observed for all of them are comparable.

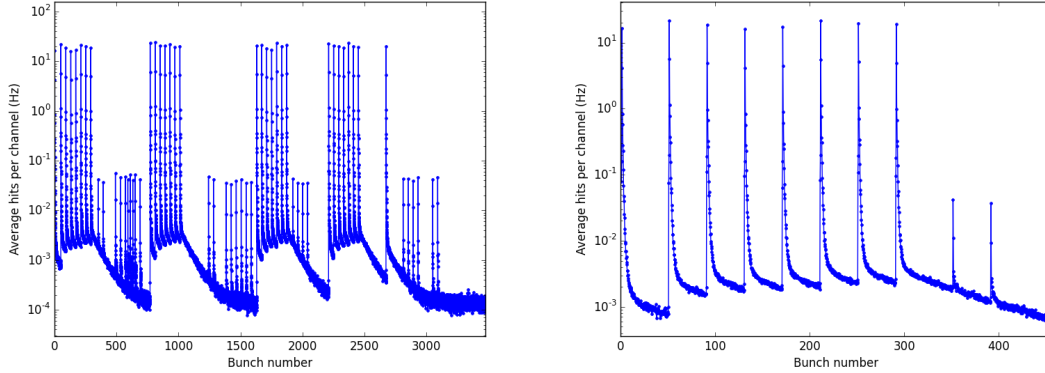


Figure 4.4: RHU raw rates from one end of BCM1F accumulated during 3 hours in the Fill 4266 before the VdM scan happened. Left: whole orbit, right: zoom into one bunch train [75].

4.2.1 Van der Meer scan analysis framework

The van der Meer scan analysis framework [83] was developed to standardize the VdM analysis for all subsystems. It allows one to produce and compare results in a relatively short time. The framework is written in *Python* [84]. *ROOT* [85] is used from *Python* via its interface module *PyRoot*. Output data is stored in the .root files for visualization and plotting and in .pkl files to provide a quick access to the data during further processing. Other formats (CSV, plain text) are produced from .pkl files and can be added by user.

The framework is complicated and consists of a collection of scripts. Some of them are used to prepare the various input files, receiving information from different sources, the other are used to carry out the actual analysis and to prepare input files for the following analysis stage. A so-called “Driver” program is used to select/unselect analysis stages.

Five main stages and optional correction stages of the analysis have to be mentioned:

- *Production of the scan file.* An input file for the framework Driver program in .json format have to be filled by user. It contains timestamps for VdM scans to be processed, active analysis stages, paths to analysis folders. Availability of files and compatibility of scans and timestamps is done by the framework. The produced scan file contains selected time information per scan point and is an input for the next stage.
- *Rates and beam current files production.* Information from the Luminosity

database, centrally produced XDAQ files in .hd5 format, the LHC database(s) and the output of CMSSW jobs are read and converted to standardized files in .pkl that comprise the input to the analysis layer. At the commissioning stage all files had to be copied by user to predefined directories.

- Optional corrections as for beam-beam effects, ghosts and satellites contribution or length scale as described in detail in the following sections.
- *Graphics production.* The standardized information from scan files and rate files normalized by beam currents are used to produce *ROOT TGraph* objects, which serve as input to the fitting stage. Various corrections to the input data from the luminometers can be applied at this stage.
- *Fitting.* This stage takes the input from the previous stages and uses it to perform fits to the VdM scan data. Details will be described in section 4.2.2.
- *σ_{vis} calculation.* This stage takes the results from the fits and uses them to derive an overall visible cross section for the luminometer using all BCIDs.

The framework is open for modifications, customer needs implementation and further development.

4.2.2 Fits of the rate as a function of the relative displacement of the beams

The procedure for a van der Meer scan using a single bunch crossing is described in the following. The rate is measured as a function of the relative displacement of the beams, Δ . In the ideal case this distribution can be described by a Gaussian. Considering the dependence on displacement,

$$f_G(\Delta) = A \cdot e^{-\frac{(\Delta-\mu)^2}{2\Sigma_x^2}}, \quad (4.2)$$

the area under the peak is equal to $\sqrt{2\pi} \cdot A \cdot \Sigma_x$. For zero separation the value of the counting rate is $R_{peak_x} = f_G(0)$ [40].

In practice there are tails in the distributions, originating from beam halo, which introduce deviations from an ideal Gaussian beam profile. They are taken into account by choosing a superposition of two Gaussians with different widths and a constant term. The ansatz is then

$$f_{DG}(\Delta) = A \cdot \left[\frac{h}{\sqrt{2\pi} \cdot \Sigma_{x1}} \cdot e^{-\frac{(\Delta-\mu)^2}{2\Sigma_{x1}^2}} + \frac{1-h}{\sqrt{2\pi} \cdot \Sigma_{x2}} \cdot e^{-\frac{(\Delta-\mu)^2}{2\Sigma_{x2}^2}} \right] + C, \quad (4.3)$$

where $\Sigma_{x1} = \Sigma_{eff} \cdot (h + r(1-h))$ and $\Sigma_{x2} = \Sigma_{eff} \cdot \frac{(h+r(1-h))}{r}$.

The parameter h is the fraction of the first Gaussian in the fit, $r = \frac{\Sigma_{x1}}{\Sigma_{x2}}$, A is the area under the double Gaussian function and C is used for estimation of the background. The peak value of the rate is obtained as $R_{peak_x} = f_{DG}(0) - C$.

Table 4.1: The fit results for σ_{vis} using different approaches to describe the rates as a function of the beam displacements.

Fit function	σ_{vis}	standard deviation	$\sigma_{vis \text{ weighted}}$	$\sigma_{vis \text{ weighted}}$ std. dev.	χ^2/NDF
Scan pair 1					
SGConst	244.46	1.50	246.52	0.17	2.2
DG	253.85	12.79	253.06	0.18	1.5
DGConst	246.11	1.92	245.95	0.26	1.4
Scan pair 2					
SGConst	248.03	1.31	247.94	0.17	1.7
DG	254.79	9.00	254.37	0.18	1.5
DGConst	247.66	1.66	247.58	0.35	1.5
Scan pair 3					
SGConst	240.96	1.28	240.89	0.16	1.9
DG	248.19	9.39	247.49	0.18	1.5
DGConst	243.38	2.40	242.75	0.36	1.5
Scan pair 4					
SGConst	241.91	1.38	244.84	0.17	2.0
DG	251.72	10.68	251.27	0.19	1.4
DGConst	247.75	3.13	247.08	0.38	1.5
Scan pair 5					
SGConst	247.58	1.69	247.50	0.20	2.7
DG	250.49	1.79	250.37	0.17	1.6
DGConst	247.38	1.93	247.19	0.36	1.5

σ_{vis} is calculated using Eq. 2.3 and extracted fit parameters for each bunch crossing. The values obtained for mean σ_{vis} value averaged over all bunch crossings and its standard deviation, as well as weighted mean $\sigma_{vis \text{ weighted}}$ value and its standard deviation are compared in Table 4.1 for fits with a single Gaussian plus a constant, referred to as SGConst, a superposition of two Gaussians, referred to as DG, and a superposition of two Gaussians plus a constant background, referred to as DGConst. Weighted mean for the visible cross sections obtained in each bunch crossing was

calculated as:

$$\sigma_{vis \text{ weighted}} = \frac{1}{\omega} \sum_{i=1}^N \omega_i \sigma_{vis \ i}, \quad (4.4)$$

where weights are defined as $\omega_i = 1/s_i^2$, s_i the standard deviation of $\sigma_{vis \ i}$ defined in one bunch crossing number i , $\omega = \sum_i \omega_i$. The standard deviation of $\sigma_{vis \ weighted}$ is $1/\sqrt{\omega}$.

The best fit results in terms of χ^2/NDF are obtained in most cases using a superposition of two Gaussians and a constant background. Examples for a fit using Eq. 4.3 are shown in Figure 4.5 for BCID 1711. The rate as a function of the displacement is well described, even in the tails, and the residuals scatter around zero. The residuals are the difference of the measured rate and the fit value for each separation value Δ divided by the statistical error of the measured rate, hence being the deviation in units of the statistical error of each rate measurement. The error bars on the residuals are then set to ± 1 . The constant term in the VdM fits results from the MIB contribution and explained in more detail in the next section.

4.2.3 Influence of the beam current measurement on σ_{vis}

As the rates measured during the VdM scan are normalized by the product of beam 1 and beam 2 bunch currents, the bias on the bunch currents affects the measured σ_{vis} . Different devices for bunch current measurement with different measurement frequency are available at the LHC. Two of them are used for a cross check of bunch currents and for comparison of σ_{vis} obtained using different bunch current monitors, as described below. The measurement of the bunch currents allows the constrain of the quantity $N_1 \cdot N_2 \cdot f \cdot n_b$ used in Eq. 2.1.

The LHC is equipped with two Beam Current Transformers [86] (BCT), and a Beam Quality Monitor (BQM). The first BCT, the Direct Current Current Transformers (DCCTs), comprises four DCCTs, two per ring of circulating beam. One on each beam (called system A) is declared as online or operation, while the other (system B) is declared as offline or spare. They work as transformers to measure the total beam current circulating in each LHC ring. The DCCT calibration is obtained with a current generator sending a known current through a dedicated coil allowing the calibration of the whole acquisition chain. It is performed separately for different DCCT operational ranges [87]. The DCCTs are very precise, but too slow for bunch-by-bunch measurements. The total uncertainty on the beam current of about 0.3% was estimated for the van der Meer scan Fill 4266 in August 2015 [88]. The following contributions to the uncertainty in this range are taken into account:

- the current source precision;

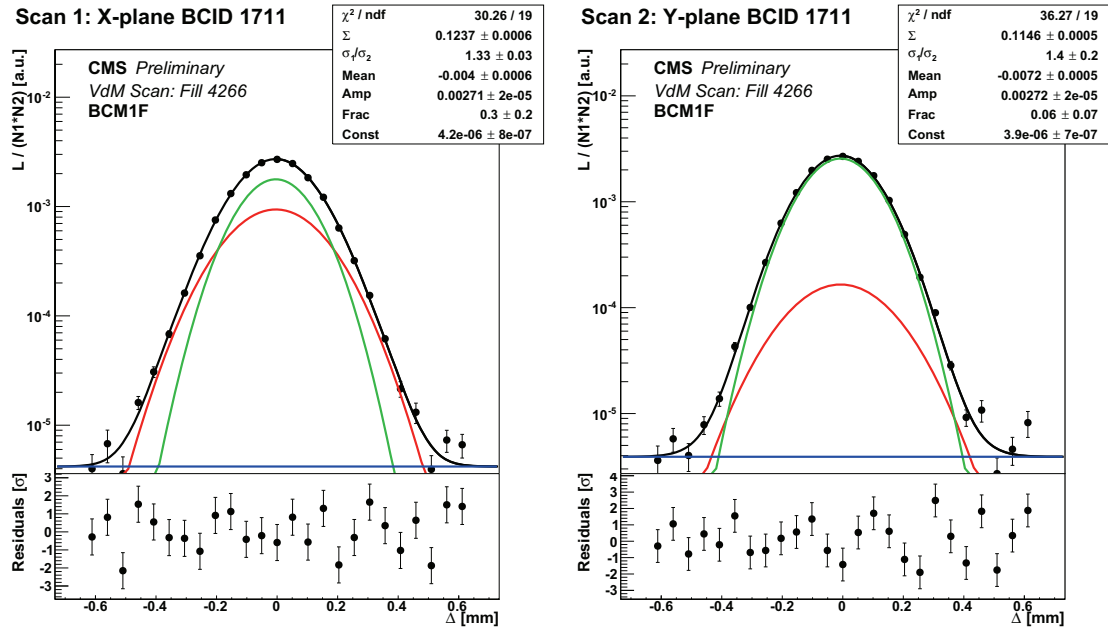


Figure 4.5: Rates as a function of the displacement for VdM scan in x and y plane and fit results using Eq. 4.3 for BCID 1711. Two Gaussian fits are shown in red and green, the constant term in blue and the resulting fit in black. Black dots are the measured rate values for each displacement. Also given are the residuals of the fit in units of the statistical errors of the measured rates.

- the bunch pattern dependence;
- the nonlinearity of the 12-bit ADC;
- the stability of the ADC baseline and the precision of baseline corrections;
- the long term stability of the baseline and the calibration;
- the differences in the measurements of the A and B systems.

The second BCT is the Fast Beam Current Transformers (FBCT) for each of the rings. The FBCT measures the beam current in a 25 ns window, i.e. including all particles in 10 RF buckets. However, the charge per bucket must be above a pre-set threshold. The small satellites and in addition the ghosts (see section 4.2.4) are not measured by the FBCT. The measurement of the FBCT can be compared and normalized to DCCT measurement if needed.

The LHC BQM [89] is capable of measuring the bunch charge in 2.5 ns RF buckets. It is sampled only every 30-40 seconds. Therefore for some of the VdM scan points, which are measured every 30 seconds, the BQM current measurement might be not available. The values for the beam currents for scan points with no BQM measurement are interpolated using two neighbor measurements.

The values obtained for σ_{vis} from VdM scans for all colliding bunches using the beam currents measured by FBCT and BQM are shown in Figure 4.6.

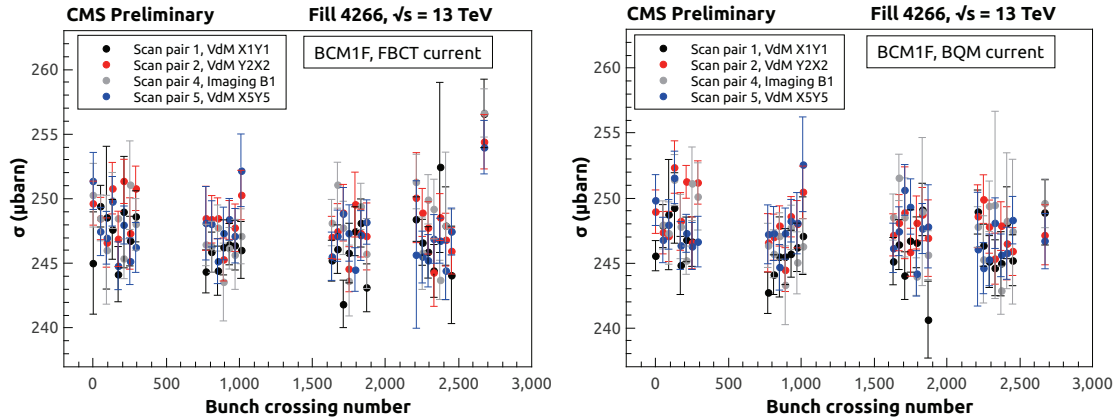


Figure 4.6: The visible cross section as a function of BCID for several van der Meer scans. Left: beam current measured using FBCT. Right: Beam current measured with the BQM.

As can be seen, the measured values for σ_{vis} are in agreement within their uncertainties, apart from the value measured using the FBCT current for the last bunch

crossing. This is also illustrated by the distribution of the ratio between values of σ_{vis} measured using the FBCT and the BQM, as shown in Figure 4.7 (left). This ratio is spread around 1 with two outliers at 1.03. One of them results from the last bunch crossing. The other one is due to a bad beam shape fit for one of the BCIDs.

Figure 4.7 (right) shows the product of the beam currents in the VdM Scan 1 measured by FBCT and BQM. For the last bunch crossing the measured values from FBCT and BQM disagree. For this BCID a bias in the FBCT measurement was confirmed by other beam current measurement systems, e.g. the Longitudinal Density Monitors (LDMs). The BQM measurements of the bunch current were used in the further VdM analysis.

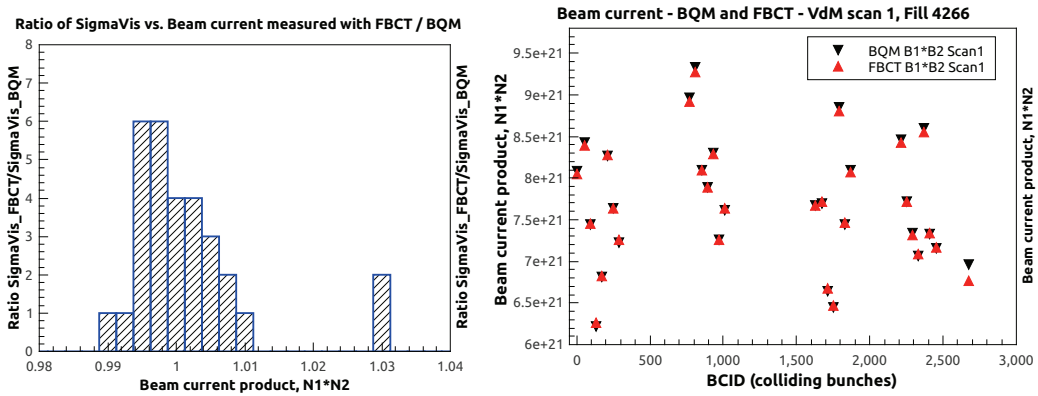


Figure 4.7: Left: The ratio of the visible cross sections determined using FBCT and the BQM current measurements. Right: The product of the currents of the two beams measured by FBCT and BQM in the VdM Scan 1 as a function of the BCID.

4.2.4 Contribution of satellite bunches and ghosts to the beam current measurement

Eq. 2.1 is valid for bunches contributing to the luminosity recorded by the detector. However, buckets neighboring the filled bucket or even randomly distributed buckets might carry particles contributing to the count rate in the luminometers but are not included in the quantities N_1 , N_2 and n_b . For operation with 25 ns bunch spacing, each 10th RF bucket is normally filled. Particles in any of the other nine RF buckets are called “satellites” and have to be taken into account as a beam current correction or as systematic uncertainty, because they contribute to the count rate in the VdM scan. In addition, particles in RF buckets outside the filled bunch trains are called “ghosts”. Both satellites and ghosts contribute to the beam current measurements in the storage ring.

The amount of particles in the ghosts is estimated from interactions with residual gas atoms in the vacuum chamber. The rate from nominally empty bunch crossings is compared with the rate of crossings of a bunch of known charge in only one beam. Using this technique, the fraction of ghost particles was estimated by LHCb in VdM Fill 4266 to be about 0.10 % for beam 1 and 0.13 % for beam 2 [90]. The time resolution of this measurement does not allow one to estimate the contributions from satellites in the rate from the single bunches. However, using the LDMS with a time resolution of 50 ps this contribution was estimated from the measurement of the synchrotron radiation photons. The contribution of both ghosts and satellites was estimated in Fill 4266 for beam 1 and beam 2 to be about 0.11 % and 0.07 %, respectively [91]. Since these contributions to the current measurements are very small, they are not applied as a correction but taken into account as a systematic uncertainty of 0.2 %.

4.2.5 Contributions from MIB and albedo to the rates measured in the VdM scan

RHU rates accumulated before the VdM scan are shown in Figure 4.4 as a function of the BCID. The higher spikes correspond to colliding bunches and the lower to non-colliding bunches. As can be seen in the zoom in the right figure the distributions show after the time of each bunch crossing a tail of delayed hits. These hits are due to slowly moving particles and activation of the material, hereafter referred to as albedo. Some of these hits are delayed in the time slot of the next bunch crossing. In addition, the MIB of the outgoing beam is in time with the collision products, and contributes to the rate measured in the luminosity bin. Under stable beam conditions the MIB rate does not scale with the luminosity, hence it is a constant contribution to the rate measured as a function of the beam separation. In the 2015 VdM scan the rates for colliding and non-colliding bunches are $20.134 \pm 2.033 \text{ Hz}$ and $0.042 \pm 0.006 \text{ Hz}$, respectively. Hence, a fraction of about $2 \cdot 10^{-3}$ in the rate at R_{peak} originated from MIB. This number is in agreement with the fraction value of the constant term in the fits shown in Figure 4.5 of about $1.6 \cdot 10^{-3}$.

In the next iteration of the analysis the MIB contribution was subtracted from the RHU rates before performing the fits. It was obtained by averaging the rate of all 28 non-colliding bunches. Then this average MIB rate was subtracted from the rate of each colliding bunch. The average rate for non-colliding bunches was calculated for each separation step, and it was confirmed that it remains constant and corresponds to about $1.8 \cdot 10^{-6}$ during the VdM scan. The corrected rates as a function of the displacement Δ were fitted again. The comparison of the values for the constant term obtained for Scan pair 1 with and without MIB subtraction is shown in Figure 4.8 (left). The values in pink and red colors are the constant terms

of the fits in x and y scans before MIB subtraction and the values in dark and light blue are the constant terms after MIB subtraction. Values estimated to be $< 10^{-7}$ were considered to be negligible and not shown in the plot. As can be seen, the values of the constant term were reduced by a factor of about two, from $4.2 \cdot 10^{-6}$ to $1.9 \cdot 10^{-6}$.

The visible cross section per BCID was also recalculated. From Figure 4.8 (right) it can be concluded that the visible cross section did not change. This is expected, since the MIB contribution is properly taken into account by the constant term of the fit. The average visible cross section values calculated before and after MIB subtraction are $246.11 \mu\text{b}$ and $245.9 \mu\text{b}$, respectively. The BQM current measurements were used for rates normalization in both cases.

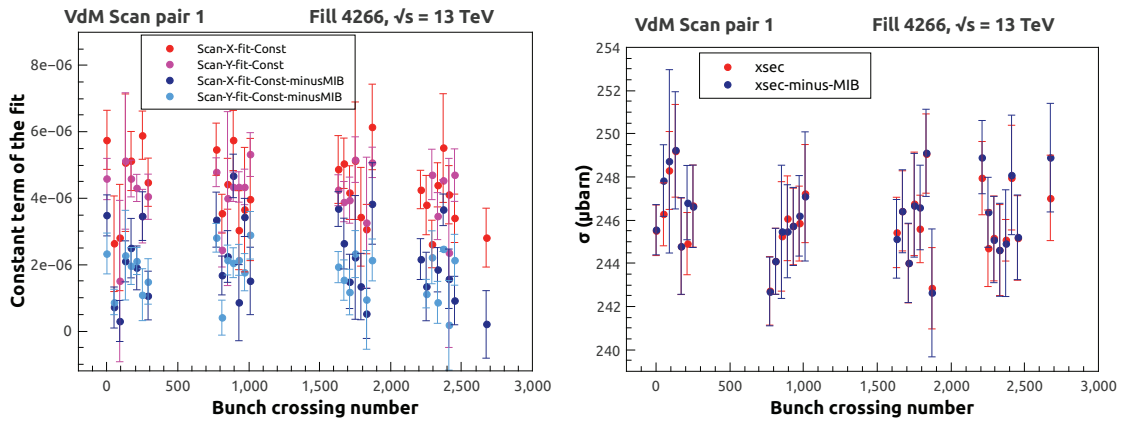


Figure 4.8: Left: the constant term extracted from the DGConst fit of the rates distribution with and without machine induced background subtraction. Pink and red points correspond to constant terms of the fits in x and y scans before MIB subtraction; dark and light blue points result from x and y scans after MIB subtraction. Right: The visible cross section calculated with (dark blue) and without (red) MIB subtraction.

From the count rate as a function of the BCID, shown in Figure 4.4 (right), it is seen that the contribution from albedo is counted in the luminosity bin of the following bunch crossing, in particular at the end of the bunch train. The fraction of albedo hits is estimated to be $2 \cdot 10^{-3} / 2 \cdot 10^1 \simeq 0.0001$, and considered as being negligible during the VdM scan.

4.2.6 Length scale scan

The LSS was performed to calibrate the beam positions in the steps of the VdM scan. The movement of the beams is performed by changing the current in the magnets of the final focus systems. The LSS delivers a mapping between the magnet current and the beam position in x and y coordinates. It is performed using the luminometers and the tracking system.

The LHC beam optics were adjusted to a $\beta^* = 19$ m and a transverse emittance of $\varepsilon = 3.7 \mu\text{m}$. These beam parameters hold for the beam width $\sigma = \sqrt{\varepsilon} / \beta^* = 102 \mu\text{m}$. Assuming that both beams have the same width σ , the convoluted beam size is $\Sigma = \sqrt{2}\sigma = 130 \mu\text{m}$.

Measurement procedure

The LSS calibration is performed in the x and y planes separately. The calibration in each plane comprises a set of measurements of the count rates in the luminometers at a constant separation of the beams of about 1Σ . In each position, data was taken for about a minute and the distribution of the vertices in the (x, y) plane was used to determine the position of the luminous region inside the vacuum chamber. The left part of Figure 4.9 illustrates one measurement. It starts with head-on collisions, where the beam spot is at the same position for both beams, then the beams are separated. The next measurement is done with beam 1 placed at -2.5Σ and beam 2 placed at -1.5Σ . For the following measurements both beams are moved in steps of 1Σ towards the center of the beam pipe. After 5 measurement steps, when beam 1 reaches 1.5Σ and beam 2 is at 2.5Σ , the beam positions are swapped, and both beams are moved in steps back to the initial position. After this the positions of the beams are swapped again. The last measurement point is taken at head-on position.

After each step of the LSS the same rate in the luminometers should be measured, since the separation of the beams is kept constant. For the y plane LSS this was the case. Neither moving nor swapping of the beams changed the rate in the BCM1F detector, as shown in terms of the instantaneous luminosity in Figure 4.9 on the right. For the head-on starting position the total instantaneous luminosity reached a value of around $2.7 \text{ Hz}/\mu\text{b}$. For each LSS calibration point with 1Σ separation of the beams, the instantaneous luminosity is around $1.5 \text{ Hz}/\mu\text{b}$. The short spikes in the instantaneous luminosity between the LSS points correspond to short periods when the beams were adjusted to head-on position during the optimization for the next LSS measurement point.

During the first LSS in the x plane a drop in luminosity of about 12% and in the second LSS a drop of about 27% were observed when the beams were swapped, as can be seen in Figure 4.10.

To understand the drop in the instantaneous luminosity the following consider-

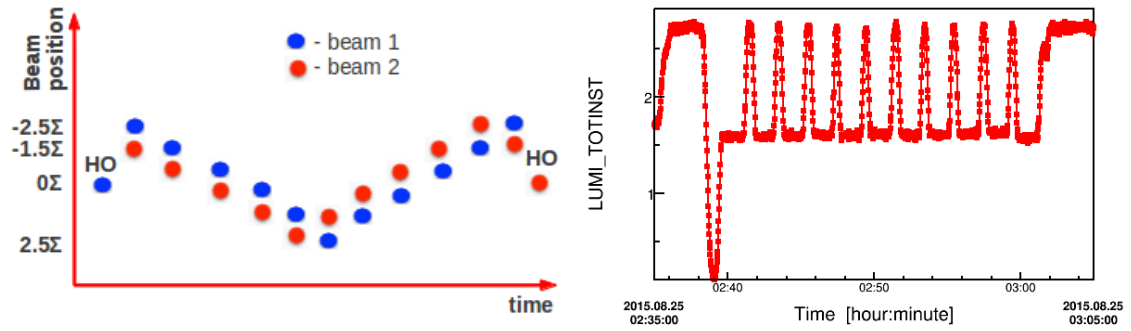


Figure 4.9: Left: Sketch showing the positions of beam 1 and beam 2 during the LSS. Right: The total instantaneous luminosity as a function of time during the LSS in the y plane.

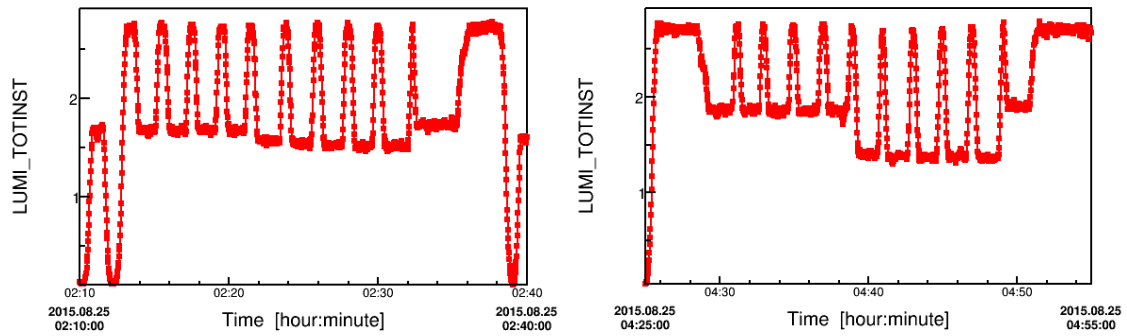


Figure 4.10: The measured total instantaneous luminosity as a function of time. Left for the first LSS in the X plane and right for the second LSS in the X plane.

ation was done. Assuming the particle density in both beams can be described by a Gaussian of width $\sigma = 102 \mu\text{m}$. The convolution of two Gaussian functions G_1 and G_2 with mean values different by a quantity d is written as

$$G_1 \times G_2 = \frac{1}{2\pi(\sigma_1^2 + \sigma_2^2)} \times e^{-\frac{[d - (\mu_1 + \mu_2)]^2}{2(\sigma_1^2 + \sigma_2^2)}}, \quad (4.5)$$

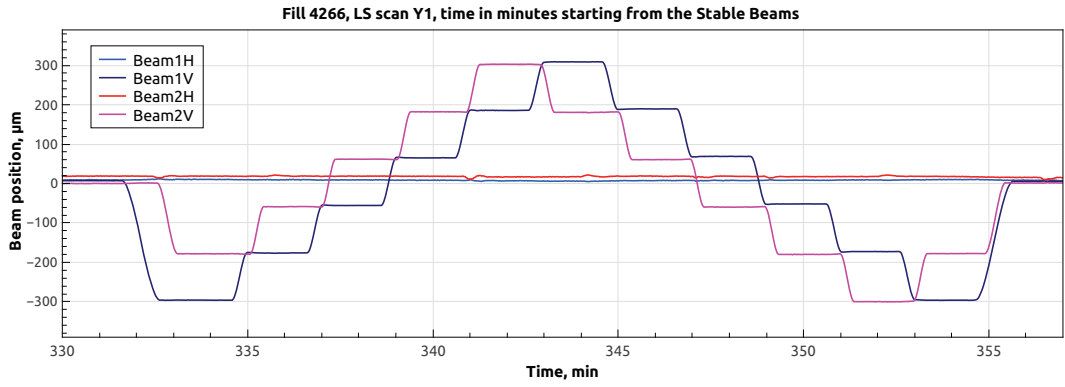
where σ_1 and σ_2 correspond to the beam widths of beam 1 and 2, μ_1 and μ_2 are the positions of the maxima of the Gaussians. Here the beams are assumed to have the same width $\sigma_1 = \sigma_2 = \sigma$ and the maxima of their particle density distributions are positioned at zero, $\mu_1 = \mu_2 = 0$. The head-on position of the beams with zero displacement is taken as the reference value for the luminous region. After the first step of the LSS, the separation of the two beams is 1Σ . The overlap of the beams is calculated to be 50.5% of the value at zero displacement. Taking into account the 27% drop in the luminosity after the beams were swapped, the overlap of the beams becomes 37%. Using the width of the beams of $102 \mu\text{m}$, the separation corresponding to 37% of the zero displacement is $d = -\sqrt{\ln(0.37) \times 4\sigma^2} = 203.4 \mu\text{m}$. From this simple estimation we can conclude that the expected drop in luminosity will be explained by a larger separation of the beams after the swap.

Beam position monitors

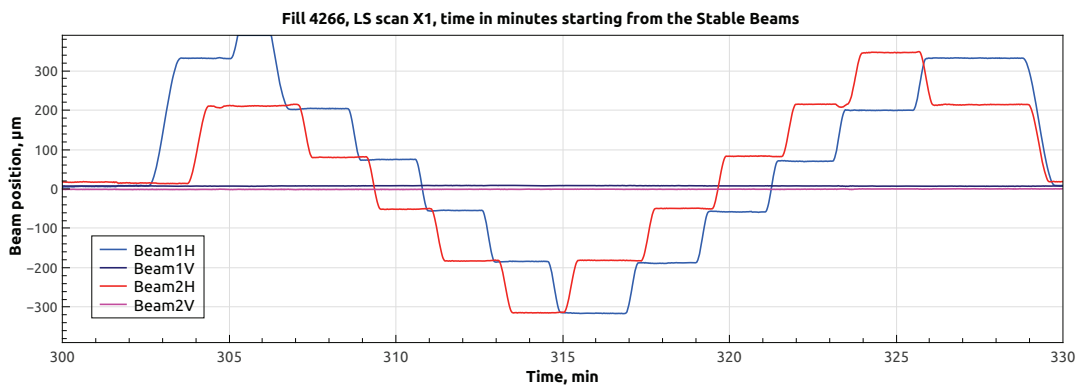
The LHC BPMs [92] were used to measure the horizontal and vertical beam position during the LSS as well as to monitor the orbit drift during the VdM scans (described in more detail in section 4.2.7). The BPMs are installed on both sides an equal distance in z from the IP at the CMS and ATLAS locations. There is no magnet of the final focus system between the BPMs and the IP, so a linear interpolation between the BPMs on both ends is done to obtain the beam position at the IP. The impact of the CMS solenoid can be ignored, since the deflection on the transverse direction is negligible.

After the upgrade during LS1, the BPMs are read out with two different electronics, the regular (RBPMs) and the new more precise DOROS electronics. DOROS is designed to have a position resolution of less than $1 \mu\text{m}$. For each beam DOROS measures the incoming and outgoing position in x and y for each beam. The position at the IP is the middle point of the straight line between the left and right modules from opposite sides from the IP. The coordinate system is the LHC coordinate system, hence the values calculated using DOROS data for the beam positions at the IP are absolute positions. There is a possible parasitic offset originating from a sensitivity to certain orbit configurations. To exclude this effect, it is sufficient just to subtract the readout value in the moment of Stable Beams declaration, identified by a time stamp. At this moment beams were head-on, and any measured offset is a measurement bias. The final beam position measurements for one LSS in the y

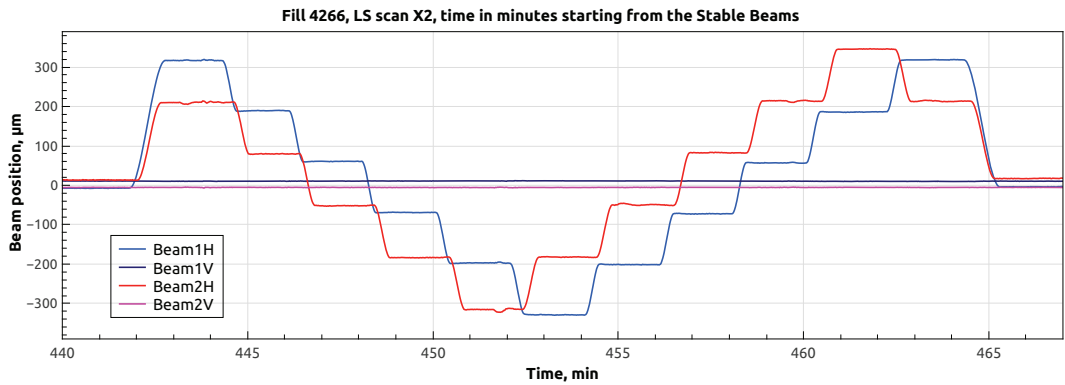
Chapter 4. Measurements of the luminosity using BCM1F



(a)



(b)



(c)

Figure 4.11: Beam position measured by DOROS BPMs as a function of time during the LSS. Beam 1 horizontal and vertical position are shown in light and dark blue and the beam 2 horizontal and vertical position are shown in red and pink, respectively. (a) – LSS in the y plane; (b) – LSS in the x plane, first measurement; (c) – LSS in the x plane, second measurement.

plane and two LSSs in the x plane are shown in Figure 4.11 as a function of time. The values are interpolated to the IP and corrected for offsets.

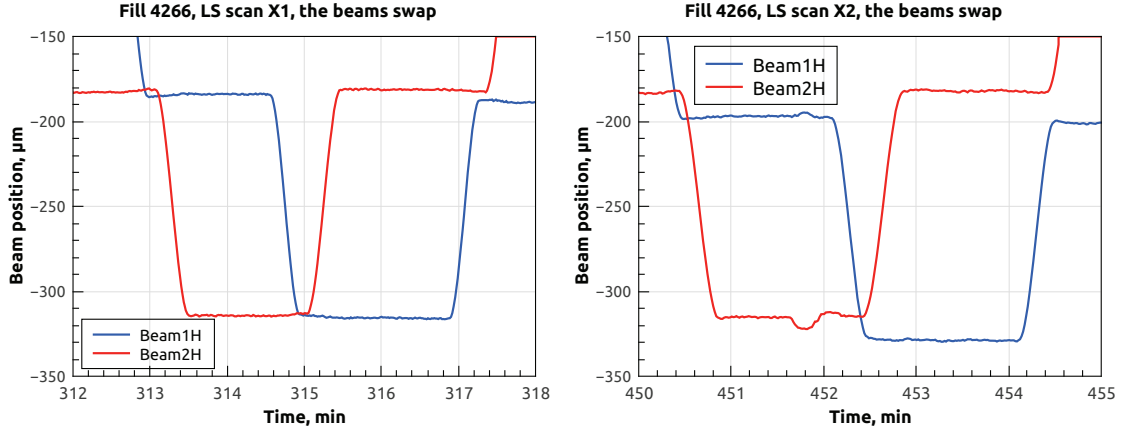


Figure 4.12: DOROS BPM data: beam 1 (blue) and beam 2 (red) positions in the middle of the first (left) and second LSS (right) in the x plane, before and after the beam swap.

Figure 4.12 shows the zoom into a region of Figure 4.11 b) and c) when beams are swapped during the first and second LSS in the x plane, respectively. Whereas the separation in the first scan is only slightly different before and after the swap, it changes in the second scan from about $116 \mu\text{m}$ to $145 \mu\text{m}$. Substituting the measured beam separations into the convolution of the Gaussians in Eq. 4.5 the overlap of the beams was calculated. The ratio of its values before and after the swap is 0.75. Hence, using measurement by the DOROS BPMs a drop of 25% in the luminous region is expected in this scan, being in a good agreement with the observation shown in Figure 4.10. In the first scan in the x plane the measurement by the DOROS BPMs lead to an expected drop of the instantaneous luminosity of 9%, also in reasonable agreement with the value of 12% as observed after the swap in Figure 4.10.

Length Scale correction applied to the 2015 VdM scans

The beam position information obtained from the DOROS BPMs is compared to the beam-spot measurement using the CMS tracker data. The position of the beam-spot is determined from the distribution of the vertices with the highest track multiplicity in each bunch crossing, as is described in more detail in Ref. [93]. Using data from DOROS BPMs shown in Figure 4.11, time intervals of LSS points were defined for beam-spot distributions. The position measurements were performed for 5 values

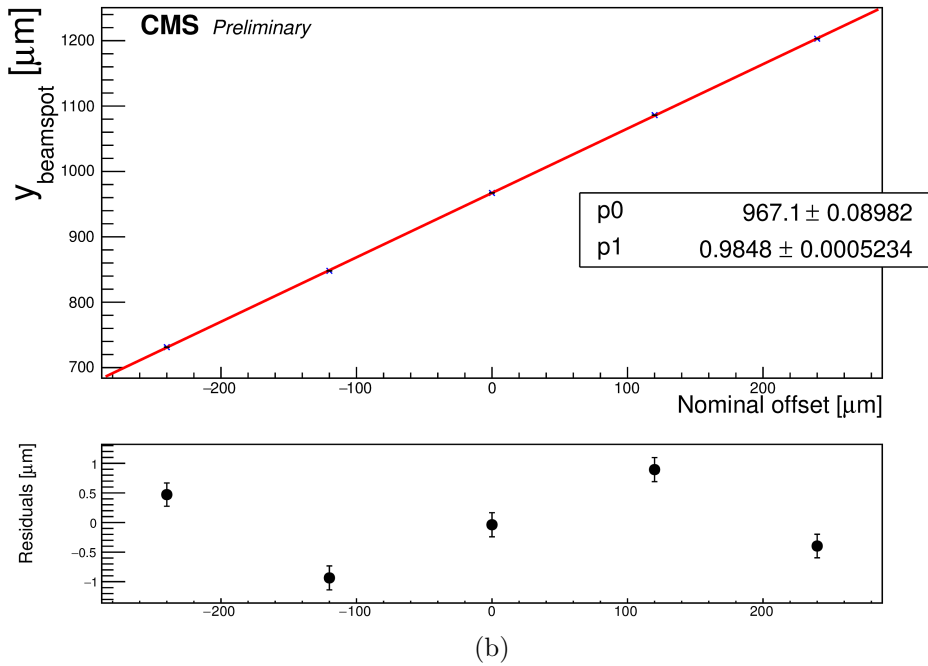
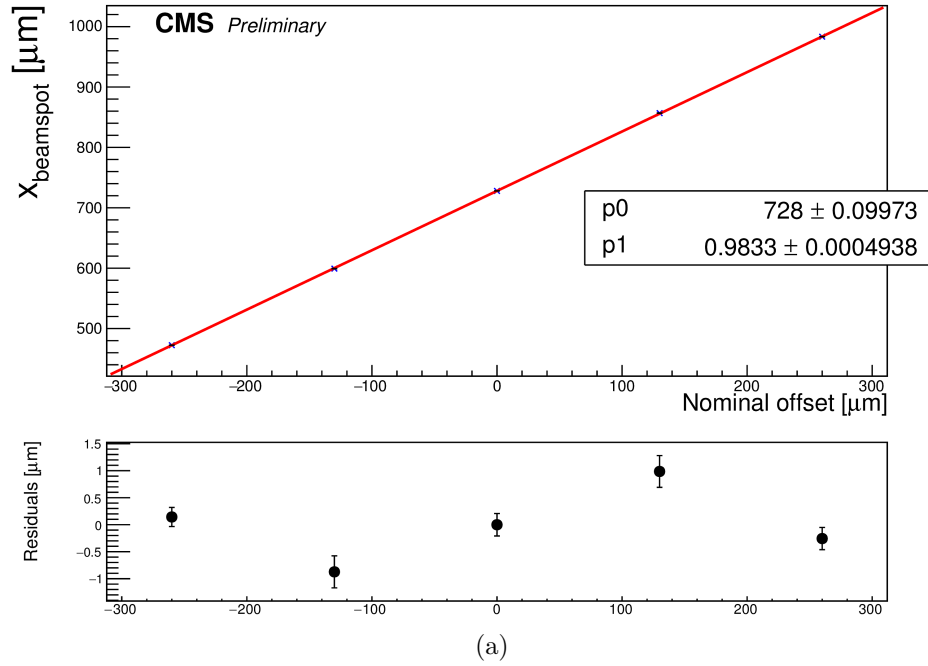


Figure 4.13: The beam-spot position measured using the distribution of vertices obtained from the tracker as a function of the beam position provided by the DOROS BPMs. Also a first order polynomial fit and the residuals are shown. (a) – results for the x plane, (b) – results for the y plane.

before and 5 values after swapping the beams. The beam-spot measurements are distributed as a function of the beam position measured by the DOROS BPMs and fitted with a straight line. Examples of the fits in the x and y planes, together with the residuals, are shown in Figure 4.13. The residuals are calculated as the difference of the beam-spot position and the fit value at each measurement point. The error bars on the residuals are taken as the uncertainty of the beam-spot position. The slope values of the straight line in the y plane and the x plane are 0.985 and 0.983, respectively. The S-shape observed in the residual distributions are seen in all LSSs, and also confirmed by the ATLAS Luminosity group. Hence it is an effect still to be considered.

From the slope values corrections are applied to the measured beam positions obtained from the DOROS BPMs. These corrections reduce the measured horizontal and vertical beam widths by 1.6% and 1.7%, respectively, and the visible cross section by 3.2%. The results of the visible cross section per scan pair with and without these corrections are summarized in Table 4.2. A 1.5% systematic uncertainty is assigned to the visible cross section determination taking into account the length scale correction.

Table 4.2: Visible cross section obtained without correction applied (no corr) and after the length scale correction was applied.

Scan pair	$\sigma_{vis\ no\ corr}$ mean	$error_{no\ corr}$	$\sigma_{vis\ LS}$ mean	$error_{LS}$	$(\sigma_{vis\ no\ corr} / \sigma_{vis\ LS}) - 1$ (%)
1	245.95	0.36	238.15	0.31	3.28
2	247.58	0.35	239.89	0.31	3.21
3	242.75	0.36	235.87	0.37	2.92
4	247.08	0.38	240.05	0.42	2.93
5	247.19	0.36	239.03	0.32	3.41

4.2.7 Orbit drift

The drift of the beam orbit during the VdM scan leads to a shift of the beams. To estimate the impact on the VdM scan parameters, the position of the beams was measured before and after the VdM scan in each plane using DOROS BPM data at several positions in the LHC arcs when the beams are adjusted head-on. Figure 4.14 shows the absolute difference of the beam positions before and after the scan for all scans. For all but one scans the orbit drift in all planes is less than 3 μm . Only for scan 5, which corresponds to the first imaging scan in the x plane, the orbit drift for

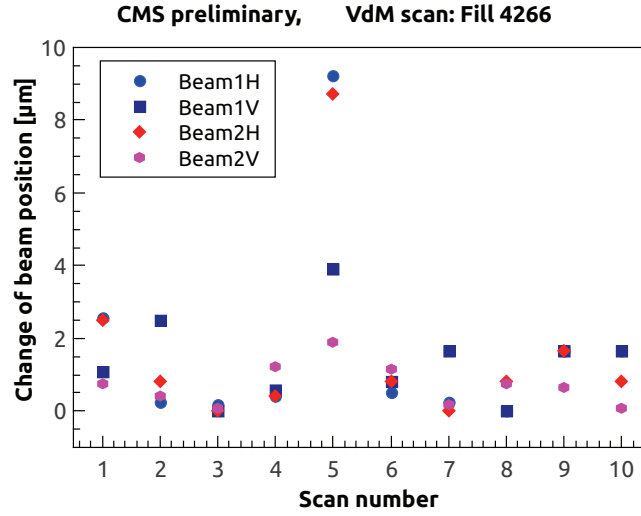


Figure 4.14: Absolute difference of the orbit position before and after each VdM scan versus scan number. DOROS BPMs data is used to obtain vertical and horizontal positions of beam 1 and beam 2.

both beams in the horizontal direction reached about $9 \mu\text{m}$. This scan was excluded from the further analysis.

4.2.8 Correlations between the particle densities in the x and y planes

If the proton density in a bunch exhibits x - y correlations, the VdM scan method is biased, as the obtained beam overlap integral differs from the one for no x - y correlations. In the VdM scan method it is assumed that the proton densities in the two beams, $\rho_1(x, y)$ and $\rho_2(x, y)$, are factorizable in x and y :

$$\rho_i(x, y) = \rho_i(x)\rho_i(y). \quad (4.6)$$

Then the overlap integral reads:

$$O_I = \int_{-\infty}^{\infty} \rho_1(x)\rho_2(x)dx \times \int_{-\infty}^{\infty} \rho_1(y)\rho_2(y)dy. \quad (4.7)$$

In Ref. [94], a method to reconstruct the two-dimensional proton densities in the bunches using vertex distributions accumulated during LHC beam imaging scans is proposed. The study is based on simulations showing that x - y correlations in the beam shapes can lead to an overestimation of the beam overlap of about 9% and to an underestimation of the visible cross section.

This method was applied for LHC imaging scan data to estimate the uncertainty on the luminosity calibration associated to the beam-shape reconstruction due to correlations in the proton density distribution. The reconstructed vertices distributions in the transverse plane of the CMS detector were considered proportional to the proton densities of the two colliding bunches.

$$n^{vtx}(x, y) \propto \rho_1(x, y)\rho_2(x, y), \quad (4.8)$$

where $n^{vtx}(x, y)$ is the number of vertices at a given point (x, y) .

Special beam imaging scans when only one beam is moving in a defined plane allow one to constrain the beam widths separately. In the first scanning beam 1 moves over beam 2 in x and y and then vice versa. The following dependencies will be obtained:

$$\begin{aligned} n_{x,2}^{vtx}(x, y) &\propto \rho_2(x, y)(\mathcal{M}\rho_1(y)), & n_{y,2}^{vtx}(x, y) &\propto \rho_2(x, y)(\mathcal{M}\rho_1(x)), \\ n_{x,1}^{vtx}(x, y) &\propto \rho_1(x, y)(\mathcal{M}\rho_2(y)), & n_{y,1}^{vtx}(x, y) &\propto \rho_1(x, y)(\mathcal{M}\rho_2(x)). \end{aligned} \quad (4.9)$$

Each distribution covers different parts of the underlying proton densities, e.g. $n_{x,2}^{vtx}(x, y)$ only depends on beam 2 in x and has x - y correlations only if there are x - y correlations in the proton density of beam 2, whereas $n_{x,2}^{vtx}(x, y)$ and $n_{y,2}^{vtx}(x, y)$ fully constrain the proton density distribution of beam 2.

The full two-dimensional proton densities of two colliding bunches are estimated from a simultaneous fit of the vertices distributions of four imaging scans, assuming analytic models for $\rho_1(x, y)$ and $\rho_2(x, y)$.

Also proton densities from the beam imaging scans were used to simulate the VdM scans and estimate the overlap regions. Comparing measured overlaps and expected ones from the simulations the overall correction for the visible cross section is 1.1%. A systematic uncertainty of 1.5% is conservatively assigned to account for correlations between the particle densities in the x and y planes [95].

4.2.9 Beam-beam effects

As proton-proton beams contain particles of the same charge, particles are deflected when bunches cross. The result is a bias in the separation of the two beams. The amount of the deflection depends on the separation of the beams. The bias is calculated as described in Refs. [40, 96] and applied as a correction to the beam separation value. An example of the correction as a function of the nominal separation for one bunch crossing is shown in Figure 4.15.

Another beam-beam effect is called the dynamic beta effect. It describes the defocusing of the beams when bunches cross. Both beam-beam effects scale with

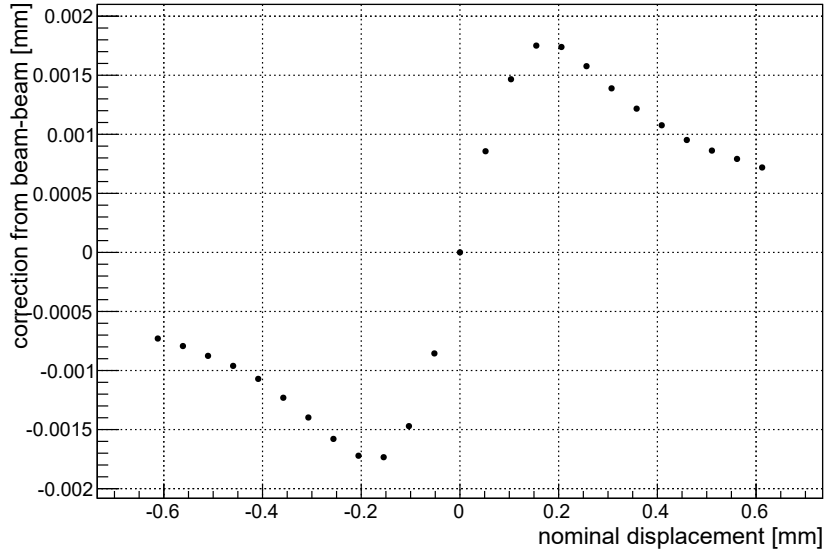


Figure 4.15: An example of the impact of the beam-beam deflection on proton-proton collisions in one bunch crossing.

the linear beam-beam parameter:

$$\xi_{x/y} = \frac{r_p N \beta_{x/y}^*}{2\pi\gamma\sigma_{x/y}(\sigma_x + \sigma_y)}, \quad (4.10)$$

where r_p is the classical proton radius, N is the number of particles in the bunch, β^* is beam optics settings, γ is the relativistic factor and σ_x and σ_y are the beam widths at the IP.

The visible cross sections extracted before and after applying the correction are summarized in the Table 4.3. With the correction applied higher visible cross section values were obtained. The correction to account for the beam-beam deflection was estimated to be about 1.77% for the four scan pairs considered. In comparison to the VdM scan in November 2013, which was done for a beam energy of 4 TeV [96], the value of the current correction is about 60% smaller. The uncertainty of this estimate is dominated by the uncertainty on β^* , set during the VdM scan to 1917 cm. Taking conservatively 20% uncertainty and varying β^* by $\pm 20\%$, the uncertainty of beam-beam correction was estimated to be 0.36%.

The dynamic beta effect is expected to be smaller, but as no correction is applied it is taken into account by assigning a systematic error of 0.5% [95]. The total systematic uncertainty due to beam-beam effects amounts to 0.62%.

Table 4.3: The visible cross section weighted mean value without corrections applied (no corr) and with beam-beam correction applied (BB).

Scan pair	$\sigma_{vis\ no\ corr}$ mean	$error_{no\ corr}$	$\sigma_{vis\ BB}$ mean	$error_{BB}$	$1 - (\sigma_{vis\ no\ corr} / \sigma_{vis\ BB})$ (%)
1	245.95	0.36	250.35	0.35	1.76
2	247.58	0.35	252.58	0.36	1.98
3	242.75	0.36	247.14	0.33	1.78
4	247.08	0.38	251.51	0.36	1.76
5	247.19	0.36	251.67	0.34	1.78

4.3 Stability of BCM1F over the 50 ns running period and systematic uncertainties

4.3.1 Relative channel-to-channel stability

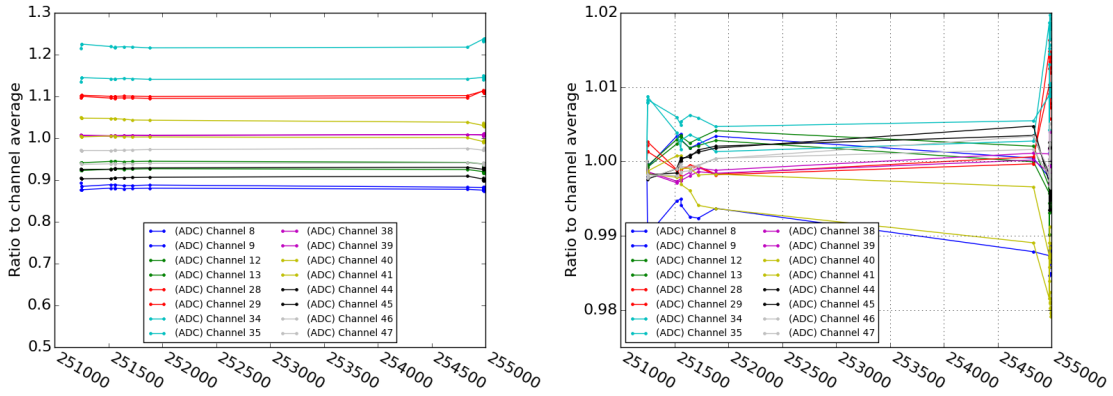


Figure 4.16: Left: The ratio of rates of individual channels to the average rate for each run in the 50 ns operation period plus the VdM scan. Right: the same quantity normalized to one at the beginning of the first run [75].

To test the relative stability and the performance of each channel over the 50 ns running period, the RHU rates were compared to each other. For each run with stable beams in the 50 ns running period plus Fill 4266, the van der Meer scan, the overall rates of all the unmasked channels were averaged. The ratios of the rate of each channel to the average are shown in Figure 4.16 on the left side as a function

of the run number. They vary up to 2% around the average value. This effect has no strong influence on the overall stability, as is shown in Figure 4.16 on the right. The curves were shifted in the first run to unity. All ratios stay within 2% in the 50-ns running period and the time of the VdM scan.

The stability and performance of the BCM1F monitoring using the VME ADC system were discussed in detail in subsection 3.8.1. The relative reduction of the MPV of the signal amplitude distribution during the 50 ns running period was estimated to affect the count rates by not more than 2% as now confirmed from the RHU rates. The shift of the MPVs towards lower values was still far from the threshold. No correction for the inefficiency caused by radiation damage of sensors or electronics was applied for this period, but a 2% uncertainty was assigned.

4.3.2 Systematic uncertainties of the luminosity measurements

The BCM1F detector was calibrated as a luminometer using VdM scans. Multiple beam effects and uncertainty sources, affecting the visible cross section were discussed before. As the uncertainty of the visible cross section directly translated to the uncertainty of the delivered luminosity, a summary of the systematic uncertainties is presented in the Table 4.4. These uncertainties are grouped into uncertainties originating from machine parameters and uncertainties originating from the stability of the BCM1F rate measurements over time. The systematic uncertainty of the luminosity measurement, computing all sources, amounts to 3.1%. This value was then used to quote the uncertainty of the cross section measurement using data from this running period.

4.4 Luminosity measurements using a single channel

During the 25 ns operation of the LHC several channels showed an erratically high count rate or triggered the trip of the power supply. These channels had to be masked from the online luminosity measurements, but some of them were used during VdM scan and hence included in the measurement of the visible cross section. Including or excluding channels from online luminosity calculation during the data taking would introduce a bias in the published luminosity value. This issue caused the need to study the measurement of the visible cross section using each channel separately as an option for 2016. In this case channels could be included or excluded from the online publication without a need in any additional correction.

Table 4.4: Systematic uncertainties of the luminosity measurements with BCM1F detector in 50 ns period.

Systematic	correction [%]	uncertainty [%]
Detector effects		
Stability	-	2
CMS downtime	-	0.5
Machine effects		
XY-Correlations	1.1 (↑)	1.5
Length scale	3.2 (↓)	1.5
Dynamic- β	-	0.5
Beam-beam deflection	1.8 (↑)	0.4
Orbit Drift	-	0.4
Beam current calibration	-	0.3
Ghosts and satellites	-	0.2
Total		3.1

4.4.1 Validation of the aggregated histogram

An example of raw RHU data for one bunch crossing for channel 41 was shown in Figure 3.5 on the right. To build this particular plot the data was accumulated within 2 hours during stable beams of the VdM scan fill. Raw RHU data is processed in different ways for the online luminosity publication and for monitoring or offline analysis. For the online luminosity measurement only the third RHU bin from the 4 bins corresponding to one bunch crossing is used. But the rates from channels are averaged and the per-channel information is not available in this data. However, the aggregated histogram can be used for the offline per-channel analysis. The bin width is 25 ns, summing up 4 bins of raw RHU data.

The aggregated histogram contains, in addition to hits from collision products, also hits from machine induced background and afterglow. The difference between the count rate stored in the luminosity bin (third bin) and in the aggregated histograms rate (sum of 4 bins) was estimated from Figure 3.5 to be about 10%. This difference is also expected to show up in the visible cross section calculated using luminosity histograms and aggregated histograms.

The validation of the aggregated histogram means the comparison of the cross section values obtained from the luminosity histogram and from the aggregated histogram using the same channels which were included in the average for online luminosity calculation. These are channels 8-9, 12-13, 28-29, 34-35, 38-39, 40-41, 45-

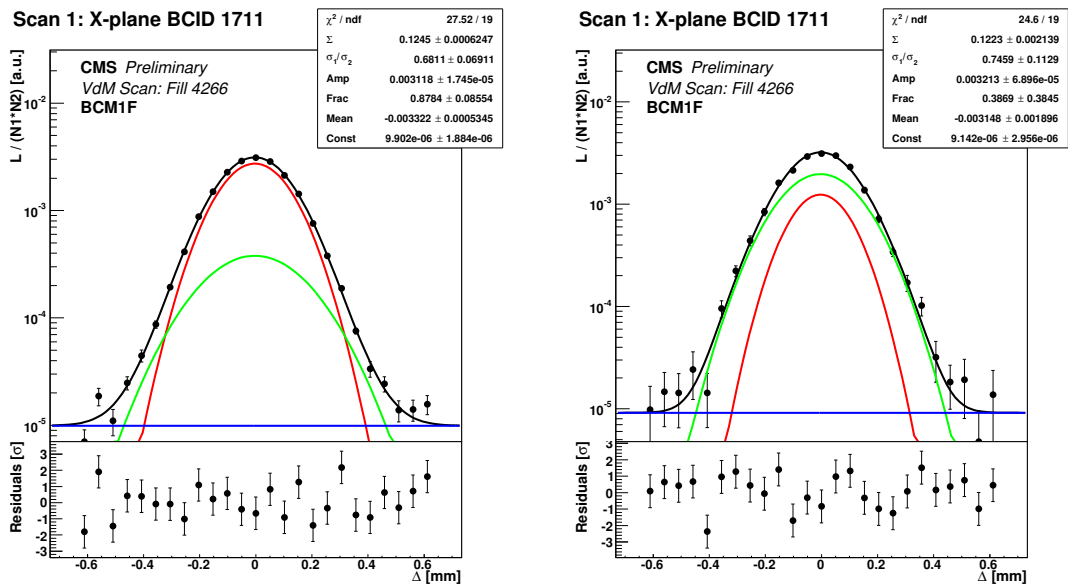


Figure 4.17: Rates obtained from aggregated histogram of the bunch 1711 as a function of the displacement in the x plane (black dots). Two Gaussians are shown in red and green, the constant term in blue and the sum of all in black. Also given are the residuals of the fit. Left: average of all channels used during VdM scan, right: data from channel 40.

45, 46-47. For each aggregated histogram the same data processing as the BCM1F processor does for the online luminosity calculation was performed. The hit rate was recalculated over four lumi-nibbles using the zero counting algorithm. Then the per-channel sum of the histograms within a defined time windows was calculated and for the unmasked channels an averaged value was determined.

The produced file is a new input for fitting in the VdM analysis framework. Keeping the same settings of the framework a superposition of two Gaussians and a constant background was used to fit the luminosity as a function of the displacement for each bunch crossing and the parameters for the visible cross section calculation were extracted from the fit. Just for illustration, a fit of a VdM scan in the x plane for one BCID using aggregated histogram is shown in Figure 4.17. The rates as a function of the displacement obtained using luminosity histograms and aggregated histograms look similar (Figure 4.5 and Figure 4.17, respectively). As expected from the difference in the data files, the constant background contribution in the latter fit is about two times higher, explained by more machine induced background and afterglow contributions store in additional 3 RHU bins of the aggregated histograms. Also the collision products leaking to the neighbors of the luminosity bin affect rates obtained from the aggregated histograms and therefore the σ_{vis} . In Figure 4.18 on the left the values obtained for σ_{vis} using aggregated histograms data (black dots) is about 13% higher than the one obtained from online luminosity data (red dots).

As scans in both planes are used to define one visible cross section, the color code in χ^2/NDF plot shown in Figure 4.18 on the right is kept to match the visible cross section comparison plot, shown in Figure 4.18 on the left. The red dots correspond to the online luminosity histograms and the black dots to the aggregated histogram data averaged over all unmasked channels. The χ^2/NDF values for fits of the scan in x and y planes are presented as dots and squares, respectively. The fit quality remain the same for both data types used with an average χ^2/NDF about 1.5. Precise values can be found in the top part of the Table 4.5.

4.4.2 Visible cross section for single channel

Using aggregated histogram data, the VdM scan analysis is done for single channel. As in the previous subsection, the hit rate was recalculated into an average number of hits per turn, μ , over four lumi-nibbles using the zero counting algorithm. Then the per-channel sum of the histograms within a defined time windows for each point of the VdM scan was calculated. The files obtained for each channel were used as an input for the VdM analysis framework to calculate the visible cross sections. An example of the fit for one BCID is shown in Figure 4.17 on the right. The statistical uncertainty shown especially on the tails of the distribution are larger than for the same bunch with rates averaged from all unmasked channels, but this does not affect the fit quality. The visible cross sections determined for several channels are

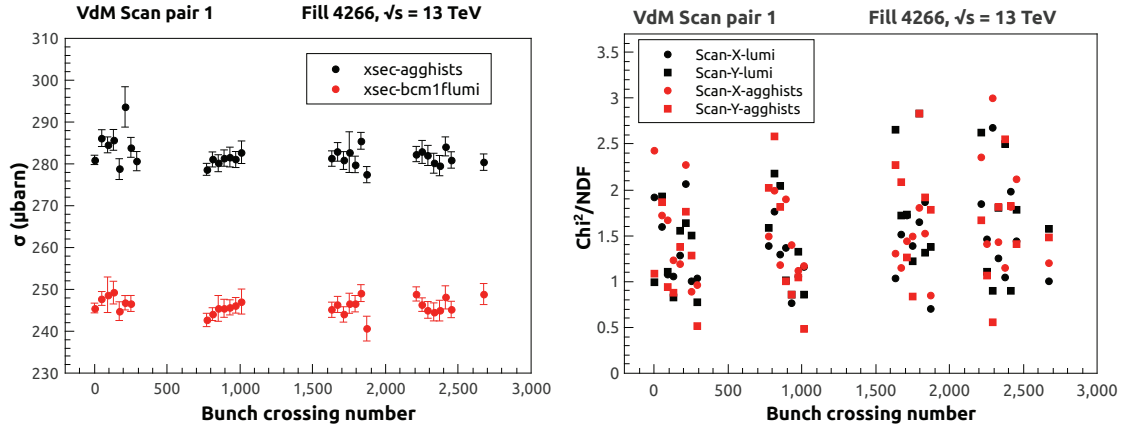


Figure 4.18: Left: The visible cross section as a function of the BCID for VdM Scan pair 1 with all unmasked channels in the average. Red points: the visible cross section was calculated using the online luminosity data; black points: the visible cross section was calculated using the aggregated histogram data averaged over all unmasked channels. Right: χ^2/NDF , showing the fit quality of the measured rates as a function of the displacement in x and y plane. The color code is kept as on the left.

Table 4.5: Average visible cross section values and their uncertainties obtained using different data sources and different channels together with corresponding χ^2/NDF of the fit in x and y planes. There were no corrections applied at this stage.

Data source	$\sigma_{vis}, (\mu barn)$	std. σ_{vis}	X scan χ^2/NDF	Y scan χ^2/NDF
All Unmasked Channels Average				
lumi data	246.11	1.92	1.42	1.55
agghists	282.14	2.98	1.56	1.50
One Channel				
agghists ch40	281.78	7.04	1.33	1.09
agghists ch41	286.07	4.12	1.14	1.05
agghists ch44	257.99	5.07	1.12	1.30
agghists ch45	253.73	4.71	1.12	1.18

presented in Figure 4.19 on the left and χ^2/NDF for fits of the scan in x and y plane on the right. Channels 40-41 and 44-45 correspond to the two pads at one diamond sensor. Precise values of the visible cross section and χ^2/NDF are summarized in the bottom part of Table 4.5. From this we can conclude that each channel can be used separately, but the standard deviation is larger than for the average of the luminosity channels.

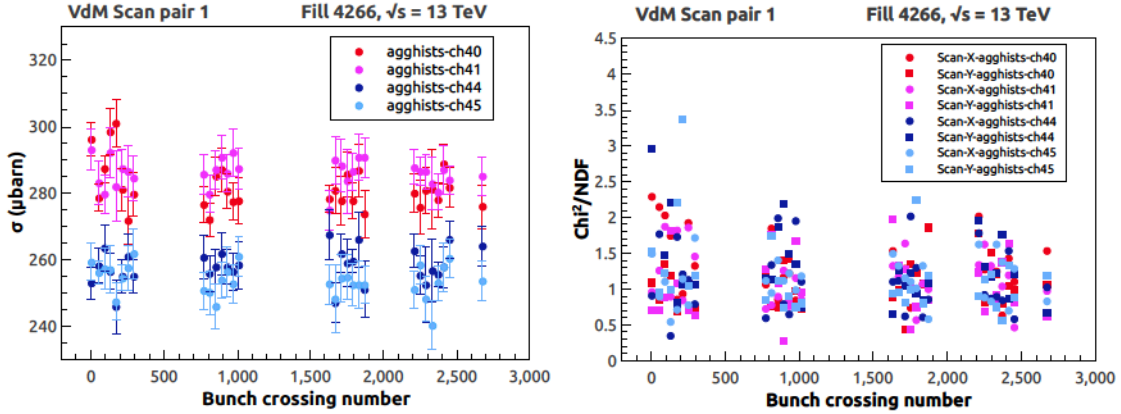


Figure 4.19: Left: The visible cross section as a function of the BCID for VdM Scan pair 1 obtained for channel 40, 41, 44 and 45 using the aggregated histograms. Right: χ^2/NDF , showing the fit quality of the measured rates as a function of the displacement in x and y plane.

The visible cross section measured by channels corresponding to the same diamond sensor are in good agreement. However, the visible cross section obtained from different diamond sensors differs by 9.86%. This difference is explained by the rate difference measured by these channels. The rate difference is estimated to be around 9.70% from aggregated histograms accumulated during 30 min of stable beams in the relevant VdM scan in Fill 4266.

4.5 Comparison of VdM scans in 2015 and 2016

The CMS VdM scan program 2016 was very similar to the one in 2015, described in detail in subsection 4.2. Two standard scan pairs with 25 measurement points, 2 imaging scan pairs with 19 points per scan, the length scale calibration and the reproducibility scan were done. There were 32 colliding bunches in the LHC grouped in four bunch trains. The first attempt to complete the VdM program took place on the 19th of May during Fill 4945 and was interrupted after the first two scan pairs

were completed due to a beam dump. The full VdM scan program was done in Fill 4954 on the 27th of May. All completed scans from both fills were used for analysis. An example of the online luminosity published on the BRIL web monitoring page during all scans in Fill 4954 of the VdM program 2016 is shown in Figure 4.20. Different luminometers data is published in different colors.

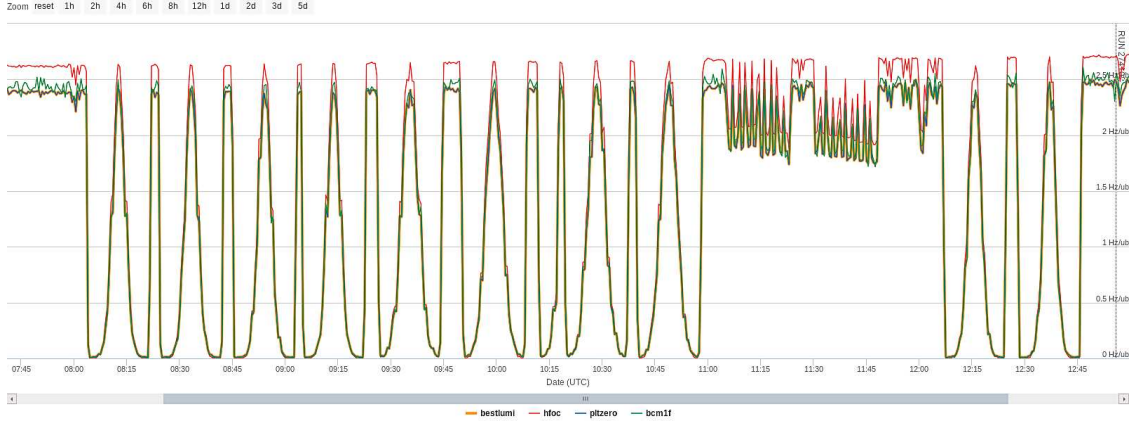


Figure 4.20: Online luminosity measured by all CMS luminometers as a function of time during the VdM program 2016, Fill 4954, web monitoring tool. HF online luminosity in red, PLT in blue and BCM1F in green.

The average visible cross section obtained from two scans of Fill 4945 and four validated scans of Fill 4954 were $(215.37 \pm 2.44) \mu b$ and $(212.63 \pm 3.02) \mu b$, respectively, resulting in a 1.3% difference. For the moment of calibration in 2016 there were four BCM1F channels included in the luminosity measurement. As the measured rate of those channels was different and there was a risk of one of the channels to trip, the visible cross section was delivered for each channel separately based on the Scan pair 1 of Fill 4945.

The aggregated histograms described in subsection 4.1 were also saved in 2016, but in addition also for the third RHU bin for each channel. To distinguish the aggregated histograms for the lumi-bin and sum of four bins, an algorithm identification (alogoID) was introduced [75]. It was equal to 1 for the sum of four bins and 2 for histograms with only the lumi-bin saved. Data of the latter one was used in 2016 for visible cross section analysis for single channel. The results are shown in Figure 4.21 and summarized in Table 4.6. In the last column of the table the ratio of the visible cross section measured in 2015 and 2016 VdM scans is given. As different data processing was applied to data in 2015 and 2016, non-lumi-bins contribution in 2015 data had to be taken into account. It was shown in subsection 4.4.1, that the contribution of the non-lumi-bins is about 10%. Therefore from the visible cross

section values taken from the Table 4.5 10% were subtracted before calculation of the ratio to the value obtained in 2016 VdM scan.

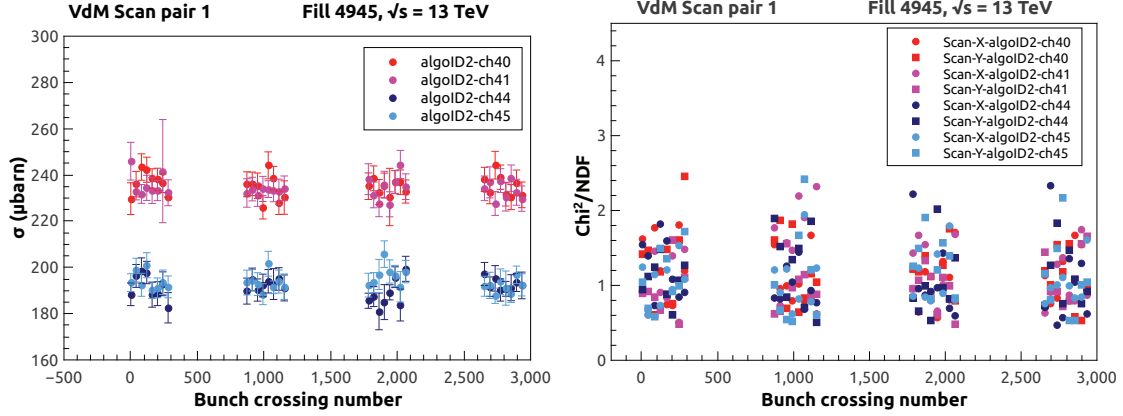


Figure 4.21: Left: The visible cross section as a function of the BCID for VdM 2016 Fill 4945 Scan pair 1 for channels 40, 41, 44 and 45. Only the luminosity bin contents were used. Right: χ^2/NDF , showing the fit quality of the measured rates as a function of the displacement in the x and y planes per-channel.

Table 4.6: The average σ_{vis} values obtained in the VdM scan in 2016 for different BCM1F channels together with corresponding χ^2/NDF of the fit in the x and y planes. In the last column the ratio of the visible cross section in the 2015 and 2016 VdM scans is given.

Data source (agghists)	σ_{vis} mean (μbarn)	std. σ_{vis} (μbarn)	X scan χ^2/NDF	Y scan χ^2/NDF	Ratio σ_{vis} 2016/2015
channel 40	235.11	4.54	1.11	1.21	0.93
channel 41	233.54	4.05	1.23	1.00	0.91
channel 44	190.71	4.45	1.09	1.12	0.82
channel 45	193.44	4.39	1.07	1.15	0.85

The visible cross sections obtained in 2016 are about 8% lower for channels 40-41 and about 13% lower for channel 44-45 in comparison to the results in 2015. The average χ^2/NDF for all scans remain about 1.1. The channels 40-41 and 44-45, corresponding to the same diamond sensor, showed almost equal visible cross sections.

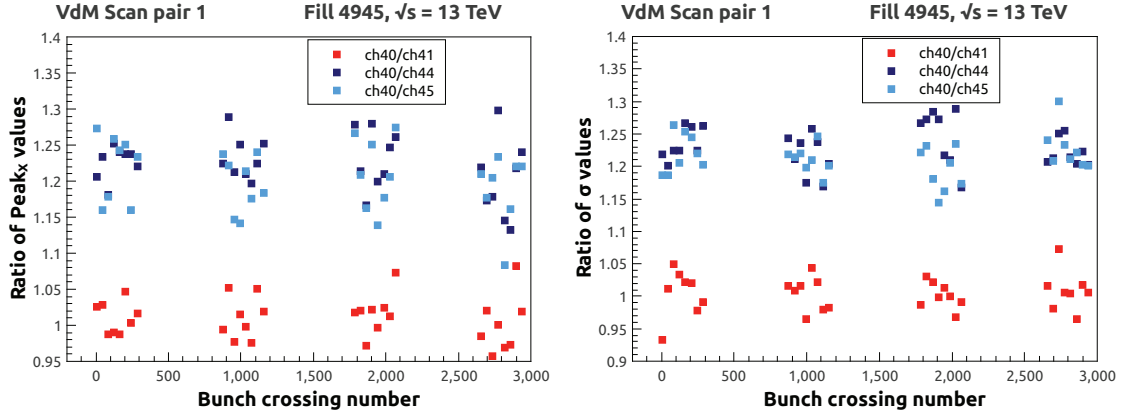


Figure 4.22: Left: Ratios of $Peak_x$ values for different BCM1F luminosity channels as a function of the BCID for VdM Scan pair 1, Fill 4945. Right: Ratios of the visible cross sections values of the same channels as a function of the BCID.

The ratio of the $Peak_x$ values obtained for different channels and also the ratio of the visible cross section values are shown in Figure 4.22. $Peak_x$ values correspond to the maximum of the measured rate. As the ratio of the $Peak_x$ values is directly reflected in the ratio of the visible cross section, we concluded that the changes in the ratio of the σ_{vis} are due to changes in the measured rates. The ratios of $Peak_x$ and the visible cross section for channel 40 to channel 41 are scattered around 1, as those channels correspond to the same diamond sensor and show similar count rates. Taking channel 40 as a reference, ratios of $Peak_x$ values to the ones measured in channel 44 and 45 were calculated. The ratios for channel 40 to channel 44 and channel 40 to channel 45 are scattered around 1.25. A similar value of the ratio was found for $Peak_y$ values and visible cross sections of these channels.

4.6 Comparison of the luminometers

As was described in Chapter 2, there are three online luminometers used at CMS and also the pixel detector used for the offline studies. The BCM1F and HF luminosity measurements are based on the zero counting algorithm. The PLT uses the rate of threefold coincidences of hits in the telescopes and the silicon pixel detector the pixel cluster counting. Because of the different locations and the employed luminosity measurement methods, the measured count rates are different.

The value as σ_{vis} has to be measured for each individual luminometer. Thanks to the central XDAQ system, data from all online luminometers is stored in the same format and can be processed in the common way.

The fitting procedure is similar. As an example the measured rates as a function of displacement for BCID 81 during imaging VdM scan Fill 4937 together with the fit are shown in Figure 4.23 for the PLT and HF. The superposition of two Gaussians with different widths and a constant term was used to fit the data.

The difference of the measured rates between PLT and HF reaches almost one order of magnitude. However, the obtained values for Σ_x and Σ_y , the effective beam widths, should be the same for all luminometers. Σ_x and Σ_y values obtained for all luminometers in the imaging VdM scans of the Fill 4937 in x and y plane are shown in Figure 4.24. BCM1F measurements agree with the other subdetectors. The average value calculated over the full orbit agrees within less than 1% with the PLT and HF and within 2% with the PCC.

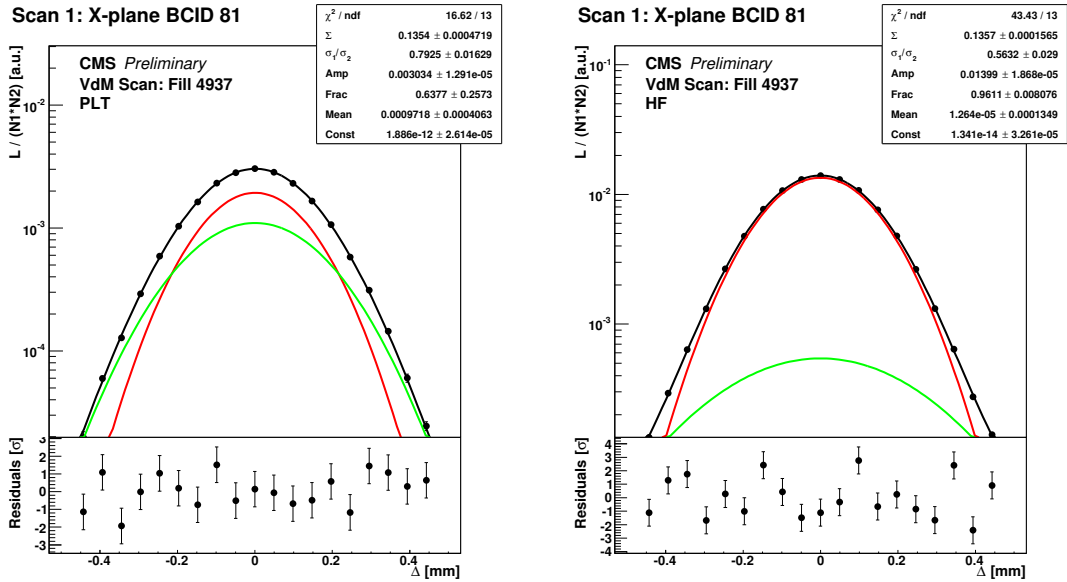


Figure 4.23: Rates as a function of the displacement during VdM imaging scan BCID 81 of the Fill 4937 in the x plane with resulting fit shown in black. Two Gaussian fits are shown in red and green. The constant term is too small and not seen on the plots. Also given are the residuals of the fit. Left: PLT, right: HF.

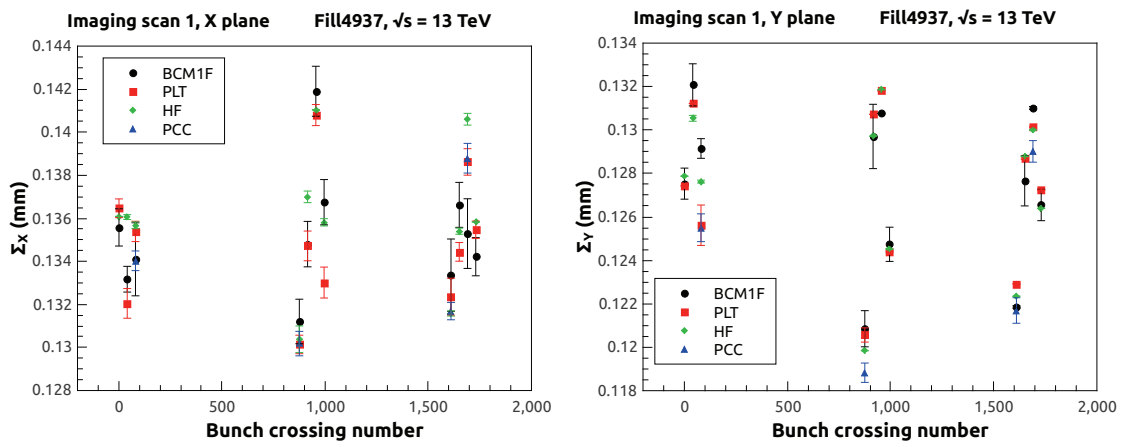


Figure 4.24: Comparison of Σ_x and Σ_y values for all luminometers as a function of bunch crossing number. Left: Fill 4937 imaging VdM scan pair 1 in x plane, right: in y plane.

Chapter 5

Upgrade of the luminometers for high luminosity LHC

There are numerous detectors which have been developed for applications in collider physics and particle physics in general. For applications with extremely high radiation doses novel detector technologies need to be developed. Solid state detectors, in comparison to gaseous or liquid detectors, have a smaller size and better fulfill the requirements for instrumentation near the beam pipe. Examples of solid state detectors applications are beam halo and beam loss monitors at the Large Hadron Collider, FLASH or XFEL [49–54, 97]. Currently silicon and artificial diamond sensors are widely used. Diamond sensors are expensive and of small size, silicon requires cooling which is not beneficial in the limited space available for instrumentation close to the beam pipe.

Single crystal sapphire sensors are considered as a promising alternative. Industrially grown sapphire wafers are available in large sizes, are of low cost like silicon and can be operated without cooling like diamond sensors. Basic characteristics, like leakage and signal current, radiation hardness, charge collection efficiency of sapphire sensors are discussed in this chapter. Also a design of a sapphire detector stack is described and the results of its performances measured in a test beam are presented. The dependence of the CCE on the applied voltage and position-resolved sensor response are studied and compared to a model of the charge transport in the presence of polarization.

5.1 Artificial Sapphire

Sapphire is a crystal of aluminum oxide, Al_2O_3 . Natural sapphire and ruby are found all over the world, with notable sources in Africa, Asia, Australia, North America, and Europe [98].

Sapphire saw its first industrial application more than 300 years ago, as jewel bearings in mechanical timepieces, where longevity and high accuracy were worth the cost of these durable and low-friction components. The first grown synthetic ruby in the 1880s and the beginning of manufacture in 1900 made rubies/sapphires beneficial for many industrial applications. In this section the invention of artificial sapphire, different growing techniques, basic characteristics and applications of sapphire will be described.

5.1.1 Historical excurs

Since J. L. Gay-Lussac in 1817 discovered a way to produce pure aluminum oxide by thermal decomposition of ammonium alum, it remains as the raw material for making sapphire up to our days. In 1840 H. Rose made a chemical analysis of sapphire. With knowledge of the true composition of sapphire, work to grow sapphire crystals began in many chemical laboratories. None of the tries of numerous scientists were successful. Up to the 1870s they were able to produce only microscopic crystals. But in 1877 Edmond Fremy and his assistant Charles Feil published a paper, declaring, that they were able to produce small, clear, red ruby crystals. After Feil died in 1876, Fremy continued to work with his new assistant Auguste V. L. Verneuil. They were able to grow clear ruby crystals from alumina in a potassium hydroxide/barium fluoride flux in a ceramic crucible at 1500° C. Crystals reached up to 3 mm in diameter and 0.3 carat in mass (1 carat = 0.2 grams), but attempts to grow bigger crystals failed [99].

Detailed investigation of the rubies appeared in Geneva in 1885 from an unknown source, showing a content of microscopic gas bubbles. It was pointing to a high-temperature synthetic process. Using this new information, his experience in the field of ruby crystal growing and first experiments with G. A. Terreil on fusion of alumina powder with chromium salt, Verneuil worked to develop flame fusion growth of ruby. He described his success and made a patent, and a sealed document at the Academy of Science was deposited in 1891-1892. In 1902, Verneuil announced his development of a flame fusion process for making ruby and published full details in 1904 [100].

As is described in Verneuil's U.S. patent, base of the method is feed of the aluminum oxide powder and a correct regulation of the flame heat. As a base powder mixture of the oxides was produced: the ammonium aluminum sulfate and ammonium chromium sulfate were each recrystallized 4-5 times and a mixture of the two was calcined at $1000-1200^{\circ}$ C to give a mixture of the oxides. Powder falling through the flame burned inside of the ceramic muffle was heated just below its melting point. Landing on the pedestal inside of the ceramic muffle powder was forming a cone. The upper tip of it became molten when the cone got sharp enough and fresh powder was landing on the molten ball it also melted enlarging

the crystal. Only a thin layer on top of the growing crystal was staying melted. Crystal was growing in a vertical direction approaching the flame. To maintain the needed conditions, the pedestals of the ceramic muffle could be lowered and flow of oxygen could be regulated to control the temperature. The described method allowed during 2 hours of growing to produce a 15 carat cylinder with a diameter of 6 mm and length of 25 mm. Modern flame fusion grown synthetic sapphire crystals, as-grown (left) and during growth in the furnace (right) are shown in Figure 5.1 [98].



Figure 5.1: These photos show flame-fusion synthetic sapphire crystals, as-grown (left) and during growth in the furnace (right). Courtesy of Hrand Djvahirdjian, SA [101].

In 1909-1911 Verneuil was working in Paris to grow blue sapphire for the New York jewelry company. He found that natural blue sapphire always contained both iron and titanium and successfully produced blue sapphire.

Ruby and sapphire manufacturing by the Verneuil process had begun in 1900 in Europe prior to Verneuil's publication of 1904. It was developing fast and there were about 100 Verneuil torches operating in 1920.

In the 1930s in the Soviet Union, S. K. Popov was working to improve the Verneuil method. By 1938 he produced successfully a semi-automatic growth apparatus. Grown by his technique long thin sapphire rods opened a new application for sapphire, as jewels for watches and instruments and as a durable fiber guide in the textile industry. Improved technology increased also crystal quality produced in the U.S.S.R. Later, in the 1950s Popov also devised equipment for bending corundum rods into shapes.

After the invention of the ruby laser in the the 1960s, the required quality of



Figure 5.2: A Czochralski-grown synthetic ruby crystal is shown alongside a fabricated piece (left), and during removal from the growth station (right). Photos by Jennifer Stone-Sundberg [101].

sapphire increased and new methods of growing pure sapphire crystals were developed, as the Czochralski method. In this process, alumina is melted in an iridium crucible in an atmosphere of 98% N_2 / 2% O_2 . A seed crystal is then dipped into the liquid. The seed is rotated and pulled out of the melt. The alumina from the melt crystallizes onto the seed. The diameter of the boule is regulated via rotating and withdrawn rate. The withdrawn rate is usually between 6 and 25 mm/h while rotating at a rate up to 30 rotations per minute. This technique is still very significant today for sapphire production and a wide variety of other crystalline materials (including silicon) because it can produce some of the highest-quality crystals in terms of both purity and defects [101]. Examples of Czochralski-grown synthetic ruby crystal together with a fabricated piece (left), and during removal from the

growth station (right) are shown in Figure 5.2.

Two main methods for growing differently shaped sapphire tubes were developed in the 1960s: edge-defined film-fed growth by H. LaBelle in the U.S. and the related Stepanov method in the U.S.S.R. This flexibility highly increased applications of sapphire in different fields. Details of production and also other methods of sapphire crystal growing, such as the heat exchanging method developed in the U.S. and gradient solidification introduced in Israel and others are described in detail in [99, 101].

The world leaders of sapphire production today are the United States and Russia. For example, the largest crack-free sapphire crystal boules are produced by ARC Energy. Weighing in at 300 *kg*, the cylindrical portion of the crystals measure 500 *mm* in diameter and 340 *mm* in height. Development of mass production reduced costs of the crystal and opened new horizons of possible applications [102].

5.1.2 Basic features of artificial sapphire and industrial applications

Sapphire (Al_2O_3) is stable up to its melting temperature of 2050° C. Its hardness of 9 on the Mohs mineral scale is second only to that of diamond [99]. When no impurities giving it color are present, sapphire can make a wonderful optical window material since it is transparent throughout the entire visible range, and far into the UV and IR ranges as well [98].

Sapphire withstands high temperature, rapid heating and cooling, high pressure, and resists chemical corrosion. High crystal perfection, low reactivity, and appropriate lattice unit cell size make sapphire an excellent substrate in the semiconductor industry for epitaxial silicon growing, blue light-emitting diodes production and diode lasers. Sapphires and rubies are widely employed as jewel bearings in precision mechanical instruments [99].

Because of excellent lattice match of the crystals, silicon can be grown directly on thin sapphire wafer. These days sapphire is widely used as a standard substitute for epitaxial growing of silicon. Computer and smartphone chips are grown on sapphire, where its thermal conductivity is also beneficial.

5.1.3 Sapphire as a solid state detector

In order to operate sapphire crystal as a solid state detector, one has to fulfill certain conditions:

- an ionizing particle should produce enough charge carriers to be registered as a signal;

- lifetime and mobility of the charge carriers should be large enough to drift a variable part of the sensor thickness;
- low leakage current is essential to avoid noise;
- for certain applications the detector should be radiation hard.

An ionizing particle traveling through the crystal loses energy that partly goes to excitation of the lattice and partly for generation of free charge carriers. According to previous studies the mean energy needed to produce one electron-hole pair is linearly proportional to the bandgap size [103]. Using a phenomenological approximation and the bandgap of sapphire of 9.9 eV [104] it was estimated to be 27 eV . For a known crystal density and the specific energy loss of a MIP it can be translated into approximately 22 e-h pairs per μm of the detector material.

Charge transport in sapphire crystals was studied in Ref. [105] at zero applied electric field. It was found that the mobility of electrons at room temperature is high enough to generate fast signals needed in high energy physics applications. It is expected, that the mobility of holes is much smaller than the mobility of electrons. To ensure long lifetime of the charge carriers it is required to have single crystal sensors with a small amount of impurities.

Low leakage current at room temperature and high breakdown field in sapphire are the consequences of the wide bandgap. Sapphire is known as one of the best insulators available.

It was also found that the time characteristics of signals from sapphire sensors are similar to the ones from CVD diamond sensors [97].



Figure 5.3: Picture of the diamond [106] (left) and sapphire (middle, right) through linear polarized films of the cinema goggles.

To define the location of the defects in the sensor a simple method was used. It was applied before for diamond sensor as mentioned in Ref. [106]. The diamond

sensor was placed between crossed linearly polarizing films. As the diamond does not polarize light, there was almost no light seen passing through the films and the diamond sensor. Only at the location of defect and edges some light was polarized and passed through, as seen in Figure 5.3 (left). The result for a sapphire sensor placed between crossed polarizing films is different, as shown in Figure 5.3 (middle) and zoomed (right). Because of defects a sapphire crystal rotates the plane of polarization and is transparent in any configuration of the polarizing films.

It is known that charge carrier mobility in ionic crystals like sapphire is strongly dependent on the temperature. Values of electron mobility in sapphire vary between $600 \text{ cm}^2/(V \cdot s)$ at 20° C and $30000 \text{ cm}^2/(V \cdot s)$ at 40° K [105]. If the lifetime of free charge carriers is not decreasing rapidly with decreasing temperature, the prediction is the following: at cryogenic temperatures sapphire sensors will have "full" charge collection efficiency and extremely fast signals.

Relevant properties of sapphires are listed in Table 5.1. For comparison, the same properties are also given for diamond.

Table 5.1: Relevant material properties of single crystal artificial sapphire and diamond [107,109].

Material properties	sapphire	diamond
density, g / cm ³	3.98	3.52
bandgap, eV	9.9	5.47
energy to create an eh pair, eV	27	13
dielectric constant (depending on the orientation)	9.3 - 11.5	5.7
dielectric strength, V / cm	4×10^5	10^6
resistivity, Ohm·cm at 20° C	10^{16}	10^{16}
electron mobility, cm ² / (V·s) at 20° C	600	1800

The band gap of sapphire is larger than of diamond, resulting in a factor of two larger energy needed to create an electron-hole pair. The energy loss of a charged particle moving in sapphire is, however, larger than in diamond. The amount of charge carriers generated per unit length in sapphire is about 60 % of the amount generated in diamond.

5.2 Sensor characterization and tests

For studies described in this chapter the sapphire sensors were obtained from the CRYSTAL company [107]. Single crystal ingots were produced using the Czochralski method (see 5.1.1) and cut into wafers of $525 \mu\text{m}$ thickness. Contamination of other elements are on the level of a few ppm.

5.2.1 Electrodes

Sapphire sensors of $525 \mu\text{m}$ thickness and $10 \times 10 \text{ mm}^2$ size were metallized from both sides in GSI [108] with consecutive layers of Al, Ti and Au of 50 nm, 50 nm and 200 nm thickness, respectively. The size of the metallization was $9 \times 9 \text{ mm}^2$. On one side it was subdivided in four pads. Aluminium was chosen as the first layer of the metallization because of its well known firm mechanical adhesion to aluminium oxide. As the outermost layer of metallization gold was used. It protects the other metalized layers from oxidizing and ensures good contact for wire bonding. To prevent diffusion of gold into the aluminium oxide, titanium was used to separate the gold and aluminum layers.

5.2.2 Sensor characterization in the laboratory

An example of one of the first measurements of the leakage current for different pads of a sapphire sensor as a function of the applied voltage are shown in Figure 5.4. The measurements are done between 0 and 500 V for both polarities. In the same figure measurements of the signal current are shown when the sensor is irradiated with a ^{90}Sr source of several MBq activity. It was proven that the signal current generated by β -particles is high enough to be separated from the noise and is growing with the increase of the bias voltage [110].

The charge collection efficiency was measured with a ^{90}Sr source up to 1000 V bias voltage. Using a scintillation counter trigger the high energy part of β -spectrum was selected, which approximately corresponds to electrons with minimum specific ionization. The detector response was measured for different applied high voltages. Taking into account calibration and the expected amount of charge carriers generated in the sensor the CCE was determined. The CCE as a function of the bias voltage is shown in Figure 5.5. The red and blue colors represent results obtained in two different trials. The error bars correspond to the error of the mean value. Due to the small signal size the measurements are very sensitive to noise level and external conditions, therefore these measurements are very preliminary.

5.2.3 The response of sapphire sensor as a function of the dose

Two sensors of $525 \mu\text{m}$ thickness and $1 \times 1 \text{ cm}^2$ area were exposed to a high-intensity electron beam at the linear accelerator DALINAC at TU Darmstadt, Germany. The beam energy was 8.5 MeV , a typical value for electrons and positrons in the electromagnetic shower maximum for the near-beam calorimetry at the future linear collider [112]. The response of the sensors was measured as the signal current. The relative drop of the signal current, interpreted as the relative drop of the CCE is

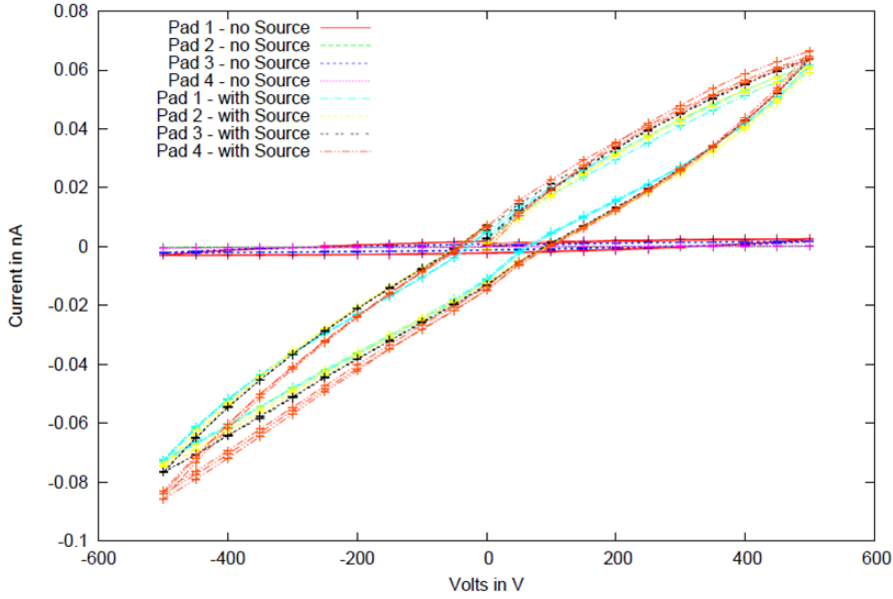


Figure 5.4: The leakage current and the signal current as a function of the bias voltage for different pads of sapphire sensor [110]. For the signal current measurements a ^{90}Sr source was used.

shown in Figure 5.6 for both sensor samples. As can be seen, the CCE degrades to about 30% of the initial CCE after a dose of 12 MGy , corresponding to more than 10 years of operation at e.g. the ILC [113] at nominal beam parameters at 500 GeV center-of-mass energy [114]. The peaks on the rather smooth curves show an increase of the CCE of about 10 % after periods when the beam was switched off to allow other intermediate measurements or because of beam losses. These breaks were about a few minutes. Assuming that the decrease of response is partly caused by a reduced field inside the sensor due to polarization, the short increase of the CCE indicates a release of trapped charge carriers with a corresponding decay constant. In addition, no current was seen during beam interruptions, indicating that the dominant trap release mechanism is recombination. When the beam was switched back on, the CCE continued to decrease. The leakage current of the sapphire sensors was measured before and after irradiation to be below 10 pA.

From laboratory measurements and beam tests it was concluded that sapphire is a promising material to be used as a current monitor. But it is also possible to use sapphire for single particle detection, as it will be described in the following sections.

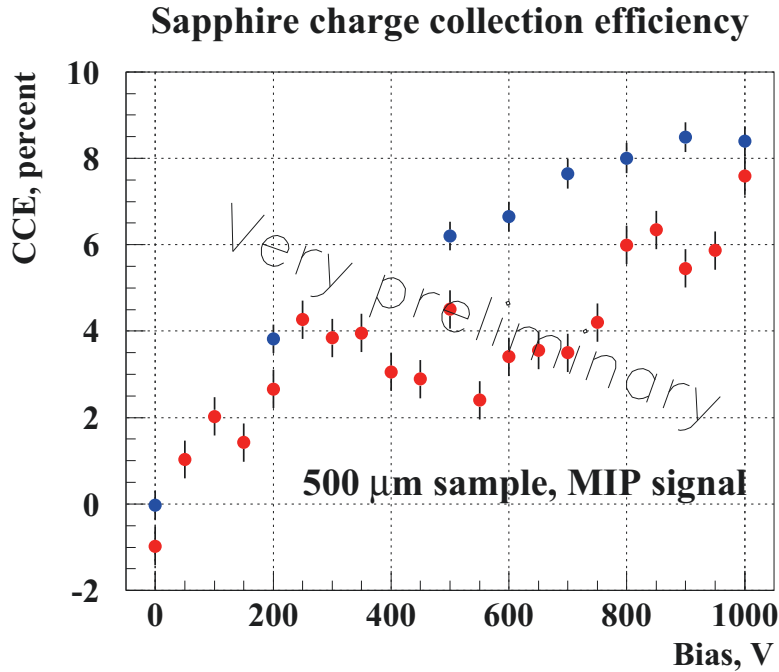


Figure 5.5: CCE as a function of bias voltage measured in the laboratory with a ^{90}Sr source [111]. The red and blue colors represent results obtained in two different trials.

5.3 Detector stack design

Taking into account the low CCE of the sapphire, a special sapphire stack design is proposed for individual particles detection. For a CCE of about 10% of industrially produced sapphire [111, 115] the signal expected for particles crossing a plate of $500\ \mu\text{m}$ thickness perpendicularly to its surface is only about 1100 e. However, if the particle crosses the sapphire sensor parallel to the $10 \times 10\ \text{mm}^2$ metallized surface, as shown in Figure 5.7 a), the signal is enhanced by a factor 20, amounting to about 22000 e, comparable to the one currently used in solid state detectors. Therefore the orientation of the sapphire plates in the test beam was chosen to be parallel to the beam direction. In addition, this orientation leads to a direction sensitivity. Only particles crossing the sensor parallel to the surface create the maximum signal. To increase the effective area of the detector, eight plates were assembled together. Each sensor has dimensions $10 \times 10 \times 0.525\ \text{mm}^3$, and was metallized from both sides

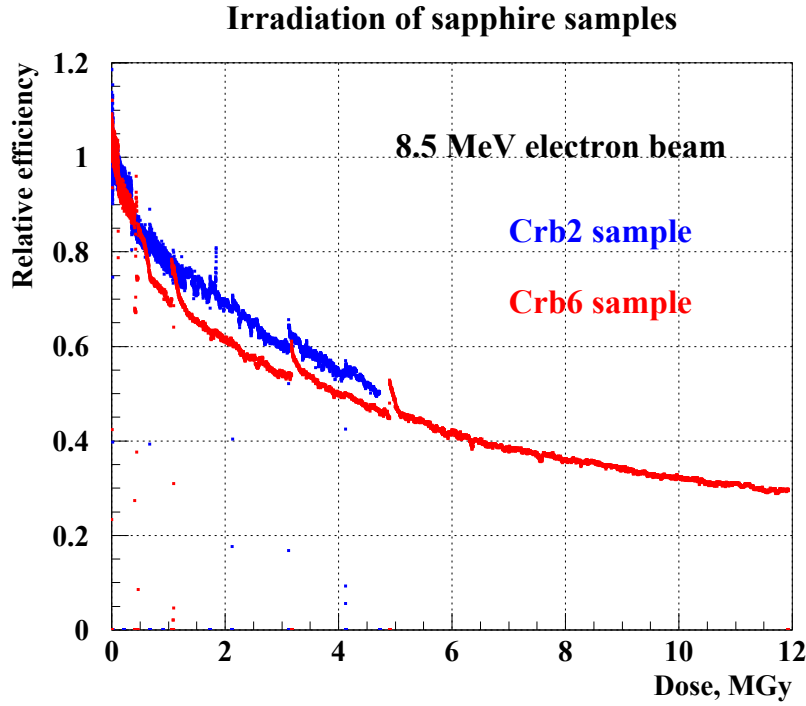


Figure 5.6: The relative CCE as a function of the dose in an electron beam for two sapphire sensors [111].

with consecutive layers of Al, Pt and Au. To allow wire-bonding connections to the high voltage and to the readout electronics, the plates were alternatively shifted to both sides. Each readout channel served two plates, as shown in Figure 5.7 b). On one side, shown on the top plate in Figure 5.7 b), the metallization has a square shape of $9 \times 9 \text{ mm}^2$ area. On the opposite side the metallization area is $9 \times 7 \text{ mm}^2$ with 9 mm parallel to the beam direction, as it is shown in Figure 5.7 c). This way an accidental contact of high voltage wire bonds with the readout pad on the adjacent sensor is excluded. The total height of the stack was 4.2 mm with 7 mm overlap of the metal pads, leading to a sensitive area of 29.4 mm^2 . The sensors were mounted inside a plastic frame as shown in Figure 5.7 d). The wire bonds for high voltage and readout connections are seen at the left and right side, respectively, in Figure 5.7 b) and d). The leakage current of each pair of sensors was measured to be below 10 pA at 1000 V .

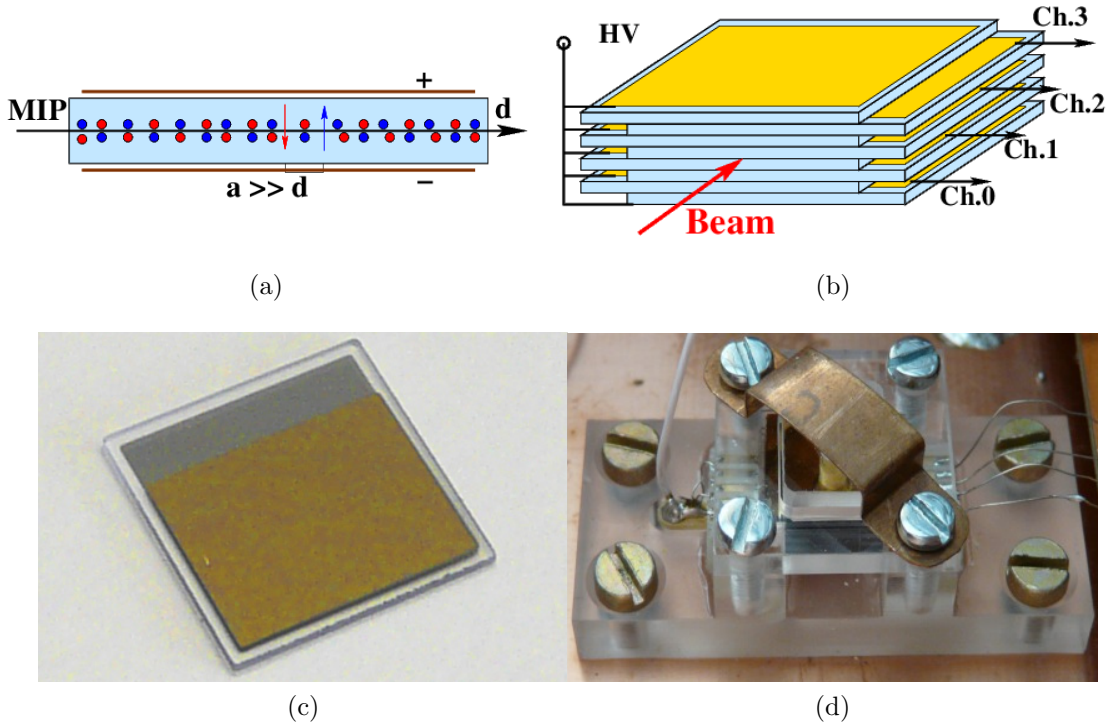


Figure 5.7: The sapphire detector under test: (a) – Orientation of single sapphire sensor with respect to the beam. (b) – Schematic view of detector stack consisting of eight metallized sapphire sensors. (c) – Metallized sapphire sensor. (d) – Assembled detector stack as used in the test beam.

5.4 Test beam setup

The stack was mounted in the middle of six planes of the EUDET pixel telescope in the 5 GeV electron beam of the DESY-II storage ring [79]. A photo of the EUDET pixel telescope with the XY-table for mounting of the test setup is shown in Figure 5.8.

The EUDET telescope is instrumented with Mimosa26 (Minimum Ionizing particle MOS Active pixel) sensors, comprised of 576×1152 pixels each, with a pixel size of $18.4 \times 18.4 \mu\text{m}^2$ on an area of $21.2 \times 10.6 \mu\text{m}^2$. The thickness of the sensors is $50 \mu\text{m}$. They are kept at a constant temperature of 14°C during operation.

Signals from sapphire sensors were amplified and shaped by charge-sensitive preamplifiers A250 [116] and RC-CR shapers with a peaking time of 100 ns and

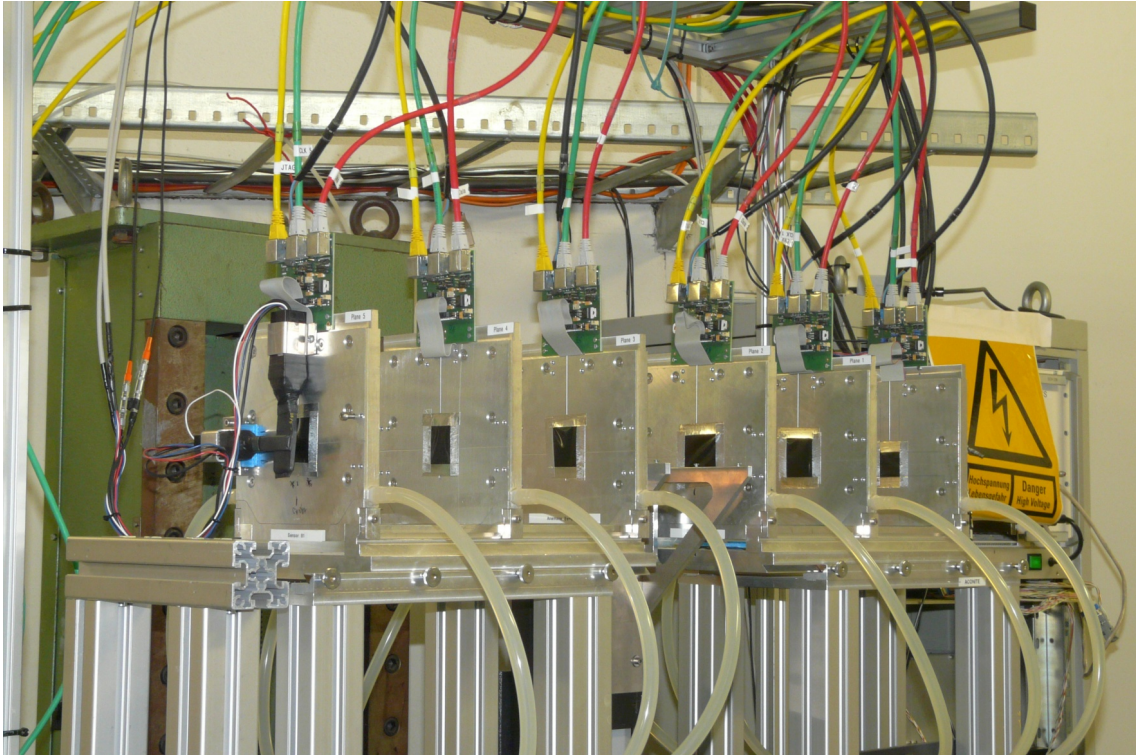


Figure 5.8: Photo of the EUDET pixel telescope in the beam test area (DESY II, Hamburg). The XY-table for mounting of the test setup is seen after the third telescope plane. Also cross of scintillators, which were used to trigger telescope readout is seen on the left hand side.

digitized by a 500 *MS/s* flash ADC v1721 [72].

Two pairs of scintillators, shown as light blue planes in Figure 5.9 upstream and downstream of the telescope, were used to trigger the readout of the telescope and the sensors.

5.5 Data synchronization and analysis

For the synchronization of the EUDET telescope and the stack readout a dedicated Trigger Logic Unit, TLU [79], was used. For each trigger the TLU distributed a trigger sequence to the EUDET telescope and the stack data acquisitions, such that a unique correspondence between records from both readouts was ensured. Occasionally there was a mismatch between the TLU number and ADC recorded number of triggers. To account for that an obligatory check for each event was

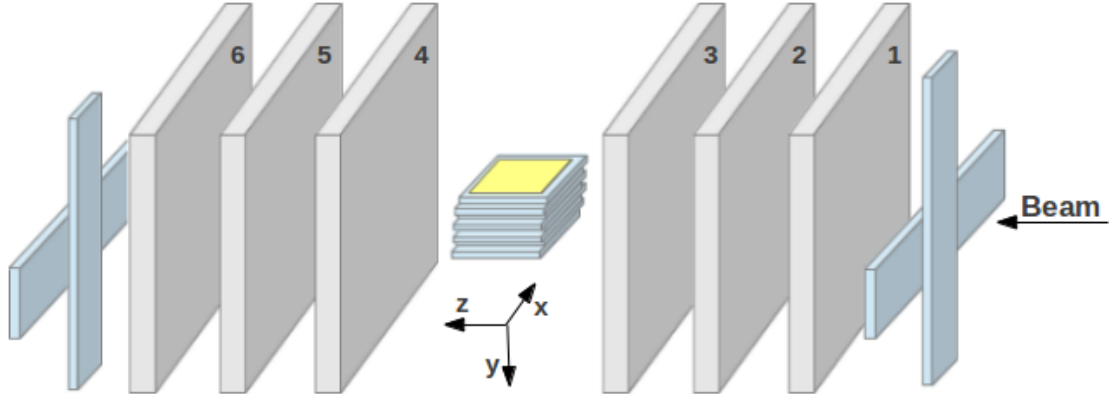


Figure 5.9: Sketch of the test beam setup. The sapphire stack was mounted in the middle of the 6 planes of the EUDET telescope. Crosses of two scintillators upstream and downstream of the telescope were used as the trigger for the DAQ.

introduced in the loop over events in the analysis program. In case of a mis-match the ADC event was skipped until a match between ADC event number and TLU number was found again.

5.5.1 Track reconstruction

The telescope planes were grouped in planes 1 – 3 forming the first arm, and planes 4 – 6 forming the second arm. Tracks from beam electrons were reconstructed for each arm separately. The standard telescope analysis software [79] was used to convert hits in the EUDET telescope into space-points in the user geometry with the origin of the coordinate system as shown in Figure 5.9.

The telescope planes have to be aligned before being analyzed. The alignment is done to define and correct for shifts and rotations of the telescope planes with respect to the first plane via the Millepede II program [117]. The special alignment run has to be done before the device under test installation between telescope plates to prevent the impact of multiple scattering on the alignment parameters. The alignment was done once and obtained alignment parameters were applied for all other runs. The width of residual distributions was measured in the alignment run to be below $4 \mu m$.

The EUDET telescope analysis software consists of the following processors:

- *Converter* converts raw data from the telescope into .lcio data format, since the EU Telescope library is based on ILCSOFT framework.

- *Clustering* defines pixels with a signal amplitude higher than a certain threshold and combines adjacent pixels into clusters.
- *Filter* algorithm for excluding noisy (“hot”) pixels using HotPixel database.
- *Correlator* processor, which calculates geometric offset values for telescope planes in x and y directions with respect to the first plane. It is considered as a pre-alignment.
- *HitMaker* defines the hit position in the cluster, which corresponds to the most central pixel of the cluster.
- *Alignment* applies earlier defined alignment parameters.
- *Fitter* uses χ^2 minimization. Multiple scattering in the planes is taken into account for track fit. Fitting in x and y directions are independent and done for each sensor separately.

5.5.2 Selection of data samples

From a Monte Carlo study the maximum displacement of the trajectory of a 5 GeV electron due to multiple scattering in the stack is about 10 μm , as the multiple scattering angle is estimated to be about 0.9 mrad [111]. For the current study scattered tracks were of critical importance, as they allow the reconstruction of the stack position in the beam using only scattered tracks. To adjust the sapphire stack position in the beam during the setup a 1 cm^3 lead cube was placed next to the sapphire stack. Due to the high density of lead almost all beam electrons were scattered on the cube. It allowed, from one data collecting run and fast telescope data analysis, a definition of the position of the stack in the beam by analyzing obtained hit maps. An empty area was seen in the hit maps corresponding to the cube position. By moving the XY-table and using hit maps the position of the stack was found in the central part of the beam. After the setup, the lead cube was removed and data collection started.

Events with more than one track candidate reconstructed from the telescope were rejected. This amount was about 30%. For the remaining events the fit of the track was done separately for the first and second arm of the telescope. The two reconstructed tracks were considered to originate from the same beam electron if their distance in the $z = 0$ plane was less than a predefined cut. Events matching this requirement were grouped in two sub-samples depending on the angle between the two tracks.

The first sub-sample contains events with an angle between the two tracks larger than 0.5 mrad and the second sub-sample with an angle between the two tracks less than 0.5 mrad . The number of events in each sub-sample is almost the same.

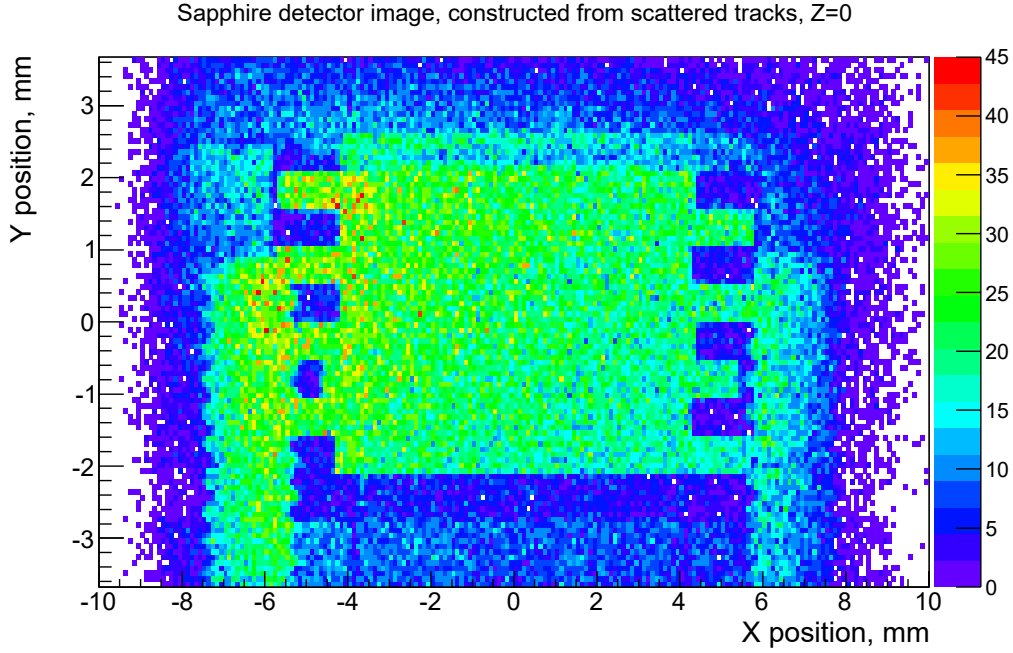


Figure 5.10: The image of the stack, obtained selecting tracks reconstructed in the first and second telescope arm requiring a space angle larger than 0.5 mrad . Counting plates from top to bottom, the two top plates correspond to readout channel 0 and the two bottom plates to readout channel 3.

Events of the first sub-sample were used to determine the precise position of the stack in the beam. From the distribution of the impact points of the track of the first arm at $z = 0$ an image of the stack in the xy plane at $z = 0$, a hit map, was obtained, as shown in Figure 5.10. This hit map played an important role in further analysis. The precise position of each plate was defined. It was needed to define the geometrical cuts for further analyses for selection of the hits in each readout channel separately. Counting plates in the hit map from top to bottom, the top two plates correspond to readout channel 0.

Also alternating protruding edges seen in Figure 5.10 on the left and on the right side were used to define the coordinate transformation for rotation and shift corrections of the stack. The sapphire stack alignment procedure and fit of the edges to a periodic function are described in Appendix B.

Events of the second sub-sample were used for the further signal analysis. Tracks reconstructed in the first arm, pointing into the detector area were used. The x and y position of their crossing point in the plane at $z = 0$ was determined. The fiducial area was defined using the coordinate system introduced in Figure 5.9 from the hit

map shown in Figure 5.10 as $-4 \text{ mm} < x < 4 \text{ mm}$ and $-2.1 \text{ mm} < y < 2.1 \text{ mm}$.

5.5.3 Sapphire sensor response

Based only on the events with tracks scattered with an angle less than 0.5 mrad in the sapphire sensors the waveforms recorded with the ADC were studied. The investigation of individual signals appeared to be not possible because of the observed noise. The waveforms corresponding to all tracks pointing to one of the sensors were averaged over about 2500 triggers. The average baseline for the same channel was obtained from all tracks not pointing to the sensors area, using about 4000 triggers per run. Average signals and average baseline plots for channel 0 are shown in Figure 5.11 a) and b), respectively. The bias voltage was set to 950 V .

The average signal of channel 0 after the average baseline subtraction is shown in Figure 5.11 c). The sapphire sensor signal is characterized by less than 10 ns rise-time, but the observed signal shape is defined by the used electronics. With a red-dashed line a 50 ns time-window selected for analysis is shown.

In both figures, large shrinkages of similar shape in the average signal and average baseline were observed. The shape of the baseline in each channel is slightly different, but the jump starts at the same time with respect to the signal. The signal arrival time is around 400 ns . The RMS of the baseline average, shown in Figure 5.11 d) is defined as:

$$RMS_{BL} = \sum_{n=1}^N \sqrt{(BL_n - BL_{aver.})^2} / N, \quad (5.1)$$

where BL_n is the instantaneous baseline value in a certain histogram bin, $BL_{aver.}$ is the average baseline value in the same bin and N is the number of entries in this bin.

The RMS_{BL} is small up to 500 ns and rises then considerably. In the further analysis ADC data was used only in the time interval $[420; 470] \text{ ns}$. From here and below the signal integral in this time interval will be used as the signal integral.

5.5.4 Common mode noise

Signals recorded by the ADC in the different channels were averaged over a large number of triggers.

Events with tracks not pointing into the detector, corresponding to the blue area in Figure 5.10, were used to study Common Mode Noise, hereafter referred to as CMN. The linear correlation of the noise in a pair of channels allows one to measure a signal in one channel of the pair by subtraction of the baseline in the other channel. Using this method the RMS of the signal integral distribution can be significantly reduced.

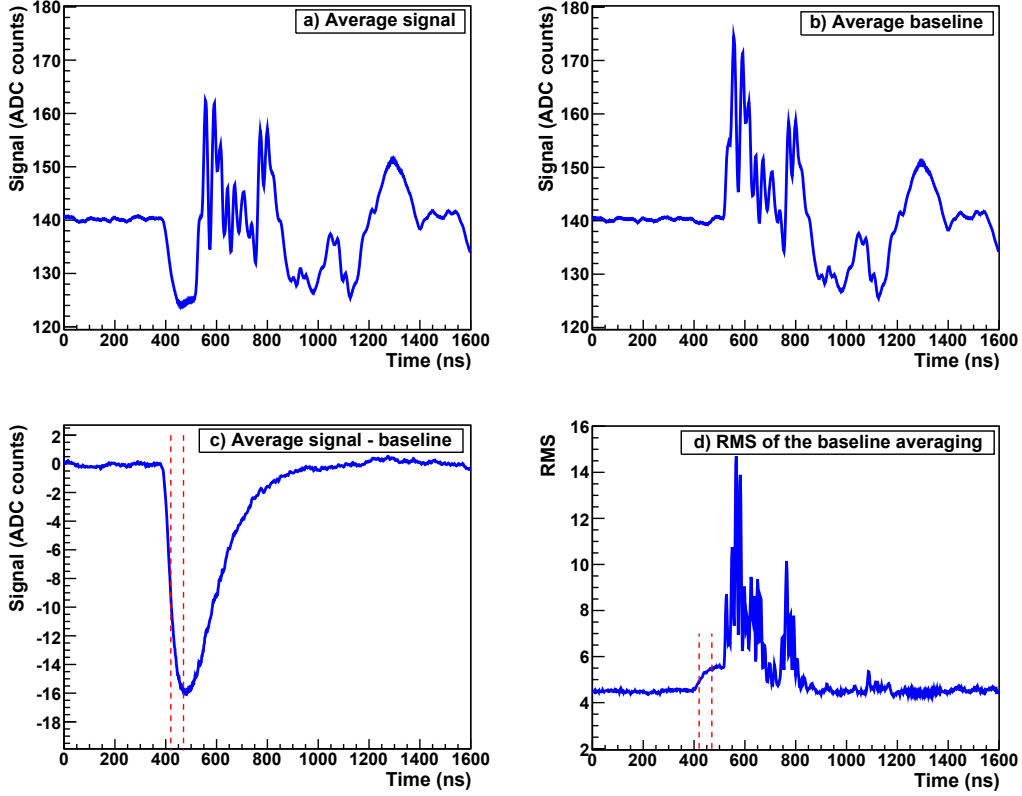


Figure 5.11: The average ADC values as a function of time from channel 0 at 950 V bias voltage. a) Average signal, b) average baseline, c) difference between average signal and average baseline, d) RMS of the baseline. The slice of the signal selected for analysis is marked with the dashed line.

The instantaneous baseline positions were calculated using a *ROOT*-based analysis code. Tracks pointing into the geometric area of the whole stack were excluded, guaranteeing the absence of signals in any of the channels. For the remaining tracks the integral of the baseline in $[420; 470]$ ns time-window was calculated and stored into a histogram for each channel. After a loop over all events of the selected data file the histogram of each channel was averaged to define the mean value of the baseline in this channel. The RMS of the baseline value in this histogram describes the noise level.

The correlations of the baselines were investigated for all combination of channels as is shown on the 2D histograms in Figure 5.12. The x and y axes correspond to the difference of the average and instantaneous baseline values in arbitrary units

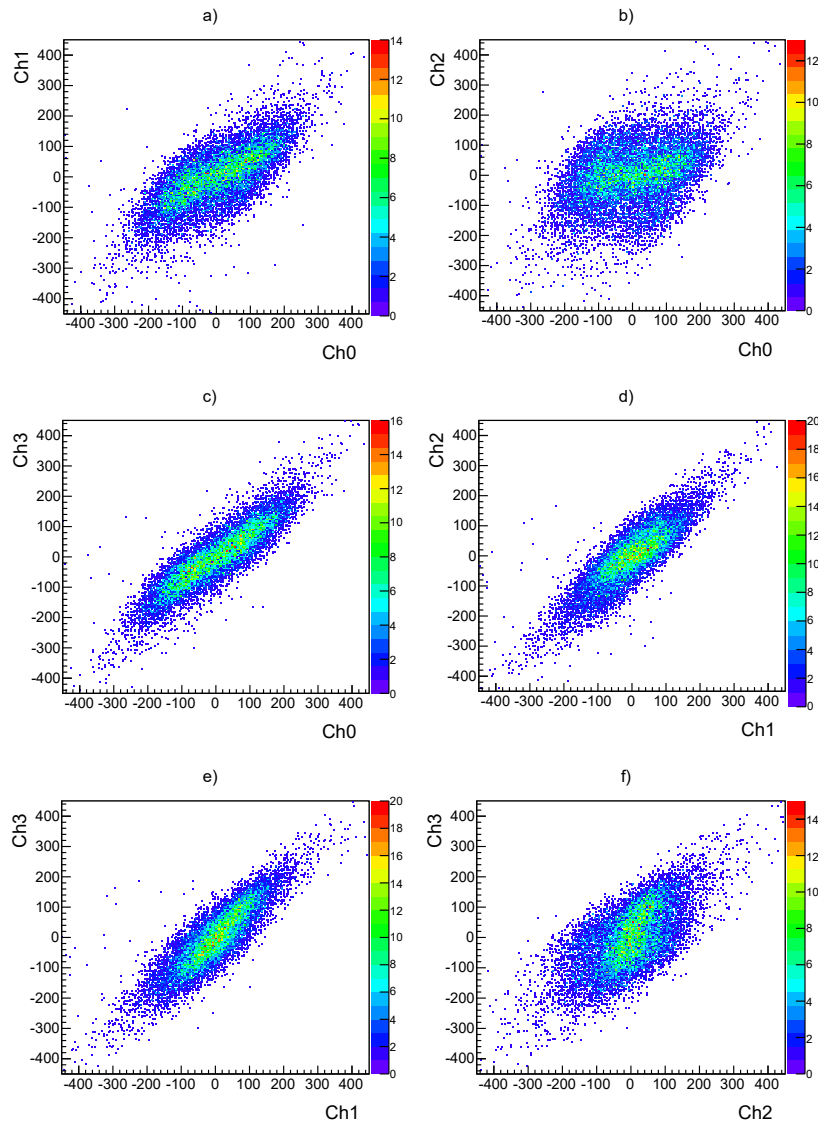


Figure 5.12: Correlation plots for each combination of channels. On the x and y axis, the difference between the instantaneous and average baseline values for particular pair of channels is plotted. About 14000 triggers correspond to one plot. The bias voltage is 950 V.

for a given pair of channels. Each plot contains about 14000 triggers. Plots for different data files and different high voltage settings are very similar. Channel 0 and channel 3 (Figure 5.12, c)), as well as channel 1 and channel 4 (Figure 5.12, d)), are fully correlated. These correlations were used in the further analysis for CMN

subtraction. To keep the method simple and transparent only the linear component was taken into account.

5.5.5 Signal spectrum

The energy deposition in the sensor by the passing of 5 *GeV* electrons was estimated from a GEANT3 simulation [118, 119]. The distribution is shown in Figure 5.13. The fit to a Landau distribution convoluted with a Gaussian distribution results in $MPV_{Landau} = 6.044 \text{ MeV}$, $\sigma_{Landau} = 0.331 \text{ MeV}$ and σ_{Gauss} compatible with zero. Also a small peak is seen below 2 *MeV*. It is related to the deposition of the delta electrons kicked out from neighbor plates.

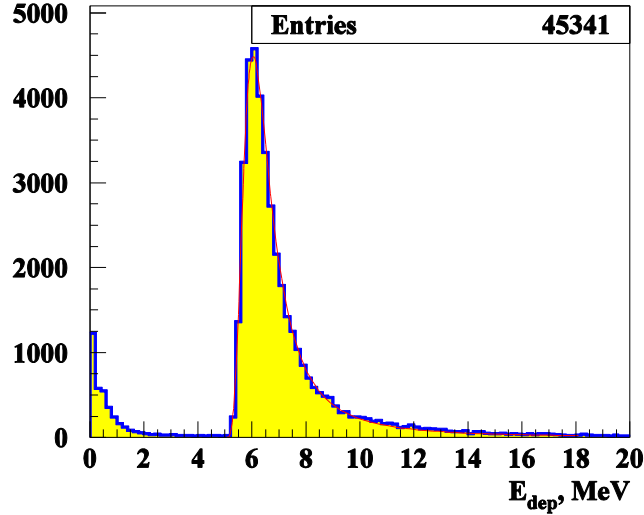


Figure 5.13: Typical deposited energy into the sapphire crystal by 5 *GeV* electron. GEANT3 simulation [119].

An example of the signal spectrum at 700 *V* bias voltage before and after CMN subtraction is shown in Figure 5.14. The data histogram is shown in blue and the fit to a Landau distribution convoluted with a Gaussian distribution is shown in red.

Similar distributions were obtained at bias voltages 500 *V* and 950 *V*. A comparison of the distribution before and after CMN subtraction was done. For example for channels 0 and 3 CMN subtraction leads to a narrower signal spectrum. The RMS is reduced by $\sqrt{200^2 - 177^2} \simeq 90$ units. The mean value of the distribution

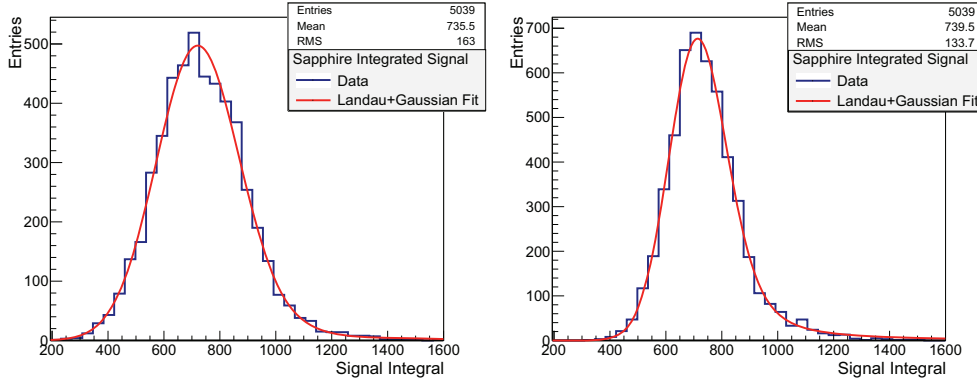


Figure 5.14: An example of the sapphire signal spectrum at 700 V bias voltage before (left) and after (right) CMN subtraction. Data in blue, fit to a Landau distribution convoluted with a Gaussian distribution in red.

remain almost the same. In the further studies, where the relative stability of the peak position and not the absolute values are of interest the simple mean of the histogram was used. It appeared to be less sensitive to CMN and allowed to keep the analysis simple and robust. The precise values of the mean values of the signal distribution and RMS before and after CMN subtraction are listed in Table 5.2.

5.5.6 Systematic errors

In further homogeneity and CCE studies, sapphire plates were subdivided into small pixels using telescope information. Therefore, the local y coordinate determination precision should be taken into account.

- The local y coordinate variation along the particle path in the sapphire plate is introduced because of the tilt of the stack. Taking the tilt angle $f = |\sin(\theta)| = 0.00431$ obtained from the fit (Appendix B) and path length under the electrode of 9 mm, the full local y coordinate variation along the path is 40 μm with $RMS \approx 40 \mu\text{m}/\sqrt{12} \approx 11 \mu\text{m}$.
- Telescope pointing track resolution is about 5 μm .
- To estimate the displacement of the electron path by multiple scattering of 5 GeV electrons in 10 mm of sapphire, a Monte Carlo study was done. A maximum displacement of 10 μm was obtained.

Table 5.2: The parameters of the fit of the signal distributions: MPV_{Landau} , σ_{Landau} and σ_{Gauss} in MeV and the mean, and RMS obtained from the histograms before and after the CMN subtraction for different high voltage settings.

Value	Before CMN subtraction	After CMN subtraction
HV = 500 V		
MPV_{Landau}	100.6 ± 1.6	106.1 ± 1.8
σ_{Landau}	14.8 ± 1.2	16.3 ± 1.0
$\sigma_{Gaussian}$	119.2 ± 1.7	66.7 ± 1.8
Mean	154.5	156.2
RMS	139.3	113.0
HV = 700 V		
Landau MPV	197.6 ± 1.8	186.1 ± 1.7
σ_{Landau}	8.7 ± 0.9	16.1 ± 1.0
$\sigma_{Gaussian}$	143.8 ± 1.6	94.2 ± 1.6
Mean	235.5	239.5
RMS	163.0	133.7
HV = 950 V		
Landau MPV	170.2 ± 1.7	153.4 ± 1.6
σ_{Landau}	15.2 ± 1.0	16.6 ± 0.9
$\sigma_{Gaussian}$	165.4 ± 1.6	148.4 ± 1.4
Mean	323.9	338.0
RMS	191.8	168.8

The error sources are uncorrelated. Adding the values quadratically, the full systematic error is estimated to be about $16 \mu\text{m}$. The minimum bin width for y coordinate dependency studies was chosen to be $25 \mu\text{m}$.

5.6 Charge collection efficiency

An example of the averaged signal after the CMN subtraction and linear coordinate transformation is shown in Figure 5.15 for the sapphire plate 1 at two different bias voltages. The black pulse is obtained at a bias voltage of 950 V , the red pulse at 550 V . As expected, a higher electric field leads to more collected charge and therefore to a higher amplitude. Similar results are obtained for the other plates with slightly different amplitudes as discussed in detail below.

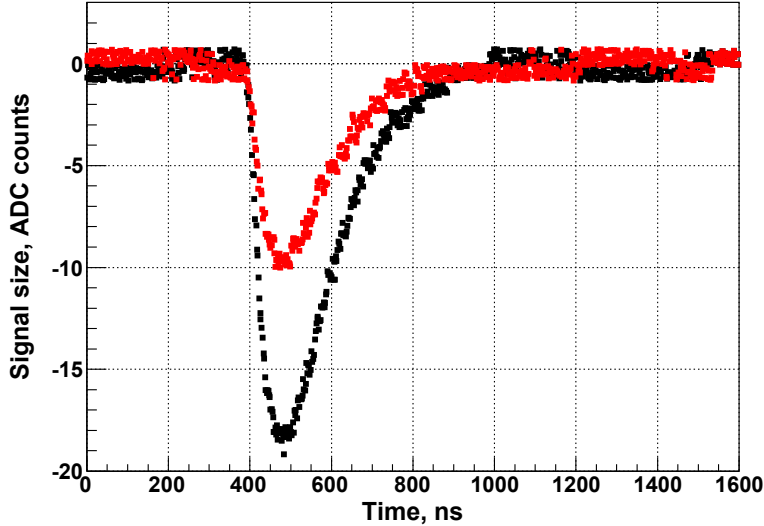


Figure 5.15: The averaged signal at the bias voltage of 550 V in red and at 950 V in black for events with tracks hitting one plate of the sapphire stack after CMN subtraction.

The CCE is defined as the ratio of the measured to the expected signal charge. The signal charge is obtained by the integration of the signal waveform over a 50 ns time interval, as discussed in subsection 5.5.3. The mean value of the distribution of the signal charge was used for the CCE calculation at each bias voltage value.

In order to convert the mean value into a charge each channel was calibrated by injecting a known charge into the preamplifier input. The ionization energy loss

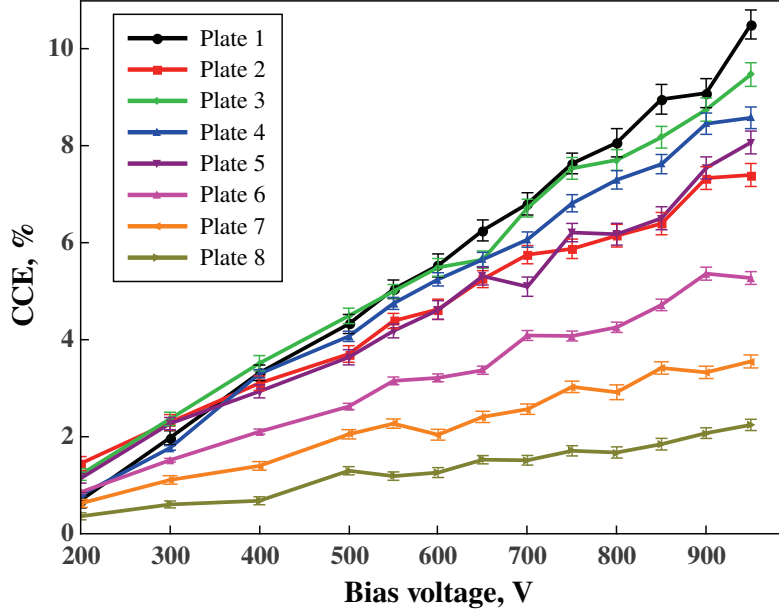


Figure 5.16: Measurement of the mean charge collection efficiency for eight sapphire plates as a function of the bias voltage.

Table 5.3: The measured CCE at the highest applied bias voltage of 950 V with statistical and systematic uncertainties. Also given are the quantities $\langle \text{CCE} \rangle$ and RMS obtained from averaging CCE values from horizontal homogeneity study in 500 μm steps in the x coordinate.

Plate number	1	2	3	4	5	6	7	8
CCE, %	10.5	7.4	9.5	8.6	8.1	5.3	3.6	2.2
Stat. error	0.3	0.2	0.2	0.2	0.2	0.1	0.1	0.1
Syst. error	0.2	0.2	0.2	0.2	0.2	0.1	0.1	0.1
$\langle \text{CCE} \rangle$, %	9.9	7.2	9.0	8.5	7.5	5.3	3.7	2.1
RMS	1.7	0.9	0.9	0.8	0.6	0.5	0.9	0.7

distribution as a function of a particle energy obtained from a GEANT3 [118] simulation was shown in Figure 5.13. The expected amount of generated electron-hole pairs is estimated from the mean value of the ionization energy loss inside the sensor and the energy needed to create an electron-hole pair is given in Table 5.1. This quantity is estimated using the extrapolation proposed in Ref. [103], and corrected for wide band-gap semiconductors [104].

The measured CCE is shown in Figure 5.16 as a function of the bias voltage for all plates of the stack. For each voltage value the statistics of about 100000 triggers were used. To exclude signals with reduced amplitude expected at the edges of the metallization pads due to distortions of the electric field the fiducial area was reduced in x to $-3 \text{ mm} < x < 3 \text{ mm}$. An almost linear rise of the CCE is observed, reaching at 950 V for plane 1 a value of 10.5%. The values of the CCE obtained for all plates at a voltage of 950 V are listed in Table 5.3. The statistical error is obtained as the standard deviation of the mean value. The systematic uncertainty is the uncertainty due to the calibration and the uncertainty due to the transition region between adjacent plates in the y coordinate, added in quadrature. The measured CCE varies from sample-to-sample reflecting variation of the substrate quality. As can be seen, 5 out of the 8 sensor plates have a relatively high and similar CCE between 7 and 10%, while three other plates have lower and different CCE values.

To study the homogeneity of the response along the sapphire plates, described in subsection 5.7, a high statistics run was performed at 950 V . Each plate was subdivided into $500 \mu\text{m}$ pixels and the average CCE, referred hereafter to $\langle\text{CCE}\rangle$, was defined. Individual CCE values for all pixels are shown in Figure 5.17. 12 CCE measurements in pixels along the x coordinate in the range $-3 \text{ mm} < x < 3 \text{ mm}$ were included in the $\langle\text{CCE}\rangle$. The $\langle\text{CCE}\rangle$ values are given together with the RMS in the Table 5.3. The CCE of the whole sapphire plate obtained from the voltage scan and the $\langle\text{CCE}\rangle$ from the homogeneity study are in agreement within the uncertainties of the measurement.

5.7 Study of the sensor response as a function of the x coordinate

The CCE was measured as a function of the x coordinate in the range $-7 \text{ mm} < x < 7 \text{ mm}$. It was extended beyond the sensor length to see the behavior at the edges. Data of a high statistics run performed at the bias voltage 950 V was used.

Dividing the range $-7 \text{ mm} < x < 7 \text{ mm}$ into $500 \mu\text{m}$ wide pixels we obtain 28 spectra histograms per plate. The average of each histogram translated into CCE value is represented by one point in Figure 5.17. The plates are shown in groups of two, keeping correspondence to the readout channels. A fast rise of the CCE is observed for all plates starting at the edge of the metallization. The shift of the odd

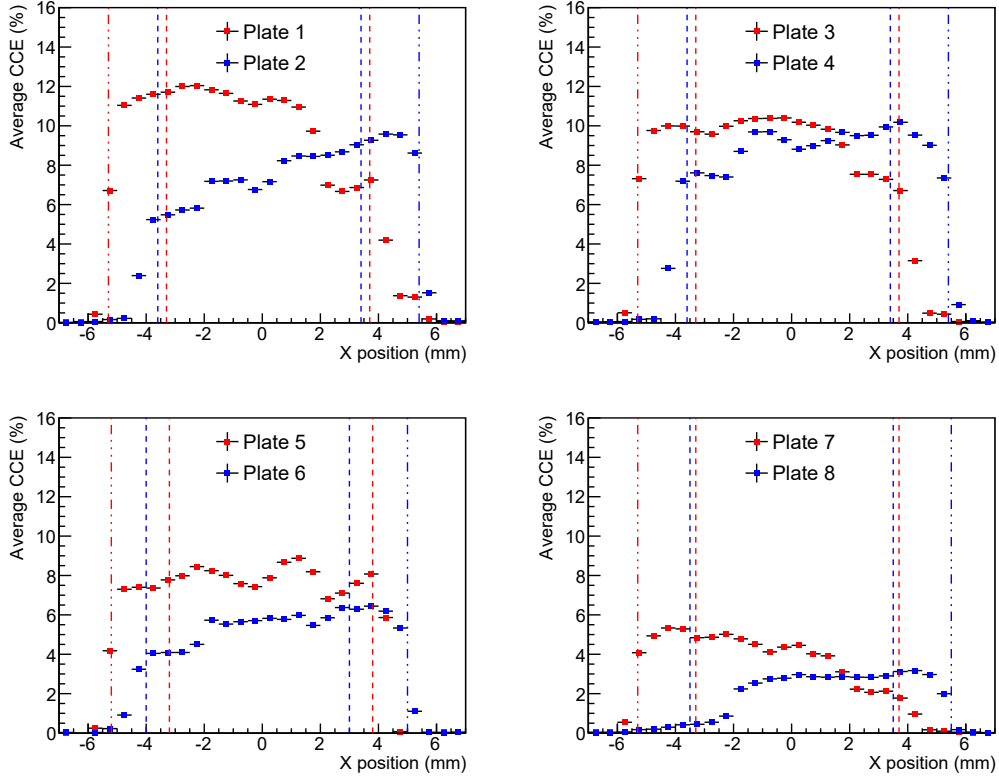


Figure 5.17: Average CCE of the sapphire plates as a function of x , measured in $500 \mu\text{m}$ wide pixels. With the dashed lines metallized area at both sides of the plate are marked. Additional dash-dotted lines point to the location of the extended metallization for each plate.

plates to the left and even plates to the right side is clearly seen and correspond to geometrical design of the sapphire stack as seen in Figure 5.10. In Figure 5.17 the area of the plate metallization from both sides is marked with a dashed line. The dash-dotted line points to the location of the longer metallization (see Figure 5.7, c)). Results for odd plates are plotted in red and for even plates in blue.

For all plates variations of the CCE as a function of x are observed. In range $-2 \text{ mm} < x < 2 \text{ mm}$ it remains stable for all plates. A step down for odd plates is observed in the range $[2; 4] \text{ mm}$ and for even plates in the range $[-4; -2] \text{ mm}$. As it is seen for all plates we can assume that this effect is related to nonuniform electrical field in the mentioned regions.

5.8 CCE as a function of time

The high statistics run at a bias voltage of 950 V was also used for a measurement of the CCE as a function of time. More than 40 short runs with about 100K triggers per run were taken in about 16 hours at stable conditions.

For each short run the signal integral spectrum for plate 1 for two different ranges was used. The first range was the same as for the CCE measurements in subsection 5.6, $-3 \text{ mm} < x < 3 \text{ mm}$. The second range was tighter, $-2 \text{ mm} < x < 2 \text{ mm}$, corresponding to high CCE values described in subsection 5.7.

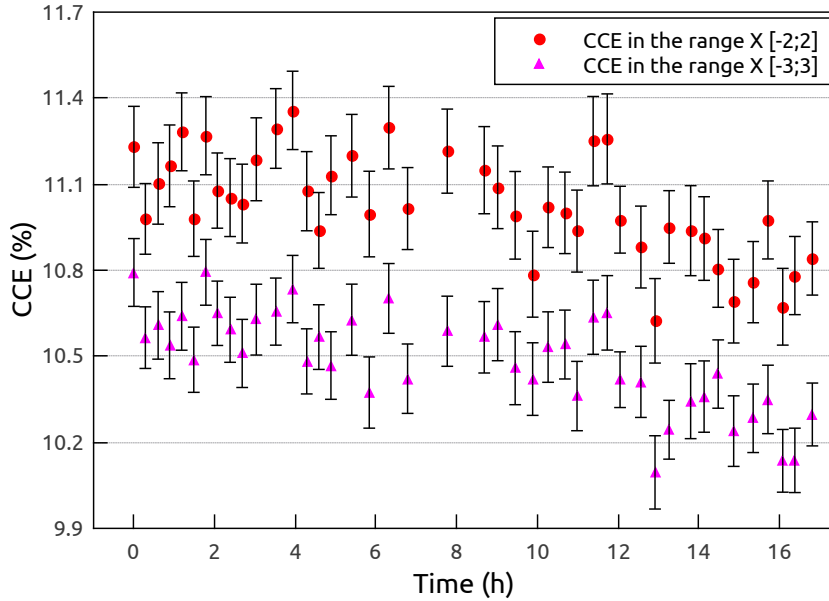


Figure 5.18: The CCE at 950 V of the plate 1 of the sapphire stack as a function of time. Each point corresponds to the average CCE value measured during 15-20 min.

There is a slight decrease observed in the average CCE value in both selected ranges, as seen in Figure 5.18. As expected, the CCE in the range $x [-2; 2]$ is higher, but the time dependence is similar for both ranges. The CCE is decreasing by about 3% between starting and end points. According to results shown in subsection 5.2.3, the radiation damage during 16 hours of irradiation with 5 GeV electrons is negligible and could not affect the CCE. The observed drop in the CCE might be related to a trap occupation state and a possible change of the polarization field. It should be taken into account that the measurement of the CCE as a function of the bias voltage was done before the high statistics run. Thence the detector was already irradiated.

5.9 A model to describe the CCE of sapphire sensors

A linear model was developed to describe the CCE as a function of the local y coordinate inside a sapphire plate. The effect of medium polarization is taken into account.

Charged particles cross the sensor and ionize the atoms along their path through the sensor. They produce in the detector p electron-hole pairs per unit volume per second. The number of charge carriers of each sign $p dy$ is produced in the thin layer of the thickness dy . If a bias voltage V is applied to the detector of thickness d with the positive electrode at $y = 0$ and negative electrode at $y = d$, holes will start to drift in the positive y direction. Similarly, for electrons, drifting in negative y direction. Their production rate at certain depth y will be:

$$\Phi_y^+ = \int_0^y p dy = py, \quad (5.2)$$

$$\Phi_y^- = \int_y^d p dy = p(d - y) \quad (5.3)$$

5.9.1 Dependence of electric field on sensor depth

Assuming that a small part of drifting charges is trapped and kept in place, the density of trapped charges is proportional to the production rate. It is described by Eq. 5.2 and 5.3. Taking the charge sign into account, a space charge density ρ will be a linear function of y :

$$\rho \propto p(2y - d) \quad (5.4)$$

The coefficient of proportionality in Eq. 5.4 depends on the capture cross section of the trap, and could be affected by many factors like recombination probability, temperature, charge carriers mobility. In this model we consider the simplest case of constant coefficients being equal for electrons and holes. In order to avoid continuous accumulation of space charge and to achieve the stable steady state, one could introduce trap release. If the trap release lifetime is not very long and trap occupation is small the release rate will be proportional to the number of occupied traps. A linear dependence of space charge density on y holds also for the steady state.

A space charge of course generates an internal electric field (polarization field), with the direction opposite to the external applied field. In the linear approximation

it could be calculated by using the charged plane electric field formula, integrated over the detector depth:

$$E(y) \propto \int_0^{y_1} \rho dy - \int_{y_1}^d \rho dy = \int_0^{y_1} \rho dy + \int_{y_1}^d \rho dy - 2 \int_{y_1}^d \rho dy = -2 \int_{y_1}^d \rho dy \quad (5.5)$$

Here we made the assumption that the crystal is neutral and the integral of space charge over the full depth is zero. Substituting the expression for the space charge density obtained in Eq. 5.4, we get:

$$E(y) \propto -2 \int_{y_1}^d p(2y - d)dy = -4p \int_{y_1}^d y dy + 2pd \int_{y_1}^d dy = 2p \left[\left(y_1 - \frac{d}{2} \right)^2 - \frac{d^2}{4} \right]. \quad (5.6)$$

The polarization field has a parabolic shape, being zero at the crystal boundaries. Finally, some constant field from charges stored at the electrodes should be added to fulfill the boundary condition:

$$\int_0^d E(y)dy = V. \quad (5.7)$$

As a result, for the further analysis we assume the dependence of electric field on the sensor depth to be:

$$E(y) = A \left(y - \frac{d}{2} \right)^2 + B, \quad (5.8)$$

where A and B are parameters. Because of the boundary condition in Eq. 5.7, these parameters are not independent.

Integrating the electric field over the sensor depth, one gets:

$$\int_0^d E(y)dy = A \int_0^d \left(y - \frac{d}{2} \right)^2 dy + B \int_0^d dy = A \int_{-d/2}^{d/2} y^2 dy + Bd = \frac{Ad^3}{12} + Bd = V. \quad (5.9)$$

As expected, in case of zero polarization ($A = 0$), the electric field is uniform and $E = B = V/d$.

5.9.2 Signal size estimate

Charge carriers, created by an ionizing particle, drift in the electric field thus inducing the signal on the sensor electrodes. To estimate the signal size electrons and holes will be considered separately, as they may contribute to the signal differently. Drift velocity in linear approximation is proportional to the electric field strength:

$$v_{e,h} = \mu_{e,h} E(y), \quad (5.10)$$

where $\mu_{e,h}$ is the mobility for electrons and holes, respectively. For the drift in a non-uniform electric field the velocity is position dependent.

The charge carrier lifetime $\tau_{e,h}$ is assumed to be constant. Then the number of carriers at time t is:

$$N_{e,h}(t) = f_d \cdot N_0 e^{-t/\tau_{e,h}}, \quad (5.11)$$

where N_0 is the amount of created charge carriers, f_d is the fraction of both types of charge carriers. According to Ramo's theorem the differential contribution to the observed signal will be:

$$dQ = \frac{e}{d} N_{e,h}(t) v_{e,h} dt. \quad (5.12)$$

In order to express the number of charge carriers as a function of the position, we use $dt = \frac{dy}{\mu_{e,h} E(y)}$. The time needed for charge carriers to drift a distance from the production point y_0 to a point y_1 , is:

$$\begin{aligned} \Delta t &= \int_{y_0}^{y_1} \frac{dy}{\mu E(y)} = \frac{1}{\mu} \int_{y_0}^{y_1} \frac{dy}{A \left(y - \frac{d}{2} \right)^2 + B} = \\ &= \frac{1}{\mu} \int_{y_0 - \frac{d}{2}}^{y_1 - \frac{d}{2}} \frac{dy}{Ay^2 + B} = \frac{1}{\mu \sqrt{AB}} \arctan \left(y \sqrt{\frac{A}{B}} \right) \Big|_{y_0 - \frac{d}{2}}^{y_1 - \frac{d}{2}} = \\ &= \frac{1}{\mu \sqrt{AB}} \left[\arctan \left(\sqrt{\frac{A}{B}} \left(y_1 - \frac{d}{2} \right) \right) - \arctan \left(\sqrt{\frac{A}{B}} \left(y_0 - \frac{d}{2} \right) \right) \right]. \end{aligned} \quad (5.13)$$

Substituting dt from the Eq. 5.13 and N from the Eq. 5.11 into Eq. 5.12 and integrating from the charge carrier generation point y_0 to the electrode surface, the generated charge is:

$$Q(y) = \frac{e \cdot f_d \cdot N_0}{d} e^{-\frac{\arctan \left(\left(y_0 - \frac{d}{2} \right) \sqrt{\frac{A}{B}} \right)}{\mu \tau \sqrt{AB}}} \int_{y_0}^d e^{-\frac{\arctan \left(\left(y - \frac{d}{2} \right) \sqrt{\frac{A}{B}} \right)}{\mu \tau \sqrt{AB}}} dy. \quad (5.14)$$

The quantity B is the electric field strength at the plane in the middle of the plate $y = d/2$, and $\mu\tau$ is the drift path length of the electrons or holes in the electric field of unit strength. The ratio $Q/N_0 \times e$ is then the fraction of the charge carriers contribution to the observed CCE. In case of $\mu\tau E \ll d$ the proportionality between the charge carrier drift path and electric field strength leads to the linear dependence of the CCE on the detector bias voltage. This statement is in agreement with the measurement shown in Figure 5.16.

It seems to be not possible to find an exact analytical expression for the integral from Eq. 5.14, so one can use a Taylor expansion and keep under the integral all terms up to the third order:

$$e^{-\frac{\arctan \left(\left(y - \frac{d}{2} \right) \sqrt{\frac{A}{B}} \right)}{\mu \tau \sqrt{AB}}} = 1 - \frac{y - \frac{d}{2}}{\mu \tau B} + \frac{\left(y - \frac{d}{2} \right)^2}{2 \mu^2 \tau^2 B^2} + \frac{(2 \mu^2 \tau^2 AB - 1) \left(y - \frac{d}{2} \right)^3}{6 \mu^3 \tau^3 B^3} + \dots \quad (5.15)$$

Table 5.4: Parameters obtained from the fit of the CCE measured as a function of the local y using Eq. 5.14 at the bias voltage of 950 V [119].

Plate number	B, ($V/\mu m$)	f_d , (%)	$\mu\tau(e)$, ($\mu m^2/Vs$)	$\mu\tau(h)$, ($\mu m^2/Vs$)	χ^2
1	1.327 ± 0.012	52.9 ± 0.5	79.1 ± 1.1	4.2 ± 0.3	19
2	1.255 ± 0.011	47.1 ± 0.5	59.5 ± 0.9	6.2 ± 0.3	41
3	1.307 ± 0.010	53.3 ± 0.5	64.9 ± 0.9	6.4 ± 0.2	27
4	1.287 ± 0.011	48.1 ± 0.5	74.6 ± 1.0	3.3 ± 0.3	27
5	1.421 ± 0.010	47.1 ± 0.7	62.9 ± 1.0	3.2 ± 0.4	16
6	1.342 ± 0.013	43.5 ± 1.3	39.4 ± 1.2	5.1 ± 0.4	42
7	1.484 ± 0.010	50.1 ± 1.2	22.0 ± 0.8	3.7 ± 0.4	19
8	1.330 ± 0.010	40.7 ± 1.7	15.1 ± 0.5	3.2 ± 0.4	33

Another possibility is to compute the integral in Eq. 5.14 numerically. The last option was used to fit Eq. 5.14 to the measured dependence of the CCE as a function of local y coordinate.

There are the following parameters: A and B for the electric field description, $\mu\tau$ for the charge carriers dynamics description and the overall normalization factor. From Eq. 5.14 it is obvious that the parameters A , B and a $\mu\tau$ are correlated, so the boundary condition Eq. 5.7 was used to resolve the ambiguity. It was also assumed to use the same normalization factor for holes and electrons, which is natural in view of prompt recombination when the number of produced free holes and electrons is reduced by an equal amount. Four parameters were used in the fit: B for electric field description, $\mu\tau$ for electrons and holes separately, taking into account the drift in opposite directions and a normalization coefficient.

5.9.3 CCE as a function of local y

Figure 5.19 shows the CCE as a function of the local y coordinate for a bias voltage of 950 V. Using track pointing information the CCE was measured in thin 25 μm slices. Results are shown together with a fit using Eq. 5.14.

For adjacent plates the electric field has the opposite direction. For example, $y = 0 \mu m$ of plate 1 and $y = 525 \mu m$ of plate 2 correspond to the same readout electrode.

In plates 1, 3, 5 and 7 negative electrode correspond to $y = 0 \mu m$, the electric field is directed from $y = 525 \mu m$ to $y = 0 \mu m$ and the CCE is shown in red dots. In plates 2, 4, 6 and 8 negative electrodes correspond to $y = 525 \mu m$, the electric field direction is opposite, and the CCE is shown in blue dots.

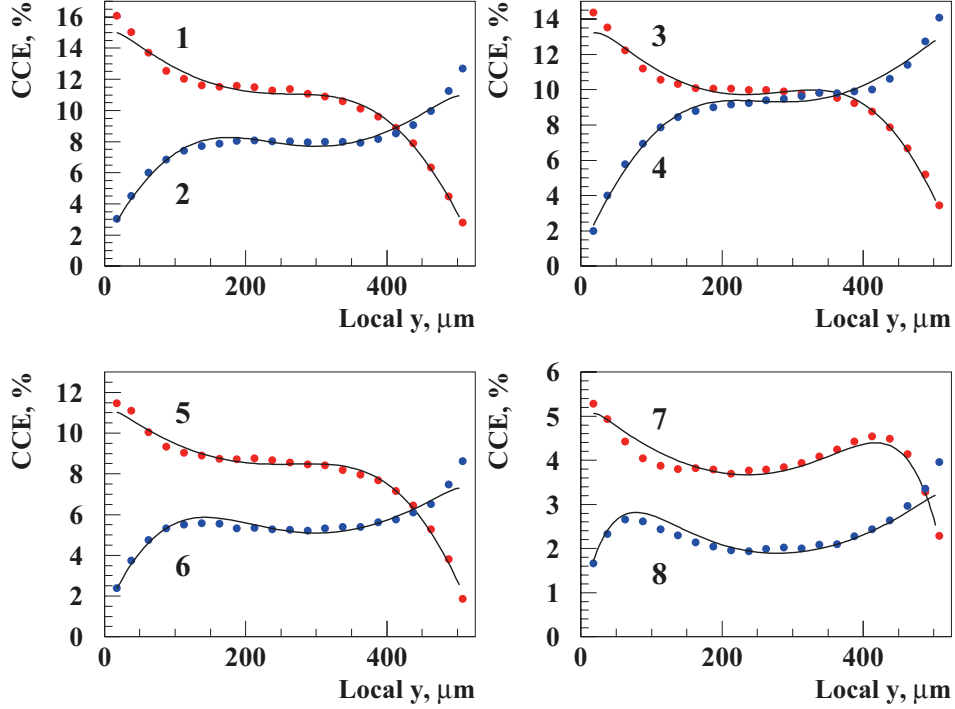


Figure 5.19: The CCE measured as a function of the local y coordinate inside a plate in slices of $25 \mu m$ for all plates of the sapphire stack. Blue dots are for the plates with electric field in the direction of y and red dots for the plates with opposite field direction. The lines are the result of a fit including both electron and hole drift. The fit parameters are given in Table 5.4.

For all plates signal is reduced in the vicinity of the positive electrode and has a maximum at the negative electrode. The drop near positive electrode could be interpreted as the dominant contribution of electrons in charge collection.

There is also dependency of the observed curve shape on the CCE of the plate. For example for plates 1 and 3 with the highest average CCE, the drop of the CCE begins at a distance of about $150 \mu m$ from the positive electrode. For plates 7 and 8 with the lowest average CCE value drop of CCE begins only at about $50 \mu m$ from the positive electrode, and in addition the second local maximum is seen at a distance of about $70 \mu m$ from the positive electrode. This result points to a shorter charge carrier path in the sensor with lower CCE and is evidence of a presence of a

significant polarization field.

The parameters of the fit are listed in Table 5.4. As can be seen, the $\mu\tau$ of electrons is in most of the cases more than 10 times larger than the $\mu\tau$ of the holes at roughly the same field strength.

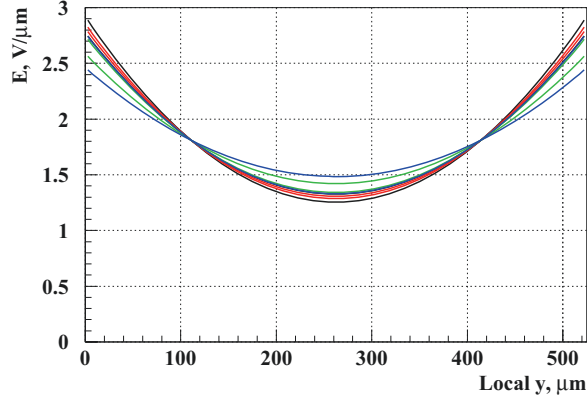


Figure 5.20: Electric field distribution inside the sapphire plates [119].

The results are compatible with the following assumptions: the electric field in the operating sapphire detector is not uniform, it is distorted by a polarization field. The shape of the polarization field is parabolic as shown in Figure 5.20. The resulting field has a minimum in the central part of the sensor and reaches maximum values near detector edges. A similar effect was observed in the irradiated scCVD diamond detectors, where the effect is even more pronounced and the electric field reaches zero values in the sensor bulk [76, 77]. About 30-40% of charge carriers, produced by ionizing particles, recombine at the very first moment. The rest of them drift in the electric field. This result is consistent with low hole mobility predicted in Ref. [120] and confirms the dominant contribution of electrons for the charge transport in sapphire [121, 122].

Summary and Conclusions

The LHC Run II started successfully in the beginning of 2015. The CMS experiment came back to operation with three online luminometers: the Fast Beam Conditions Monitor and the Hadron Forward calorimeter, upgraded during the LHC long technical stop, and the newly installed Pixel Luminosity Telescope. From the beginning of operation all the luminometers provided reliable feedback to the LHC.

The BCM1F detector performance monitoring

The diamond-based upgraded BCM1F detector was successfully installed and commissioned at the LHC in the beginning of 2015. The characteristics of the ASIC were confirmed to fulfill 25 ns operation requirements. Using the VME-based front-end modules, online luminosity measurements and detector conditions monitoring were performed.

The deadtime-free Real-time Histogramming Units with 6.25 ns bin width were employed for online monitoring of the detector rates and online luminosity and machine induced background measurements.

For the individual signal analysis 8 bit analog-to-digital converters with 2 ns sampling time were used. From baseline position monitoring, time over threshold histograms and amplitude spectra, a full characterization of the BCM1F system was done at the beginning of operation. Test pulse analysis was used for characterization of the electronics chain separately.

The so-called MIP peak position was used to monitor the stability of the ADC spectra. Using ROOT-based analysis programs and different BCM1F data samples, the stability of the BCM1F response within one data-taking period was confirmed. The MIP peak position was stable within ± 1 mV range. Already in 50 ns operation, up to a 6% decrease of the MIP peak position was observed, 4% of this decrease were associated with the radiation damage of the electronics. But the decrease of MIP position was concluded not to affect the rate measurement, as the separation between the MIP peak and analysis threshold was kept. Concerning further operation, radiation damage became more pronounced. In April 2016 for some of the channels it reached 20%, and later the bias voltage had to be lowered because of instabilities.

The number of smaller amplitude signals increased in the amplitude spectra of the irradiated sensors, forming a shoulder on the left side of the MIP peak. Combining this observation with the beam-test results we associated this effect with decreased field at the edges of the metallization and in the metallization gap.

In some of the BCM1F channels erratic currents and anomalous spikes in the rates were observed. These channels were excluded from the luminosity measurements.

A monitoring tool was developed for baseline position, amplitude spectra, signal length and test pulse spectra fast checks online. The automated data acquisition is followed directly by data processing and production of control plots.

The calibration of BCM1F as a luminometer

The van der Meer scans in 2015 and 2016 were used to calibrate the BCM1F detector as a luminometer. The calibration constant – the visible cross section – is needed to translate the measured rates into the luminosity. The RHU data was used for the measurement of the rates. The fits of the beam overlap regions in the x and y planes were made to two Gaussian distributions plus a constant background. The visible cross section for the BCM1F detector was determined.

Effects such as MIB and albedo contributions were estimated to be small and taken into account by the constant term of the fit. The impact of beam-beam effects, length scale calibration, $x - y$ correlations in the transverse particle densities in a bunch, the influence of different beam current measurements and contributions of ghost and satellite bunches on the visible cross section measurement were studied. The total systematic uncertainty of the visible cross section, taking into account detector stability, was estimated to be 3.1% for 50 ns operation period.

The visible cross sections obtained for the individual BCM1F channels reflected differences in the measured rates which for a couple of the selected channels reached about 10%. Due to radiation damage of the diamond sensors and the resulting decrease in the measured rates, the visible cross section measured in 2016 is lower than in 2015 by about 11% on average.

Beam test with sapphire detector

For future upgrades of near-beam detectors an alternative to the currently-used diamond and silicon sensors is needed, as diamond is expensive and silicon requires cooling. Artificially grown sapphire, widely used in industry, is a promising sensor material. It has already found its application as a solid state detector for beam current monitors, but we showed that it has high enough CCE even for the detection

of individual particles. It also has extremely low leakage current, it is radiation hard, and it does not require cooling.

A conceptually new sapphire detector design was proposed and tested in a 5 GeV electron beam. The CCE shows a linear dependence on the bias voltage, reaching up to 10% at 950 V. A measurement of the CCE as a function of the local coordinate through the thickness of the plates shows a pronounced dependence on track position with respect to the electrode. The measurement can be explained by a linear model pointing to a dominant contribution of electron drift to the signal charge and to the presence of a polarization field inside the bulk of the sensor. We conclude that the results are promising and sapphire should find many applications in particle physics not only as a beam monitor, but also as tracker or calorimeter detector material.

Appendix A

Adjustment of the BCM1F signal delay with respect to BPTX

A.1 BPTX signal delay

The BPTX system and signal processing are described in section 2.4. BPTX detectors are positioned symmetrically at $+Z$ and $-Z$ with respect to the IP at a distance of 175 m . Assuming that particles are traveling at the speed of light, it takes $t_{BPTX+ZIP} = t_{BPTX-ZIP} = 583\text{ ns}$ between BPTX and IP.

The cable lengths from BPTX to the counting room (S1) are different at the $+Z$ and $-Z$ side. Taking into account also the delay in the NIM logical modules, the measured BPTX signal travel time is $t_{BPTX+Ztravel} = 1087\text{ ns}$ and $t_{BPTX-Ztravel} = 1007\text{ ns}$. Using $t_{BPTXtravel}$ and t_{BPTXIP} we can calculate with which delay the BPTX signal arrives in S1 with respect to the time of the bunch crossing: $t_{BPTX+ZS1delay} = 504\text{ ns}$ and $t_{BPTX-ZS1delay} = 424\text{ ns}$.

A.2 BCM1F signal delay and coincidence with BPTX

The signals from diamond sensors on both ends of the CMS experiment have to pass the same electronics and cables chain, except for the fibre length from the experimental hall (PPO) to S1, which is 61.5 m from $+Z$ side and 55.5 m from $-Z$ side. This results into the following total delay of the BCM1F signal with respect to bunch crossing: $t_{BCM1F+ZS1delay} = 361\text{ ns}$ and $t_{BCM1F-ZS1delay} = 336\text{ ns}$. All delays are summarized in Table A.1.

For the $+Z$ end, the BPTX signal is delayed in S1 with respect to the bunch crossing by 504 ns . The BCM1F signal needs 361 ns to enter S1, hence an additional

Appendix A. Adjustment of the BCM1F signal delay with respect to BPTX

Table A.1: Delay of the BCM1F signals from +Z and -Z ends with respect to bunch crossing.

Delaying component	Travel time +Z (ns)	Travel time Z (ns)
FE ASIC	5	5
0.5 m flex	2.5	2.5
0.56 m fibre	2.5	2.5
AOH	10	10
2.2 m fibre	11	11
PP0 - PPS1	296	271
Optical receiver	20	20
Lemo cable	4	4
NIM FI/FO	10	10
Total	361	336

delay of 143 ns is needed, corresponding to a fibre of length 29 m. Using the same logic for the -Z end delay of $t_{BPTX+ZS1delay} - t_{BCM1F-ZS1delay} = 88ns$ is needed, corresponding to a fibre of 18m.

A.3 Coincidence of BPTX and BCM1F signals from both ends

Using delays calculated in sections A.1 and A.2 it is possible to calculate relative delays of the signals in coincidence of BPTX and BCM1F. As reference the BPTX signal arrival to S1 with the largest delay ($t_{BPTX+ZS1delay} = 504 ns$) after the bunch crossing is taken. Then the signal from BCM1F +Z end has to be delayed by $t_{BPTX+ZS1delay} - t_{BCM1F+ZS1delay} = 143 ns$ and the signal from BCM1F -Z end by $t_{BPTX-ZS1delay} - t_{BCM1F-ZS1delay} = 168 ns$. Taking the light propagation speed $v_p = 0.68$, these numbers correspond to fibre cable lengths of 29 m and 34 m, respectively.

The BCM1F signals from +Z and -Z are connected from the S1 to the optical receiver board by a cable of 41 m, corresponding to an additional delay of 200 ns. Hence, the signals from BCM1F are expected to be delayed with respect to the later BPTX signal by 57 ns for the +Z side and 32 ns for the -Z side. Also it has to be taken into account that the signals at the BCM1F sensors arrive 6.5 ns before the bunch crossing. The above numbers change then to $t_{BCM1F+Zfinaldelay} = 50.5 ns$ and $t_{BCM1F-Zfinaldelay} = 25.5 ns$.

A.4 Relative delay measurements using beam splash events

Using the splash events the arrival time of the BPTX and BCM1F signals was measured with an oscilloscope. Four output channels of BCM1F from each end were combined by a logical OR and provided to channel 1 and 2 of the oscilloscope. In channel 3, the OR of the BPTX beam 1 and beam 2 signal was computed. An example of a screenshot of a beam splash event from beam 1 and beam 2 is shown in Figure A.1. The relative time difference between BPTX signals and signals from +Z and -Z ends of the BCM1F was measured.

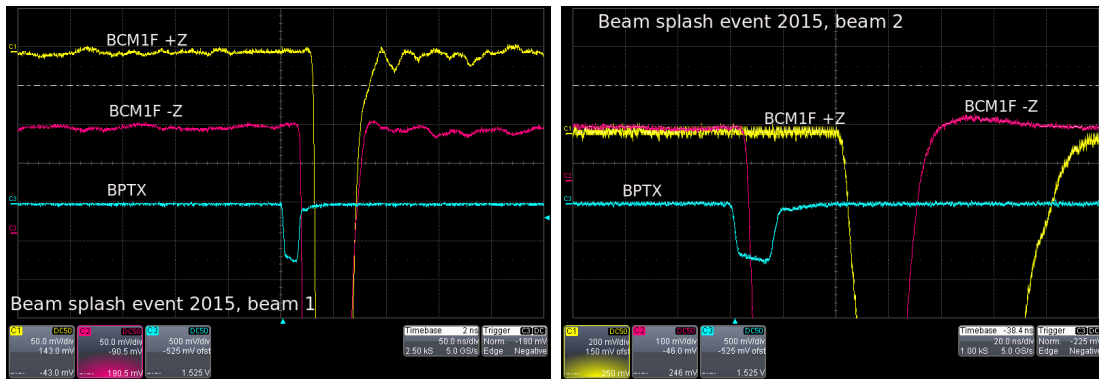


Figure A.1: The oscilloscope measurement of the beam 1 (left, x -axis scale 50 ns/div) and beam 2 splash event in April 2015 (right, x -axis scale 20 ns/div). In yellow the signal from BCM1F +Z end, in pink the signal from BCM1F -Z end and in light blue the BPTX signal.

Beam 1 enters the +Z end first and the signal from the sensors at the -Z end are delayed by 13 ns . The measured difference between the BPTX signal and the BCM1F +Z end is delayed 30 ns and between the BPTX signal and the BCM1F -Z end is 18 ns . Taking into account the 13 ns delay due to time of flight from the +Z to the -Z end, the delay of the signal from the -Z end is 5 ns .

For beam 2 splash events the beam enters BCM1F at the -Z end first and signal from BCM1F +Z is delayed by 13 ns . The measured difference between the BPTX signal and BCM1F +Z end is 42 ns and between the BPTX signal and the BCM1F -Z end is 5 ns . Taking into account the 13 ns time of flight between -Z and +Z, the delay of the BCM1F signals from the +Z end with respect to BPTX is 29 ns .

These numbers are in good agreement with the numbers obtained for beam 1. However, there is a difference of 20 ns , as a shift, to the numbers estimated from the cables and fibre lengths.

Appendix A. Adjustment of the BCM1F signal delay with respect to BPTX

Using the beam splash events in April 2015 the arrival time of the BCM1F signals with respect to the BPTX signals was measured. To obtain equal arrival time of BPTX and BCM1F signals in the counting room the fiber cable length for signals from the +Z end was reduced from 41 m to 36 m, reducing the BCM1F signal delay by 29 ns. The remaining 5 ns difference for signals from the -Z end was compensated using a different cable length.

Appendix B

Linear coordinate transformation for the sapphire stack

B.1 Detector alignment

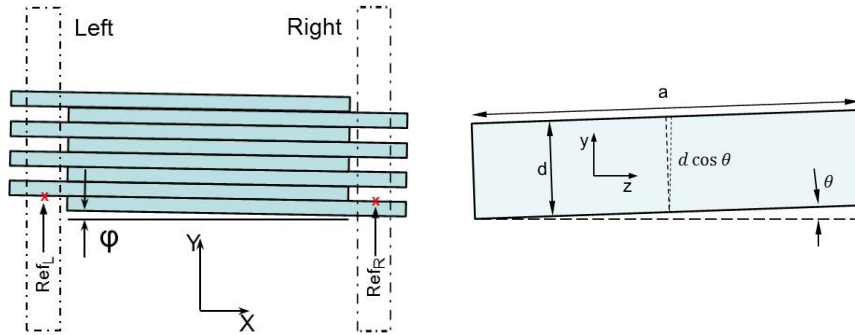


Figure B.1: Left: Detector stack as it is seen from the telescope. The alignment regions of interest are marked with dash-dotted line: Ref_L on the left, Ref_R on the right. Right: Longitudinal cut of the detector plate in the yz plane.

The narrow regions at the stack edges at $4.7 \text{ mm} < |x| < 5.2 \text{ mm}$ of Figure 5.10, were used for the alignment. The left part of Figure B.1 shows a schematic view of the stack. Regions of interest are indicated by dash-dotted lines and marked for Ref_L the reference on the left hand side edge and Ref_R for the reference on the right hand side edge. It is expected that the distribution of impact points at $z=0$ of scattered tracks will have a periodic structure, if plotted as a function of y . Half of the period of the distribution will be $d^* = d / \cos(\varphi)$, where d is the plate thickness and φ is the angle of the rotation of the stack. The reference plate positions are used for stack positioning and rotation angle determination.

Appendix B. Linear coordinate transformation for the sapphire stack

In the case when the detector stack is tilted with respect to the beam direction, the visible thickness of the plates will be changed as shown in Figure B.1 on the right. The effective thickness seen by the telescope becomes $d \cdot \cos(\theta)$ and the edge image is smeared with a full width of $a \cdot \sin(\theta)$. θ is the tilt angle with respect to the horizontal telescope plane, a is the length of the plate. Both the rotations in xy and yz planes give $d^* = d \cdot \cos(\theta) / \cos(\varphi)$ for the visible plate thickness projections and contribute to the smearing of the image edges. In addition, finite telescope spatial resolution will also lead to smearing of the edges.

Figure B.2 (left) shows the number of impact points of scattered tracks as a function of y in red color for the left and in black color for the right alignment regions. The expected periodic structure is clearly seen. The beam intensity correction was applied to the alignment distributions to take into account nonuniform beam intensity.

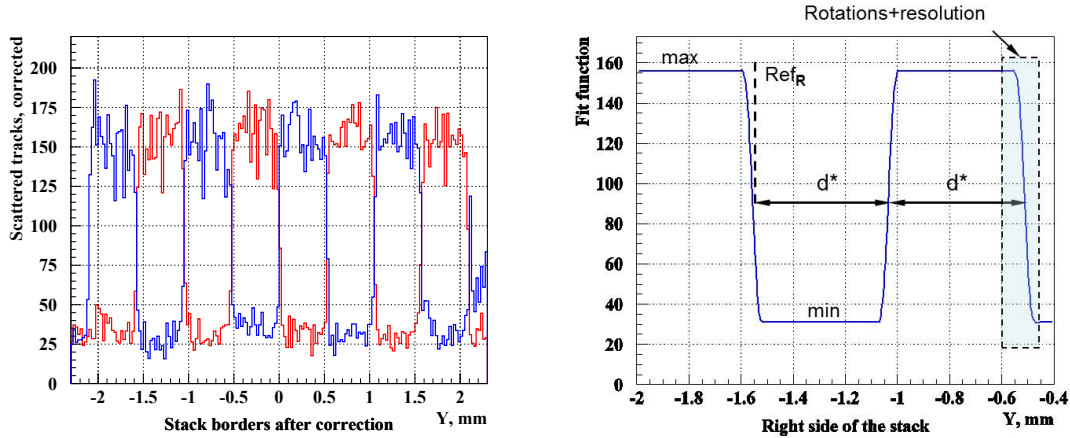


Figure B.2: Left: The number of scattered tracks as a function of y for the left (red) and right (blue) regions after beam intensity correction. Right: Example of the fit function used to define the geometrical parameters of the stack.

The alignment distributions for the left and right regions were used for the simultaneous alignment fit. The function used for this purpose is illustrated in Figure B.2 on the right. Edges of the fit function are assumed to be linear, being correct for the xy plane rotation and approximately correct for the stack inclination, since the multiple scattering angle cut introduces some nonlinearity. As a final fit a linear function convoluted with a Gaussian distribution was used.

The fit function contains 7 parameters: Ref_L and Ref_R are the shifts of the first trailing/leading edge position on the left and on the right side, as is shown in Fig. B.1; σ_{tel} is the telescope resolution, a Gaussian function is assumed; d^* is the

Appendix B. Linear coordinate transformation for the sapphire stack

visible plate thickness, a half-period of the fit function; f is the rotation and tilt parameter, without rotation $f = \sin(\theta)$; max is the normalization for the upper level; min is the normalization for the lower level.

It is worth mentioning that the parameters σ_{tel} and f both describe the edge shape and therefore are strongly correlated. So the fit was done for several scenarios: with the inclination parameter f set to a very small value and fixed; with the telescope impact point resolution fixed to $5 \mu\text{m}$ - close to real telescope resolution and with telescope impact point resolution fixed to $1 \mu\text{m}$ for the ideal resolution case. In the first scenario the fit program tends to describe the edges completely by the telescope resolution. Edges are described by Gaussian smearing. The resulting σ_{tel} value of $14.9 \mu\text{m}$ could be considered as an upper limit of the telescope resolution obtained from this analysis. In the second and third scenarios, the obtained f values are compatible. At the same time the f value obtained with fixed telescope resolution of $1 \mu\text{m}$ could be considered as an upper limit for the stack tilt.

Fit results for all mentioned scenarios are listed in Table B.1 and alignment regions of interest for both sides together with the fit are shown in Figure B.3 [119].

Table B.1: Parameters of the fit function for described scenarios.

Parameter	No stack inclination	$5 \mu\text{m}$ resolution	$1 \mu\text{m}$ resolution
Ref_L , mm	0.4778 ± 0.0010	0.4782 ± 0.0017	0.4784 ± 0.0017
Ref_R , mm	0.4427 ± 0.0013	0.4430 ± 0.0017	0.4434 ± 0.0018
σ_{tel} , mm	0.0149 ± 0.0012	0.005 (fixed)	0.001 (fixed)
d^* , mm	0.52236 ± 0.00028	0.52225 ± 0.00040	0.52218 ± 0.00045
f	0.000001 (fixed)	0.00431 ± 0.00039	0.00455 ± 0.00034
max	155.20 ± 1.06	155.78 ± 1.08	155.71 ± 1.07
min	31.10 ± 0.49	31.24 ± 0.48	31.26 ± 0.49

B.2 Linear coordinate transformation

Using parameter values, obtained for the fixed $5 \mu\text{m}$ telescope resolution, coefficients of a linear coordinate transformation were calculated. These coefficients include rotation in the counterclockwise direction, scaling and shift of the detector image. The new detector related coordinates are calculated from the relation:

$$\begin{bmatrix} x_1 \\ y_1 \end{bmatrix} = S \cdot \begin{bmatrix} \cos \varphi & -\sin \varphi \\ \sin \varphi & \cos \varphi \end{bmatrix} \cdot \begin{bmatrix} x_{tel} \\ y_{tel} \end{bmatrix} + \begin{bmatrix} x_0 \\ y_0 \end{bmatrix}, \quad (\text{B.1})$$

where S is a scaling factor, φ the rotation angle and x_0 , y_0 the shift of origin.

Appendix B. Linear coordinate transformation for the sapphire stack

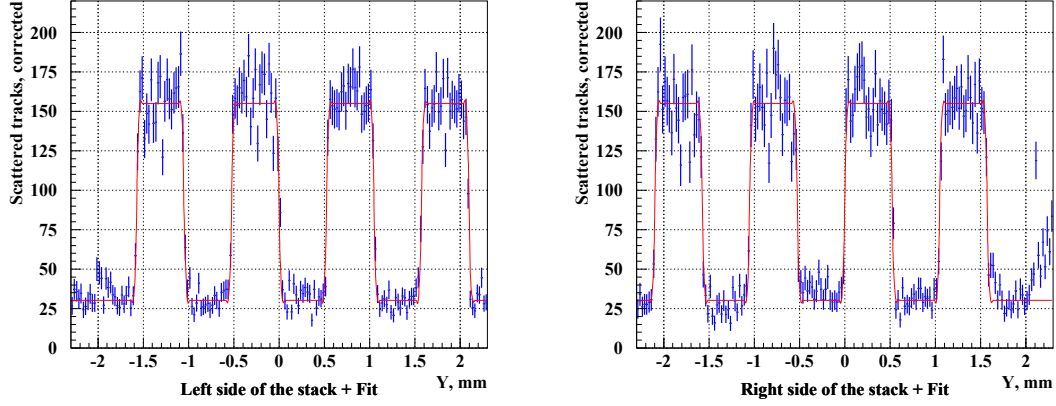


Figure B.3: Description of the experimental data by fit function for $5 \mu\text{m}$ telescope resolution [119].

Here x_{tel} , y_{tel} are coordinates, given by the telescope tracking and x_1 and y_1 the new coordinates in the detector coordinate system.

The rotation angle is calculated from the values of reference positions and the distance between alignment regions ΔX_{LR} :

$$\tan \varphi = (Ref_L - Ref_R) / \Delta X_{LR}. \quad (\text{B.2})$$

Substituting numbers, obtained from the fit from Table B.1, we get $0.0352/9.9 = 0.00356 \pm 0.00024$. This points to a rotation of the stack of only about 0.2° . The coefficients in the rotation matrix are: $\cos \varphi = 0.99999$, $\sin \varphi = 0.00356$.

The rotation and the tilt parameter f reflect the width of fit function edges. In the case of the stack inclination contribution only, the effective width of the edge could be expressed as $a \cdot \sin \theta = a \cdot f$, where $a = 10 \text{ mm}$ is a plate length along the beam direction. If the rotation of the stack also contributes to the edge width, this contribution can be estimated as $\omega \cdot \tan \varphi$, where ω is the width of alignment band of about 0.5 mm . The contribution of the rotation to f is given by $f^* = \omega \cdot \tan \varphi / a = 0.00018$, which is negligible compared to the value $f = 0.00431 \pm 0.00039$, obtained from the fit. We conclude that the dominant contribution to f originates from a tilt angle of 0.25° .

The scaling factor $S = 1.00527$ was applied to correct the visible thickness of sapphire plate to 0.525 mm .

Finally, the shift is calculated from the condition that the detector center has to be positioned at the origin of the coordinate system. Including the scaling factor

Appendix B. Linear coordinate transformation for the sapphire stack

into the rotation matrix and substituting into Eq. B.1, one gets:

$$\begin{bmatrix} x_1 \\ y_1 \end{bmatrix} = \begin{bmatrix} 1.00527 & -0.00358 \\ 0.00358 & 1.00527 \end{bmatrix} \cdot \begin{bmatrix} x_{tel} \\ y_{tel} \end{bmatrix} + \begin{bmatrix} 0.0 \\ -0.0275 \end{bmatrix}. \quad (\text{B.3})$$

Using the new coordinate system, the second iteration of data selection has been performed.

Bibliography

- [1] L. Evans and P. Bryant (editors), *LHC Machine*, 2008 JINST 3S08001.
- [2] J. Bennett, et al., *Design concept for a 100 GeV $e^+ e^-$ storage ring (LEP)*, CERN 77-14 (1977).
- [3] The European Organization for Nuclear Research, <https://home.cern/>
- [4] *LHC Magnets* web-page <http://lhc-machine-outreach.web.cern.ch/lhc-machine-outreach/components/magnets.htm>
- [5] *LHC magnet types* web-page https://lhc-machine-outreach.web.cern.ch/lhc-machine-outreach/components/magnets/types_of_magnets.htm
- [6] E. Kugler et al., *The New CERN ISOLDE online mass separator facility at the PS Booster*, CERN-PPE-91-170, C91-09-02.2 and home-page <http://isolde.web.cern.ch/>
- [7] The neutron time-of-flight facility at CERN, home-page <https://ntof-exp.web.cern.ch/ntof-exp/>
- [8] E. Gschwendtner, *AWAKE, The Advanced Proton Driven Plasma Wakefield Acceleration Experiment at CERN*, arXiv:1512.05498 (2015).
- [9] W. Oelert for ELENA Collaboration, *The ELENA project at CERN*, arXiv:1501.05728 (2015).
- [10] ATLAS Collaboration, *Atlas detector and physics performance: Technical Design Report, Volume 1*, CERN-LHCC-99-14, ATLAS-TDR-14.
- [11] ATLAS Collaboration, *Atlas detector and physics performance: Technical Design Report, Volume 2*, CERN-LHCC-99-15, ATLAS-TDR-15.
- [12] CMS Collaboration, *CMS physics TDR (PTDR1), Detector Performance and Software*, CERN-LHCC-2006-001.

Bibliography

- [13] CMS Collaboration, *The CMS experiment at LHC*, JINST 3 (2008), doi:10.1088/1748-0221/3/08/S08004
- [14] ALICE Collaboration, *Technical Proposal for A Large Ion Collider Experiment at the CERN LHC*, CERN/LHCC/95-71, (1995).
- [15] LHCb Collaboration, *LHCb: Technical Proposal*, CERN-LHCC-98-004 (1998).
- [16] LHCf Collaboration, *LHCf experiment: Technical Design Report*, CERN-LHCC-2006-004.
- [17] G. Ruggiero et al., *The TOTEM Detector at LHC*, CERN-LHCC-2005-002, (2005).
- [18] The ATLAS Collaboration, *Observation of a new particle in the search for the Standard Model Higgs boson with the ATLAS detector at the LHC*, Phys. Lett. B 716 (2012) 1, doi:10.1016/j.physletb.2012.08.020, arXiv:1207.7214.
- [19] The CMS Collaboration, *Observation of a new boson at a mass of 125 GeV with the CMS experiment at the LHC*, Phys. Lett. B 716 (2012) 30, doi:10.1016/j.physletb.2012.08.021, arXiv:1207.7235.
- [20] The CMS Collaboration, *CMS Tracking Performance Results from early LHC Operation*, Eur. Phys. Journal C, 70:1165-1192, (2010).
- [21] The CMS Collaboration, *Electromagnetic calorimeter commissioning and first results with 7 TeV data*, CMS NOTE-2010/012 (2010).
- [22] F. Nessi-Tedaldi on behalf of the CMS Collaboration, *Response evolution of the CMS ECAL and R&D studies for electromagnetic calorimetry at the High-Luminosity LHC*, ETHZ-IPP-2012-03; CMS CR-2012/296, arXiv:1211.3885 (2012).
- [23] J. Mans (editor), *CMS Technical Design Report for the Phase 1 Upgrade of the Hadron Calorimeter*, CERN-LHCC-2012-015, CMS-TDR-010 (2012).
- [24] M. Garcia, *CMS muon system status*, The 2007 Europhysics Conference on High Energy Physics (2008).
- [25] The ATLAS Collaboration, *Measurements of Higgs boson production and couplings in diboson final states with the ATLAS detector at the LHC*, Phys. Lett. B 726 (2013) 88, doi:10.1016/j.physletb.2013.08.010, arXiv:1307.1427.
- [26] The ATLAS Collaboration, *Evidence for the spin-0 nature of the Higgs boson using ATLAS data*, Phys. Lett. B 726 (2013) 120, doi:10.1016/j.physletb.2013.08.026, arXiv:1307.1432.

Bibliography

- [27] The CMS Collaboration, *Evidence for the 125 GeV Higgs boson decaying to a pair of τ leptons* , JHEP 05 (2014) 104, doi:10.1007/JHEP05(2014)104, arXiv:1401.5041.
- [28] The ATLAS Collaboration, *Measurement of Higgs boson production in the diphoton decay channel in pp collisions at center-of-mass energies of 7 and 8 TeV with the ATLAS detector* , Phys. Rev. D 90 (2014) 112015, doi:10.1103/PhysRevD.90.112015, arXiv:1408.7084.
- [29] The CMS Collaboration, *Precise determination of the mass of the Higgs boson and tests of compatibility of its couplings with the standard model predictions using proton collisions at 7 and 8 TeV* , Eur. Phys. J. C 75 (2015) 212, doi:10.1140/epjc/s10052-015-3351-7, arXiv:1412.8662.
- [30] ATLAS and CMS Collaboration, *Combined measurement of the Higgs boson mass in pp collisions at $\sqrt{s} = 7$ and 8 TeV with the ATLAS and CMS experiments*, Phys. Rev. Lett.114 (2015) 191803, doi:10.1103/PhysRevLett.114.191803, arXiv:1503.07589.
- [31] The CMS Collaboration, *Evidence for the direct decay of the 125 GeV Higgs boson to fermions* , Nature Phys. 10 (2014) 557, doi:10.1038/nphys3005, arXiv:1401.6527.
- [32] The CMS Collaboration, *Measurement of the transverse momentum spectrum of the Higgs boson produced in pp collisions at $\sqrt{s} = 8$ TeV using $H \rightarrow WW$ decays*, CMS-HIG-15-010; CERN-EP-2016-125 (2016).
- [33] The CMS Collaboration, *Search for two Higgs bosons in final states containing two photons and two bottom quarks*, CMS-HIG-13-032; CERN-EP-2016-050 (2016).
- [34] C. Autermann, *Experimental Status of Supersymmetry after the LHC Run-I*, Progress in Particle and Nuclear Physics 90 (2016) 125-155, arXiv:1609.01686.
- [35] The CMS Collaboration, *Measurement of inclusive W and Z boson production cross sections in pp collisions at $\sqrt{s} = 13$ TeV*, CMS PAS SMP-15-004, (2015).
- [36] G. Arduini, *Post LS1 Operation*, in proceedings of the MPP Workshop on LHC Machine Protection, 11–13 March 2013, Annecy, France, CERN-ACC-2014-0041 (2014).
- [37] R. Bruce et al., *Sources of machine-induced background in the ATLAS and CMS detectors at the CERN Large Hadron Collider*, Nucl. Instrum. Meth. A 729 (2013) 825.

Bibliography

- [38] H. Burkhardt and P. Grafstrom, *Absolute Luminosity from Machine Parameters*, LHC Project Report 1019 (2007).
- [39] S. van der Meer, *Calibration of the Effective Beam Height in the ISR*, CERN-ISR-PO-68-31, (1968).
- [40] CMS Collaboration, *Luminosity Calibration for the 2013 Proton-Lead and Proton-Proton Data Taking*, CMS-PAS-LUM-13-002 (2013). URL <https://cds.cern.ch/record/1643269>.
- [41] H. Abramowicz et al., *Forward instrumentation for ILC detectors*, JINST 5:P12002 (2010).
- [42] A. Dabrowski for the CMS collaboration, *Upgrade of the CMS instrumentation for luminosity and machine induced background measurements*, proceedings of 37th International Conference on High Energy Physics, July 2014, Valencia, Spain, CMS-CR-2014-362 (2014).
- [43] M. Guthoff, et al., *Radiation damage in the diamond based beam condition monitors of the CMS experiment at the Large Hadron Collider (LHC) at CERN*, Nucl.Instrum.Meth. A730 (2013) 168-173.
- [44] A. Pozdnyakov, et al., *BPTX electronics and software at CMS*, CMS information server CMS IN-2013/010.
- [45] A. Gabriel, *Using the BPTX for relative bunch population measurements*, LPCC Workshops, LHC Lumi Days 2012, CERN, Geneva, (2012).
- [46] Y. Allkofer, et al., *Design and performance of the silicon sensors for the CMS barrel pixel detector*, Nucl. Instrum. Methods Phys. Res., A 584 (2008) 25-41.
- [47] M. Barbero et al., *Design and test of the CMS pixel readout chip*, Nucl. Instrum. Methods Phys. Res., A 517 (2004) 349.
- [48] O. Novgorodova, *Characterisation and Application of Radiation Hard Sensors for LHC and ILC*, PhD Thesis DESY-THESIS-2013-052, November 2013 (CMS).
- [49] A. Bell et al., *Fast Beam Conditions Monitor BCM1F for the CMS Experiment*, Nucl.Instrum.Meth. A614 (2010) 433-438, DOI: 10.1016/j.nima.2009.12.056
- [50] N. Odell on behalf of the CMS Collaboration, *Measurements of luminosity and normalised beam-induced background using the CMS Fast Beam Condition Monitor*, 36th International Conference on High Energy Physics, Melbourne, Australia (2012), PoS(ICHEP2012)526.

Bibliography

- [51] M. Mikuz et al., *Diamond pad detector telescope for beam conditions and luminosity monitoring in ATLAS*, Nucl.Instrum.Meth. A579 (2007) 788-794, DOI:10.1016/j.nima.2007.05.297
- [52] V. Cindro et al., *The ATLAS beam conditions monitor*, JINST 3 (2008) P02004, DOI: 10.1088/1748-0221/3/02/P02004
- [53] Ch. Ilgner et al., *The Beam Conditions Monitor of the LHCb Experiment*, arXiv:1001.2487
- [54] S. Sfyrla et al., *Beam Condition Monitoring with Diamonds at CDF*, IEEE Trans.Nucl.Sci. 55 (2008) 328-332, DOI: 10.1109/TNS.2007.913492
- [55] S. Orfanelli et al., *A novel Beam Halo Monitor for the CMS experiment at the LHC*, 2015 JINST 10 P11011.
- [56] M. Guthoff for the CMS collaboration, *Instrumentation for beam radiation and luminosity measurement in the CMS experiment using novel detector technologies*, 14th Vienna Conference on Instrumentation, VCI (2016).
- [57] CMS Collaboration, *CMS Luminosity Based on Pixel Cluster Counting - Summer 2013 Update*, CMS Physics Analysis Summary LUM-13-001, (2013).
- [58] G. Battistoni, et al., *The FLUKA code: Description and benchmarking*, in: M. Albrow, R. Raja (Eds.), Proceedings of the Hadronic Shower Simulation Workshop 2006, Vol. AIP Conference Proceeding 896, Fermilab 6–8 September 2006, 2007, pp. 31–49.
- [59] I. Azhgirey, et al., *Proceedings of XVIII Workshop of the Charged Particles Accelerators*, Protvino, (2000).
- [60] M. Huthoff on behalf of the BRIL, *Upgrades to the Beam Condition Monitors at CMS*, 4th ADAMAS workshop, GSI, Darmstadt, Germany (2015).
- [61] S. Mallows, et al., *Monte Carlo simulations of the radiation environment for the CMS experiment*, Nucl.Instrum.Meth. A824 (2016) 30-32, doi: 10.1016/j.nima.2015.11.044
- [62] Particle Data Group booklet, extracted from the Review of Particle Physics, J. Beringer, et al. (PDG), Phys.Rev.D86, 010001 (2012).
- [63] L. Landau, *On the energy loss of fast particles by ionization*, J.Phys.(USSR). 8: 201. (1944)
- [64] Wolfram, *Convolution*, <http://mathworld.wolfram.com/Convolution.html>

Bibliography

- [65] M. Ohlerich, *Investigations of the Physics Potential and Detector Development for the ILC*, PhD Thesis DESY-THESIS-2010-008, February 2010 (ZEU).
- [66] M. Hempel, *Development of a new diamond based detector for machine induced background and luminosity monitoring*, PhD Thesis DESY-Zeuthen (2017).
- [67] D. Przyborowski, et al., *Design and Performance of the BCM1F Front End ASIC for the Beam Condition Monitoring System at the CMS Experiment*, IEEE TRANSACTIONS ON NUCLEAR SCIENCE, VOL. 63, NO. 4, (2016).
- [68] M. Hempel, et al., *Measurements of the performance of a beam condition monitor prototype in a 5GeV electron beam*, doi:10.1016/j.nima.2016.04.038 (2016).
- [69] O. Karacheban, et al., *A new on-line luminometer and beam conditions monitor using single crystal diamond sensors*, 13th Pisa Meeting on Advanced Detectors, Elba2015, Biodola, Italy, May 2015.
- [70] Optical Links for CMS webpage, <http://cms-tk-opto.web.cern.ch/cms-tk-opto>.
- [71] A. Zagodzinska, et al., *New Fast Beam Conditions Monitoring (BCM1F) system for CMS*, Presentation TWEPP (2015).
- [72] CAEN, *8 Channel 8 bit 500 MS/s Digitizer V1721*. URL <http://www.caen.it/csite/CaenProd.jsp?parent=11&idmod=532>.
- [73] H. Henschel, Developer of the V1495 Testpulse Generator for the BCM1F front-end.
- [74] M. Penno, et al., *A Real-time Histogramming Unit for Luminosity and Beam Background Measurements for each Bunch Crossing at the CMS*, Presentation TWEPP 2013 - Topical Workshop on Electronics for Particle Physics, Perugia, Italy (2013).
- [75] Private communication with Jessica Leonard.
- [76] S. Schuwalow, *Polarization effects in radiation damaged scCVD Diamond detectors*, 4th NoRHDia Workshop at GSI, Darmstadt (2008).
- [77] F. Kassel, et al., *Severe signal loss in diamond beam loss monitors in high particle rate environments by charge trapping in radiation-induced defects*, Phys. Status Solidi A 213, No. 10, 2641–2649 (2016) / DOI 10.1002/pssa.201600185
- [78] M. Ferro-Luzzi and W. Herr, *LHC bunch filling schemes for commissioning and initial luminosity optimization*, LHC Project Note 415, (2008).

Bibliography

- [79] J. Behr, *Test Beam Measurements with the EUDET Pixel Telescope*, EUDET-Report-2010-01, Hamburg (2010).
- [80] Private communication with Jonas Daugalas, Zhen Xie and Arkady Likhovitskiy.
- [81] CMS Online Software project page, Internal CERN Documentation URL <https://svnweb.cern.ch/trac/cmsos> and <https://edms.cern.ch/ui/#!/master/navigator/document?D:1832636191:1832636191:subDocs>.
- [82] J. Leonard, et al., *Fast beam condition monitor for CMS: Performance and upgrade*, Proceedings from HSTD-9-13 conference - Hiroshima, Japan (2013).
- [83] VdM scan analysis framework designed by Monika Grothe for CMS. Internal CERN Documentation URL <https://twiki.cern.ch/twiki/bin/viewauth/CMS/VdMLumiFramework>.
- [84] Python, URL <https://docs.python.org/2/tutorial/index.html#tutorial-index>.
- [85] ROOT, URL <https://root.cern.ch/>.
- [86] G. Anders, et al., *LHC Bunch Current Normalisation for the April-May 2010 Luminosity Calibration Measurements*, CERN-ATS-Note-2011-004 PERF, (BC-NWG note1) (2011). URL <http://cdsweb.cern.ch/record/1325370>.
- [87] C. Barschel, et al., *Results of the LHC DCCT Calibration Studies*, CERN-ATS-Note-2012-026 PERF (2012). URL <http://cds.cern.ch/record/1425904>.
- [88] C. Barschel, *DCCT uncertainties for VDM fills in Aug 2015*, slides from LHC LCMWG meeting Sept. 28, 2015. URL <https://indico.cern.ch/event/447902/contribution/0>.
- [89] G. Papotti, et al., *Longitudinal Beam Measurements at the LHC: The LHC Beam Quality Monitor*, CERN-ATS-Note-2011-220 (2011). URL <http://cds.cern.ch/record/1399087>.
- [90] C. Barschel, *Ghost Charges for VDM fills Aug 2015*, slides from LHC LCMWG meeting Oct. 19, 2015. URL <https://indico.cern.ch/event/454827/contribution/0>.
- [91] M. Palm, *BSRL: VdM-scan August 2015*, slides from LHC LCMWG meeting Sept. 28, 2015. URL <https://indico.cern.ch/event/447902/contribution/2>.
- [92] J.L. Gonzalez, et al., *The Measurement of Bunch Intensity using the LHC BPM System*, CERN-BE-2009-017 (2009). URL <http://cds.cern.ch/record/1183398>.

Bibliography

- [93] CMS Collaboration, *CMS Luminosity Based on Pixel Cluster Counting - Summer 2012 Update*, CMS Physics Analysis Summary LUM-12-001, (2012).
- [94] M. Klute, C. Medlock and J. Salfeld-Nebgen, *Beam Imaging and Luminosity Calibration*, arXiv:1603.03566, (2016).
- [95] CMS Collaboration, *CMS luminosity measurement for the 2015 data taking period*, CMS Physics Analysis Summary LUM-15-001, (2015).
- [96] W. Kozanecki, T. Pieloni, and J. Wenninger, *Observation of Beam-beam Deflections with LHC Orbit Data*, CERN-ACC-NOTE-2013-0006 (2013). URL <http://cds.cern.ch/record/1581723>.
- [97] A. Ignatenko, *Beam Halo Monitor for FLASH and the European XFEL*, IPAC-2012 New Orleans, Conf.Proc. C1205201 (2012) 816-818.
- [98] J. Stone-Sundberg, *Sapphire Series Part 1: Introduction to Sapphire and Synthetic Sapphire*, <http://www.gia.edu/gia-news-research-Sapphire-Series-Introduction-to-Sapphire-and-Synthetic-Sapphire>, USA (2013).
- [99] D. Harris, *A Century of Sapphire Crystal Growth*, Proceedings of the 10th DoD Electromagnetic Windows Symposium Norfolk, Virginia (2004).
- [100] A. Verneuil, *Memoire sur la Reproduction du Rubis par Fusion*, Ann. Chim. Phys. Ser 8, 3: 20-48 (1904).
- [101] J. Stone-Sundberg, *Sapphire Series Part 2: The Next Generation of Sapphire Crystal Growth Techniques*, <http://www.gia.edu/gia-news-research-Sapphire-Series-Next-Generation-Growth-Techniques>, USA (2013).
- [102] ARC Energy, *New Technique Grows World's Largest Sapphire Crystal*, <http://www.engineering.com/AdvancedManufacturing/ArticleID/10587/New-Technique-Grows-Worlds-Largest-Sapphire-Crystal.aspx>, (2015).
- [103] C.A. Klein, *Bandgap Dependence and Related Features of Radiation Ionization Energies in Semiconductors*, J.Appl.Phys., 39, 2029 (1968), DOI:10.1063/1.1656484.
- [104] A.Owens, *Compound Semiconductor Radiation Detectors*, p.398, CRC Press 2012, ISBN: 9781439873137.
- [105] F. Wang, J. Shan, E. Knoesel, M. Bonn, and T.F. Heinz, *Electronic Charge Transport in Sapphire Studied by Optical Pump/THz-Probe Spectroscopy*, Proceedings of the SPIE, 5352 , 216 (2004).

Bibliography

- [106] F. Kassel et al., *Investigations of electric field effects caused by radiation induced defects. Irradiation campaign and TCT measurements*. Talk at 4th ADAMAS Workshop, GSI, Darmstadt (2015).
- [107] CRYSTAL GmbH, Ostendstrasse 25, D-12459 Berlin, Germany, <http://crystal-gmbh.com/en/contact/persons.php>.
- [108] GSI Detector Laboratory, Darmstadt, Germany, https://www.gsi.de/work/fairgsi/rare_isotope_beams/detector_laboratory.htm.
- [109] Molecular Technology GmbH, Rudower Chaussee 29-31 (OWZ), 12489 Berlin, Germany, http://www.mt-berlin.com/frames_cryst/descriptions/sapphire.htm.
- [110] E. Pearson, *Sapphire and Quartz as a Detector Material for the BeamCal of the ILC*, Summer student report, DESY-Zeuthen (2008).
- [111] S. Schuwalow, W. Lange, *Sapphire detectors for Beam Monitoring*, Talk at WS on CMS Beam Conditions, DESY-Zeuthen, (2013).
- [112] Ch. Grah et al., *Polycrystalline CVD diamonds for the beam calorimeter of the ILC*, IEEE Trans.Nucl.Sci. 56 (2009) 462-467, DOI: 10.1109/TNS.2009.2013853.
- [113] B. Barish et al., *The International Linear Collider Technical Design Report*, ILC-REPORT-2013-040, arXiv:1306.6327.
- [114] H. Abramowicz et al., *Forward Instrumentation for ILC Detectors*, JINST 5 (2010) P12002, DOI: 10.1088/1748-0221/5/12/P12002.
- [115] A. Ignatenko, *Development of Beam Halo Monitors for the European XFEL using Radiation Hard Sensors and Demonstration of the Technology at FLASH*, PhD Thesis, BTU, <https://opus4.kobv.de/opus4-btu/frontdoor/index/index/docId/3475>.
- [116] Amptek, Inc., Bedford, MA, USA, <http://www.amptek.com/products/a250-charge-sensitive-preamplifier>.
- [117] V. Blobel, *Millepede II Linear Least Squares Fit with a Large Number of Parameters*, <http://www.desy.de/~blobel/Mptwo.pdf>, Hamburg (2007).
- [118] R. Brun et al., GEANT3, Preprint CERN-DD/EE/84-1 (1984), revised 1985.
- [119] Collaborative work with Sergej Schuwalow.
- [120] Yong-Nian Xu and W.Y. Ching, *Self-consistent band structures, charge distributions, and optical-absorption spectra in MgO, α -Al₂O₃, and MgAl₂O₄*, Phys. Rev. B 43, 4461 (1991), DOI: 10.1103/PhysRevB.43.4461.

Bibliography

- [121] R.C. Hughes, *Generation, transport, and trapping of excess charge carriers in Czochralski-grown sapphire*, Phys. Rev. B 19, 5318 (1979); DOI: 10/PhysRevB.19.5318.
- [122] U.E. Hochuli, *Photoconductivity Measurements in Ruby and Sapphire*, Phys. Rev. 133. A 468 (1964); DOI: 10.1103/PhysRev.133.A468.